

ON THE DYNAMICS IN PLANETARY SYSTEMS,
GLOBULAR CLUSTERS AND GALACTIC NUCLEI

by

BENJAMIN THOMAS GEORGE BRADNICK



UNIVERSITY OF
BIRMINGHAM

A thesis submitted to the University of Birmingham for the degree of DOCTOR OF
PHILOSOPHY

School of Physics & Astronomy

College of Engineering and Physical Sciences

University of Birmingham

May 2017

UNIVERSITY OF
BIRMINGHAM

University of Birmingham Research Archive

e-theses repository

This unpublished thesis/dissertation is copyright of the author and/or third parties. The intellectual property rights of the author or third parties in respect of this work are as defined by The Copyright Designs and Patents Act 1988 or as modified by any successor legislation.

Any use made of information contained in this thesis/dissertation must be in accordance with that legislation and must be properly acknowledged. Further distribution or reproduction in any format is prohibited without the permission of the copyright holder.

Abstract

N-body simulations are used to investigate the dynamics of planetary systems based on the observed period-radius distribution by Kepler. The stability of the distribution is tested using integrations of 2,000 systems and with the addition of a Jupiter-like perturber in an aligned and inclined configuration sufficient for Lidov-Kozai (LK) oscillations. $\sim 67\%$ of planetary systems are found stable, falling to $\sim 62\%$ and $\sim 48\%$ with an aligned or inclined giant perturber. Planet ejections are rare. Instability timescales of systems are predicted by spacing and multiplicity of planets, but exceptions are common. Evolution of select individual systems are investigated and classified.

The dynamics of stellar binaries on eccentric orbits around a massive black hole (MBH) in the empty loss cone (LC) are also explored. The LK mechanism is suppressed by two-body relaxation from stars in galactic nuclei whilst tidal perturbations from the MBH excite the eccentricity of the binary to produce mergers in $\sim 75\%$ of simulations. Stellar tides circularise the binaries and produce low velocity mergers. Enhanced magnetic fields in merger products could explain relativistic jet formation in tidal disruption events (TDEs).

A method is presented for rapidly calculating the stellar evolution of stars with masses $m = 8.0 - 300.0 M_{\odot}$ and metallicities $-4.0 \leq [Z/H] \leq 0.5$ that can be incorporated into future n-body simulations.

Acknowledgements

First of all I would like to thank my supervisor Dr. Will Farr. You have been a great mentor and both your advice and encouragement have helped me immensely throughout my research. I am also very grateful to my co-supervisor Professor Ilya Mandel, who has provided huge amounts of support and guidance since the beginning of my fourth year of undergraduate study at the university and is also responsible for the publication of my first paper (for which I also thank Professor Yuri Levin, for his useful input on the project).

I thank the STFC for providing the funding to support my research.

Lastly, I'd like to thank Sarah, who has stood beside me for the last seven years, along with all of my family and friends.

Contents

1	Introduction	11
2	The stability of the observed period-radius distribution of planets	19
2.1	Introduction	20
2.2	Theory	22
2.2.1	The period-radius distribution of planets	23
2.2.2	Close encounters and stability	24
2.2.3	Resonances	28
2.3	Previous works	33
2.3.1	Stability of hypothetical systems	33
2.3.2	The stability of the Solar System	36
2.3.3	Stability of exoplanetary systems	37
2.3.4	Comparison to this work	38
2.4	Methodology	39
2.4.1	Generating planetary systems	39
2.4.2	Numerical integrations	40
2.4.3	Analysis of results	41
2.5	Results	50
2.5.1	Stability of the overall population	50
2.5.2	Comparisons between the final distributions	70
2.5.3	The instability of the planetary systems	71

2.6	Conclusion	82
2.7	Discussion	84
2.7.1	Limitations	88
3	Tidal disruptions of stellar binaries by a massive black hole	97
3.1	Preamble	98
3.2	Abstract	98
3.3	Introduction	99
3.4	Methods	102
3.4.1	Binary population	103
3.4.2	Outer orbit around the MBH	104
3.4.3	Stellar tides	105
3.5	Results of numerical integrations	107
3.6	Discussion	114
4	Stellar population synthesis and interpolating stellar tracks	128
4.1	Introduction	129
4.2	Methods	130
4.2.1	Storing EEP tracks	130
4.2.2	Interpolating between EEP tracks	131
4.2.3	Evolving a star	135
4.2.4	Obtaining the mass distribution of a cluster	137
4.3	Results	138
4.3.1	Stellar radius through each phase	139
4.3.2	Stellar evolution on the MIST grid	139
4.3.3	Mass distributions using MIST versus SSE	142
4.4	Discussion	145
A	Appendix	152
A.1	Converting between orbital elements and state vectors	153

A.1.1	State vectors to orbital elements	153
A.1.2	Orbital elements to state vectors	155
A.2	Inverse transform sampling	157
A.2.1	Mutual inclination of the MBH-binary	158
A.2.2	Power law	158
A.2.3	Gaussian	159
A.3	Parabolic orbits	160
A.4	Stellar tides using a Runge-Kutta Cash-Karp method	162
A.5	Tidal disruption of a star and binary by a MBH	164
A.6	Fluctuations of the binary orbital energy by a MBH	166
A.7	Long-term Kepler system integrations	167
A.8	Evolution of individual Kepler planetary systems	179

List of figures

2.1	Roche potential	27
2.2	Mutual inclination	30
2.3	Lidov-Kozai timescale	32
2.4	Stability of the Kepler planet systems integrated alone	51
2.5	Histogram of planet spacings for Kepler planet systems	52
2.6	Multiplicities in Kepler planet systems	53
2.7	Multiplicity of Kepler planet systems versus planet spacings	54
2.8	Period-radius distribution of Kepler planet systems	55
2.9	KDE of period-radius distribution of Kepler planet systems	55
2.10	Inclination distribution of Kepler planet systems	57
2.11	Inclination and eccentricities of Kepler planets	57
2.12	Stability of Kepler planet systems with aligned Jupiter-like perturber	59
2.13	Histogram of planet spacings for Kepler planet systems with aligned perturbers	59
2.14	Multiplicities in Kepler planet systems with aligned perturbers	60
2.15	Period-radius distribution of Kepler planet systems with aligned per- turbars	61
2.16	KDE of period-radius distribution of Kepler planets with aligned per- turbars	62
2.17	Inclination distribution for Kepler planet systems with aligned per- turbars	63

2.18	Inclination and eccentricities of Kepler planets with aligned perturbers	63
2.19	Stability of Kepler planet systems with inclined perturbers	64
2.20	Histograms of planet spacings for Kepler planet systems with inclined perturbers	65
2.21	Multiplicities of Kepler planet systems with inclined perturbers . . .	65
2.22	Period-radius distribution of Kepler planets with inclined perturbers .	66
2.23	KDE of the period-radius distribution of Kepler planets with inclined perturbers	66
2.24	Inclination distribution of Kepler planet systems with inclined per- turbers	68
2.25	Histogram of the standard deviation of inclination of Kepler planet systems with inclined perturbers	68
2.26	Histogram of Kepler planets with inclined perturbers	69
2.27	KDE comparisons of the final period-radius distributions of Kepler planets with and without perturbers	71
2.28	Stability timescale of Kepler planet systems	72
2.29	Reproduction of Chambers et al. (1996) fit	74
2.30	Stability timescale versus minimum planet spacing for systems of five Kepler planets and an aligned perturber	76
2.31	Stability timescale of Kepler planet systems with inclined perturbers .	76
2.32	Integration time of Kepler planet systems by multiplicity	78
2.33	Maximum eccentricity in high eccentricity Kepler planet systems with perturbing bodies	82
2.34	Planet spacings in observed Kepler systems	86
3.1	Eccentricity excitation of a stellar binary	108
3.2	Suppression of Lidov-Kozai evolution	109
3.3	Final eccentricity distribution of mergers	110
3.4	Initial inner semimajor axis distribution	111

3.5	Collisional velocity of mergers	112
3.6	Delay between merger and disruption	113
3.7	Distribution of hyperbolic excess velocities	114
4.1	Stellar radius at the start of each FSPS phase	139
4.2	Final stellar masses pre-SN for MIST and SSE (COMPAS)	141
4.3	Final CO core masses for MIST and SSE (COMPAS) stars	141
4.4	Remnant masses of MIST and SSE stars using the Fryer et al. (2012) delayed supernova mechanism	142
4.5	Mass distribution of MIST and SSE stars at $Z = 0.02$	143
4.6	Comparison of final and CO core masses between SSE and MIST at $Z = 0.02$	144
4.7	Comparison of remnant masses between MIST and SSE at $Z = 0.02$.	145
4.8	Mass distribution of MIST and SSE stars at $Z = 0.005$	146
4.9	Comparison of final and CO core masses between SSE and MIST at $Z = 0.005$	146
4.10	Comparison of remnant masses between MIST and SSE at $Z = 0.005$	147
A.1	Eccentricity evolution for system 4000	170
A.2	Semimajor axis evolution for system 4000	171
A.3	Inclination evolution for system 4000	171
A.4	Eccentricity evolution for system 4005	173
A.5	Semimajor axis evolution for system 4005	173
A.6	Eccentricity and inclination evolution of system 4005	174
A.7	Semimajor axis evolution for system 4011	176
A.8	Eccentricity and inclinaton evolution for system 4011	177
A.9	Eccentricity evolution of system 4006	178
A.10	Semimajor axis evolution for system 4009	178
A.11	Eccentricity evolution of system 4009	179

A.12 Evolution of a precessing disk system	181
A.13 Evolution of a precessing 2-disk system	181
A.14 Precession of periapses for two planets in single-disk system	182
A.15 Eccentricity evolution of the single-disk system	182

List of tables

2.1	Property constraints of Kepler planets	40
2.2	Parameters of the Jupiter-like perturber	42
2.3	KLD of initial and final period-radius distributions	71
2.4	Fitting parameters for the stability of Kepler planet systems	75
2.5	Piecewise fitting parameters for stability of Kepler planet systems with inclined perturbers	75
2.6	Minimum eccentricity requirement for planet crossings	80
2.7	Unbound planets in Kepler planet systems with and without perturb- ing bodies	81
3.1	Mass-luminosity relationship	106
3.2	Table of evolution timescales	107
4.1	Stellar phases in the EEP track files	132
4.2	Equivalent FSPS phases located in the equivalent evolutionary point (EEP) track files	133
4.3	Interpolation benchmarks	135
A.1	Runge-Kutta Cash-Karp parameters	163
A.2	Stability of long-term integrations	169

List of acronyms

BH black hole

CB carbon burning

CDF cumulative distribution function

CHeB core helium burning

CO carbon-oxygen

COMPAS Compact Object Mergers: Population Astrophysics and Statistics

EEP equivalent evolutionary point

FFT fast fourier transform

FSPS Flexible Stellar Population Synthesis

HB hydrogen burning

HPC high-performance computing

HVS hypervelocity star

IMF initial mass function

KDE kernel density estimation

KLD Kullback-Leibler divergence

LC loss cone

LK Lidov-Kozai

NS neutron star

MBH massive black hole

MC Monte Carlo

MCMC Markov Chain Monte Carlo

MESA Modules for Experiments in Stellar Astrophysics

MIST MESA Isochrones and Stellar Tracks

MMR mean motion resonance

MNRAS Monthly Notices of the Royal Astronomical Society

MS main sequence

PDF probability distribution function

RGB red giant branch

RLOF Roche-lobe overflow

SN supernova

SSE single-star evolution

TDE tidal disruption event

WDCS white dwarf cooling sequence

WR Wolf-Rayet

ZAMS zero-age main sequence

Chapter 1

Introduction

Astronomy has been one of the longest-studied subjects in history, beginning thousands of years ago with the first observations using just the naked eye. Jumping to the near-present, there have been vast improvements to both ground and space-based telescopes, ever-improving their performance. The first confirmation of an extrasolar planet detection occurred in 1992 (Wolszczan and Frail 1992), and since then the number of detections has grown at an ever-increasing rate. The two most popular methods for detecting planets are the radial velocity and transit methods, with the Kepler space telescope using the latter method. As of today there are 3,488 confirmed exoplanets (NASA 2017), with the Kepler telescope responsible for over two-thirds. The population of detected planets are helping us to understand the structure of planetary systems, and also giving insight into their potential formation history. The first heliocentric model of the Solar System was proposed over two thousand years ago, in the 3rd century BC by Aristarchus of Samos (Berggren and Sidoli 2007), with each planet on a circular orbit around the Sun. However, it wasn't until much later that this model was adopted. It reappeared under Nicolaus Copernicus in the 16th century, and was improved upon by Johannes Kepler by considering the orbits instead as ellipses, along with the three well-known laws of planetary motion. Newton's theory of gravity helped explain these laws, and these laws are still in use today.

Thanks to telescopes operating at many different wavelengths, we can even perform observations of the Galactic Centre. Light at optical wavelengths is blocked by the dust between us and the centre (Osterbrock and Ferland 2006), but observations in the X-ray, millimetre and radio bands can penetrate this dust and probe the properties of the gas residing at the centre. Karl Jansky build an antenna which could receive radio signals, and in 1932 discovered a background signal (Jansky 1933a; Jansky 1933b) which we now know originates from a region in the centre of the Milky Way known as Sagittarius A. Observations of this region, including the motion of its stars around what appears to be a very compact object, suggests that

a $\sim 4 \times 10^6 M_{\odot}$ massive black hole (MBH) residing at the Galactic Centre is the source (Ghez et al. 2008).

Even these detailed observations have limitations. For example, we only directly obtain the current state of an observed system. Some systems take millions to billions of years to evolve, and observing for this length of time is unfeasible. Theoretical models coupled with these observations can attempt to infer the history of the system as well as other properties which cannot be observed. Alongside this we also have another tool at our disposal; n-body simulations. These can probe both the potential dynamical history and future of a given dynamical system to help constrain a system's formation history and fate. Whilst only a general solution of the two-body problem exists, there are various approximations and applications which can be used to improve the accuracy of integrating a given n-body system (e.g. treating planets as perturbations from a dominant central-Keplerian potential, or the restricted three-body problem where one body is treated as a test particle). The first direct gravitational n-body simulation was performed in 1960 for clusters of up to 16 stars (von Hoerner 1960). Since then there have been vast improvements to the performance of computers through developments in transistor technology, with a huge increase in both the clock speed and the availability of many cores via high-performance computing. Simulations containing hundreds of billions of particles are now possible (Kim et al. 2011; Angulo et al. 2012), and smaller simulations of $n \lesssim 10$ bodies are trivial to evolve for millions of years on individual CPU cores. There are generally different approaches when integrating a small number of bodies compared to a large number. Direct integrations require $O(n^2)$ evaluations to calculate the interactions between each pair of bodies, but approximations such as tree code or particle mesh methods can be used to divide large n-body simulations into smaller cells or meshes, reducing the complexity of the problem to $O(n \log n)$. These simulations have been used in a variety of areas of Astrophysics; from the evolution of the matter distribution of the Universe over time into large-scale structures and

galaxies in the Millenium suite of simulations (Springel et al. 2005; Boylan-Kolchin et al. 2009; Angulo et al. 2012), dynamics of stars orbiting a MBH (Antonini et al. 2010; Prodan et al. 2015; Stephan et al. 2016), to the dynamical evolution of the planetary systems including the Solar System (Chambers et al. 1996; Barnes and Quinn 2004; Batygin and Laughlin 2008) ¹. N-body simulations, too, have their own limitations; integration errors that grow with longer integrations, and either ignoring or approximating additional effects such as general relativistic precession. However, they can still be useful for statistical analysis by performing many integrations of a population covering some defined parameter space, which is where the work in this thesis comes in.

The thesis is separated into three projects, each located within their own chapter. Chapter 2 takes a look at the period-radius distribution of planets observed by the Kepler telescope, and using this distribution, n-body simulations of planetary systems are performed to analyse the stability of this distribution after integration. This is probed further by considering an additional giant in wider orbits outside of those observable by Kepler, which interact more strongly with the other inner planets. Following this, chapter 3 moves to dynamics of stellar binaries orbiting a massive central black hole, as part of a nuclear cluster of stars. The focus of this chapter is the dynamics of stellar binaries on eccentric orbits around the MBH that are located in the empty loss cone (LC), and so survive multiple orbits whilst being tidally perturbed by the MBH as a three-body system. This allows for the eccentricities of the binary to grow and produce mergers, and depending on the stellar properties of the merger product are potential progenitors to producing relativistic jets as they become tidally disrupted by the MBH. Lastly, chapter 4 covers the ongoing work in producing a rapid population synthesis code which can produce stellar evolutionary tracks of a star given an initial mass and metallicity. This code

¹References given here are only a few examples of work in each area, and far from an exhaustive list

is based on interpolating between stellar evolutionary tracks generated by MESA Isochrones and Stellar Tracks (MIST) (Choi et al. 2016), which provide evolutionary tracks at regular mass and metallicity intervals. This final chapter does not contain work on n-body simulations directly, but shows progression towards developing code which can be incorporated into the n-body simulations of the previous two chapters to consider the effect of stellar evolution on the dynamical evolution of these systems. For instance, stars evolving from the main sequence may expand to many times their original radii, which can engulf planets on reasonable close orbits (which is expected to happen to the Sun, where the inner planets will be encompassed). This same expansion can also have an effect on the dynamics of binaries around an MBH, as it alters the separation required for mergers even without considering stellar binary evolution where common envelopes and Roche-lobe overflow (RLOF) can occur (and the state of the system at the time of collision will determine the properties of the merger product).

References

- [1] R. E. Angulo et al. “Scaling relations for galaxy clusters in the Millennium-XXL simulation”. In: MNRAS 426 (Nov. 2012), pp. 2046–2062. DOI: 10.1111/j.1365-2966.2012.21830.x. arXiv: 1203.3216.
- [2] F. Antonini et al. “Tidal Breakup of Binary Stars at the Galactic Center and Its Consequences”. In: ApJ 713 (Apr. 2010), pp. 90–104. DOI: 10.1088/0004-637X/713/1/90. arXiv: 0909.1959.
- [3] Rory Barnes and Thomas Quinn. “The (In)stability of Planetary Systems”. In: *ApJ* 611 (Aug. 2004).
- [4] K. Batygin and G. Laughlin. “On the Dynamical Stability of the Solar System”. In: ApJ 683, 1207-1216 (Aug. 2008), pp. 1207–1216. DOI: 10.1086/589232. arXiv: 0804.1946.
- [5] J. L. Berggren and N. Sidoli. “Aristarchus’s *On the Sizes and Distances of the Sun and the Moon*”. In: *Archive for History of Exact Sciences* 61 (May 2007), pp. 213–254.
- [6] M. Boylan-Kolchin et al. “Resolving cosmic structure formation with the Millennium-II Simulation”. In: MNRAS 398 (Sept. 2009), pp. 1150–1164. DOI: 10.1111/j.1365-2966.2009.15191.x. arXiv: 0903.3041 [astro-ph.CO].

-
- [7] J. E. Chambers, G. W. Wetherill, and A. P. Boss. “The Stability of Multi-Planet Systems”. In: *Icarus* 119 (Feb. 1996), pp. 261–268. DOI: 10.1006/icar.1996.0019.
- [8] J. Choi et al. “Mesa Isochrones and Stellar Tracks (MIST). I. Solar-scaled Models”. In: *ApJ* 823, 102 (June 2016), p. 102. DOI: 10.3847/0004-637X/823/2/102. arXiv: 1604.08592 [astro-ph.SR].
- [9] A. M. Ghez et al. “Measuring Distance and Properties of the Milky Way’s Central Supermassive Black Hole with Stellar Orbits”. In: *ApJ* 689, 1044–1062 (Dec. 2008), pp. 1044–1062. DOI: 10.1086/592738. arXiv: 0808.2870.
- [10] K. G. Jansky. “Electrical phenomena that apparently are of interstellar origin”. In: *Popular Astronomy* 41 (Dec. 1933), p. 548.
- [11] K. G. Jansky. “Radio Waves from Outside the Solar System”. In: *Nature* 132 (July 1933), p. 66. DOI: 10.1038/132066a0.
- [12] J. Kim et al. “The New Horizon Run Cosmological N-Body Simulations”. In: *Journal of Korean Astronomical Society* 44 (Dec. 2011), pp. 217–234. DOI: 10.5303/JKAS.2011.44.6.217. arXiv: 1112.1754 [astro-ph.CO].
- [13] NASA. *Exoplanet and Candidate Statistics*. Accessed: 29/05/2017. NASA. May 2017. URL: https://exoplanetarchive.ipac.caltech.edu/docs/counts_detail.html.
- [14] D. E. Osterbrock and G. J. Ferland. *Astrophysics of gaseous nebulae and active galactic nuclei*. 2006.
- [15] S. Prodan, F. Antonini, and H. B. Perets. “Secular Evolution of Binaries near Massive Black Holes: Formation of Compact Binaries, Merger/Collision Products and G2-like Objects”. In: *ApJ* 799, 118 (Feb. 2015), p. 118. DOI: 10.1088/0004-637X/799/2/118. arXiv: 1405.6029.

- [16] V. Springel et al. “Simulations of the formation, evolution and clustering of galaxies and quasars”. In: *Nature* 435 (June 2005), pp. 629–636. DOI: 10 . 1038/nature03597. eprint: astro-ph/0504097.
- [17] A. P. Stephan et al. “Merging Binaries in the Galactic Center: The eccentric Kozai-Lidov mechanism with stellar evolution”. In: *ArXiv e-prints* (Mar. 2016). arXiv: 1603.02709 [astro-ph.SR].
- [18] S. von Hoerner. “Die numerische Integration des n-Körper-Problemes für Sternhaufen. I”. In: *ZAp* 50 (1960).
- [19] A. Wolszczan and D. A. Frail. “A planetary system around the millisecond pulsar PSR1257 + 12”. In: *Nature* 355 (Jan. 1992), pp. 145–147. DOI: 10 . 1038/355145a0.

Chapter 2

The stability of the observed
period-radius distribution of
planets

2.1 Introduction

The first confirmed discovery of exoplanets occurred in 1992, where several planets were observed to be orbiting a millisecond pulsar (Wolszczan and Frail 1992). Since then thousands of planets have been discovered with many more candidates to be confirmed, with radial velocity and transit methods being the most popular. By far the most successful planet-hunting mission, the Kepler mission has 2,000 confirmed discoveries (NASA 2017a) by observing planets as they cross in front of their host stars. We are now at an exciting stage where there are enough detections to perform analysis on the discovered population, and from it attempt to infer statistical properties of the overall population of planets. Each method of detecting planets have their own advantages and disadvantages. With the radial velocity method, more massive planets produce a larger Doppler velocity on their host star and are more likely to be detected. The Doppler velocity is also larger for planets in close orbits. This method yields the minimum mass of the planet, as the observed component of the star's velocity depends on the inclination of the orbit. For the transit method used in the Kepler mission, larger planets are again easier to detect as they produce a larger reduction in the light received from the host star. The probability of a transit occurring in the line of sight between the star and the observer is also inversely proportional to the semimajor axis of orbit, meaning that planets in wider orbits are less likely to be detected.

The observed population of planets and planet candidates can be modelled, after ruling out likely false-positives (some candidates may turn out to be brown dwarf stars) and also correcting for some of the selection effect biases. Applying this to the population of Kepler candidates yields a bivariate log-normal distribution in planetary radius and orbital period (Aldridge and Stroud 2014). This distribution can then be used to produce planetary systems, which can be numerically integrated to measure their dynamical stability over time. There are multiple criteria to measure

the stability of a system. One simple requirement would be that all planets remain gravitationally bound to the host star, but more stringent requirements could include for the order of the planets to remain constant. However, this observed population is likely incomplete. The Kepler telescope needs to observe two transits for the observation to be considered a candidate. Based on the length of observations, this sets an upper limit on the orbital period of detectable planets to just over 3 years. Applied to our own Solar system, this would mean that the 4 outer planets would never be found by Kepler. These outer giant planets drive the dynamical evolution of our Solar system. They are responsible for the Kirkwood gaps in the asteroid belt, and Jupiter may have previously ejected a planet in the past (Cloutier et al. 2015). In the next few billion years there is also potential for Mercury’s orbit to be sufficiently perturbed by Jupiter that it will eventually collide with an inner planet, the Sun or be completely ejected (Batygin and Laughlin 2008).

This work aims to investigate the stability of planetary systems. The Monte Carlo method is used to generate planets in these systems based on the observed period-radius distribution (Aldridge and Stroud 2014), and 2,000 systems are generated. These systems are integrated for 1 million orbital periods of the innermost planet, and their stability is measured both by the ordering of planets by semimajor axis and the frequency of planet ejections. Further integrations are performed of the same systems with the addition of a giant outer perturbing body, which would be undetectable by Kepler. The parameters of this body are chosen to be Jupiter-like, and this body is placed in both an aligned orbit and inclined ($i_{\text{mutual}} \sim 50^\circ$) orbit relative to the inner planets to compare the effects of inclination. The difference in stability of these systems with and without an external perturbing body works towards constraining the presence of giant planets in the outer unobservable regions of planetary systems, which due to their mass tend to dominate planet-planet interactions. The stability timescales of these planetary systems is predicted based on the spacing of these planets, using a similar method to Chambers et al. (1996),

where it is expected that systems with closely-spaced planets become unstable on shorter timescales than those with widely-spaced planets. The results of the numerical simulations are compared with current observations of real multi-planet systems detected by Kepler.

In addition, a small number of planetary systems which remain stable by semimajor axis ordering are selected for long term \sim Gyr integrations. These systems are used to check against the stability timescale predictions, and also to obtain some results for timescales which approach the age of our own Solar system. The results of these integrations are presented in the appendix in section A.7.

This chapter is organised as follows: in section 2.2 I mention relevant theory on obtaining the period-radius distribution, measuring the stability of planetary systems and how resonances between planets can affect the dynamical evolution of the system. In section 2.3 I take a look at previous work in the field. Section 2.4 gives details on the methods used to generate and integrate the systems, as well as the analysis performed. Results can be found in section 2.5, with a summary and discussion following in sections 2.6 and 2.7.

2.2 Theory

This section contains the theory for obtaining the period-radius distribution and the distribution of the number of planets per star from the selected Kepler candidates and also important dynamical processes responsible for the evolution of systems, including mean motion resonances (MMRs) and secular interactions.

2.2.1 The period-radius distribution of planets

In this work, a bivariate log-normal distribution was used to generate the period and radius of each planet. The parameters of this distribution were fit to 3,000 selected Kepler candidates, removing likely false-positives and correcting for selection effects due to the geometric probability of observing a transit. The distribution can be written as:

$$\mathcal{N}(x, \mu, \Sigma) = \frac{1}{\sqrt{4\pi^2|\Sigma|}} \exp \left[-\frac{1}{2}(x - \mu)^T \Sigma^{-1}(x - \mu) \right], \quad (2.1)$$

with:

$$x = \begin{bmatrix} \ln P \\ \ln R \end{bmatrix}, \quad \mu = \begin{bmatrix} \langle \ln P \rangle \\ \langle \ln R \rangle \end{bmatrix}, \quad (2.2)$$

and $\Sigma = cov(\ln P, \ln R)$ is the covariance matrix. P and R are the orbital period and radius of the planet respectively. The fit of Kepler candidates to this distribution was performed using Markov Chain Monte Carlo (MCMC) by Farr et al. (2014) and Aldridge and Stroud (2014), and in this work samples of the obtained probability distribution function (PDF) are used to generate planetary systems. When generating planetary systems in this work, we draw from a Poisson distribution with mean and variance λ equal to the expected number of planets in planetary systems, which has been calculated in Farr et al. (2014).

This distribution has been obtained from observed planetary systems which have existed for billions of years. This means we expect that systems containing just these Kepler planets will remain stable over the course of the integrations. What will be important is how the stability and evolution of these systems is affected by the presence of giant Jupiter-like perturbing bodies. Systems consisting of just Kepler planets will then serve as a good baseline for drawing comparisons, and also are potentially useful for producing statistics to measure long-term stability of

planetary systems.

Each planet is drawn independently of every other planet in a given system, which is likely unrealistic given that the period-radius distribution of planets is likely correlated with multiplicity. This is because planets in a multi-planet system will have a minimum spacing between them to remain stable for long enough have been observed, and so for higher multiplicity systems you would expect this distribution to be spread over a wider range. However, the vast majority planets that have been observed all belong to different systems and there are too few multi-planet systems observed to obtain a distribution for each multiplicity. This means that a number of systems will be generated where planets are initially very close to each other, and these will likely become unstable on very short timescales.

2.2.2 Close encounters and stability

Planets that approach too closely to each other can have their orbits around the central star disrupted. The order of magnitude of the distance where encounters become close can be calculated by looking at a planet's Hill sphere (also known as the Roche sphere). This sphere is the volume where the planet's gravitational influence is stronger than that of any other body in the system, and any satellite orbiting within this sphere should approximately be stable. Therefore, in the case of multiple planets orbiting a star, a planet which enters another's Hill sphere will be strongly perturbed. A two-body system can be considered of masses M_1 and M_2 at positions \vec{r}_1 and \vec{r}_2 respectively. Then, a third test mass in the system m located at position \vec{r} will feel a total gravitational force from the other two bodies as:

$$\vec{F} = -\frac{GM_1m}{|\vec{r} - \vec{r}_1|^3}(\vec{r} - \vec{r}_1) - \frac{GM_2m}{|\vec{r} - \vec{r}_2|^3}(\vec{r} - \vec{r}_2), \quad (2.3)$$

where G is the gravitational constant. The radius of the Hill sphere can be found by looking for positions where the third body remains in a constant position relative to the other two bodies. We can move to the centre of mass co-rotating frame of M_1 and M_2 , which rotates with a constant angular velocity Ω given from Kepler's second law:

$$\Omega = \frac{2\pi}{P}, \quad (2.4)$$

$$= \sqrt{\frac{G(M_1 + M_2)}{R^3}}, \quad (2.5)$$

where P is the orbital period and R is the separation of bodies 1 and 2. There are two additional contributions to the force on m in this frame:

$$\vec{F}_\Omega = \vec{F} - 2m \left(\vec{\Omega} \times \frac{d\vec{r}}{dt} \right) - m\vec{\Omega} \times (\vec{\Omega} \times \vec{r}), \quad (2.6)$$

$$= \vec{F} + F_{\text{cor}}^\vec{r} + F_{\text{cen}}^\vec{r}. \quad (2.7)$$

$F_{\text{cor}}^\vec{r} = -2m \left(\vec{\Omega} \times \frac{d\vec{r}}{dt} \right)$ is the coriolis force and $F_{\text{cen}}^\vec{r} = m\vec{\Omega} \times (\vec{\Omega} \times \vec{r})$ is the fictitious centrifugal force. In this coordinate system, bodies 1 and 2 both lie along the x-axis with positions \vec{r}_1 and \vec{r}_2 , given by:

$$\vec{r}_1 = -\frac{M_2}{M_1 + M_2} R \hat{i}, \quad (2.8)$$

$$= -\mu_1 R \hat{i}, \quad (2.9)$$

$$\vec{r}_2 = \frac{M_1}{M_1 + M_2} R \hat{i}, \quad (2.10)$$

$$= \mu_2 R \hat{i}. \quad (2.11)$$

where R is the separation between the two bodies. The frame rotates at a rate Ω about the z-axis, $\vec{\Omega} = \Omega \hat{k}$, and our test mass lies in the orbital plane at position $r = x(t)\hat{i} + y(t)\hat{j}$. Equilibrium points are locations where the velocity $\vec{v} = d\vec{r}/dt = 0$, and $\vec{F}_\Omega = 0$, so a test mass at this point will be stationary in this frame and feel no

overall force. \vec{F}_Ω can be decomposed into vector components as:

$$\vec{F}_\Omega = \begin{bmatrix} -\frac{GM_1m(x+\mu_1R)}{((x+\mu_1R)^2+y^2)^{3/2}} - \frac{GM_2m(x-\mu_2R)}{((x-\mu_2R)^2+y^2)^{3/2}} + m\Omega^2x \\ -\frac{GM_1my}{((x+\mu_1R)^2+y^2)^{3/2}} - \frac{GM_2my}{((x-\mu_2R)^2+y^2)^{3/2}} + m\Omega^2y \\ 0 \end{bmatrix}. \quad (2.12)$$

We can make use of the substitution $G = \Omega^2 R^3 / (M_1 + M_2)$ from equation 2.4 to simplify the expression for the force:

$$\vec{F}_\Omega = \begin{bmatrix} m\Omega^2 \left[-\frac{\mu_1(x+\mu_1R)^3}{((x+\mu_1R)^2+y^2)^3} - \frac{\mu_2(x-\mu_2R)^3}{((x-\mu_2R)^2+y^2)^{3/2}} + x \right] \\ m\Omega^2 \left[-\frac{\mu_1yR^3}{((x+\mu_1R)^2+y^2)^3} - \frac{\mu_2yR^3}{((x-\mu_2R)^2+y^2)^{3/2}} + y \right] \\ 0 \end{bmatrix}. \quad (2.13)$$

$\vec{F}_\Omega = 0$ has no closed-form solution by default. However, in the limit where $M_1 \gg M_2$ such that $\mu_1 \ll 1$ (like in the case of a star and a planet), located along x-axis are three solutions – known as the first three Lagrange points, and are given by (Murray and Dermott 1999, pp. 77–80):

$$\vec{L}_1 \approx \left[R \left[1 - \left(\frac{\mu_1}{3} \right)^{1/3} \right], 0, 0 \right] \quad (2.14)$$

$$\vec{L}_2 \approx \left[R \left[1 + \left(\frac{\mu_1}{3} \right)^{1/3} \right], 0, 0 \right] \quad (2.15)$$

$$\vec{L}_3 \approx \left[-R \left[1 + \frac{5}{12}\mu_1 \right], 0, 0 \right]. \quad (2.16)$$

L_1 and L_2 are located on the zero-velocity surfaces close to the smaller mass, and are an approximate measure of the radius of its gravitational sphere of influence. In a general sense, the L_1 and L_2 points sit on the Roche lobe of the second body – the region within which material is gravitationally bound to that body. The Roche lobe forms a teardrop shape containing the region of space where matter would be gravitationally bound to the body. An example showing the Lagrangian points

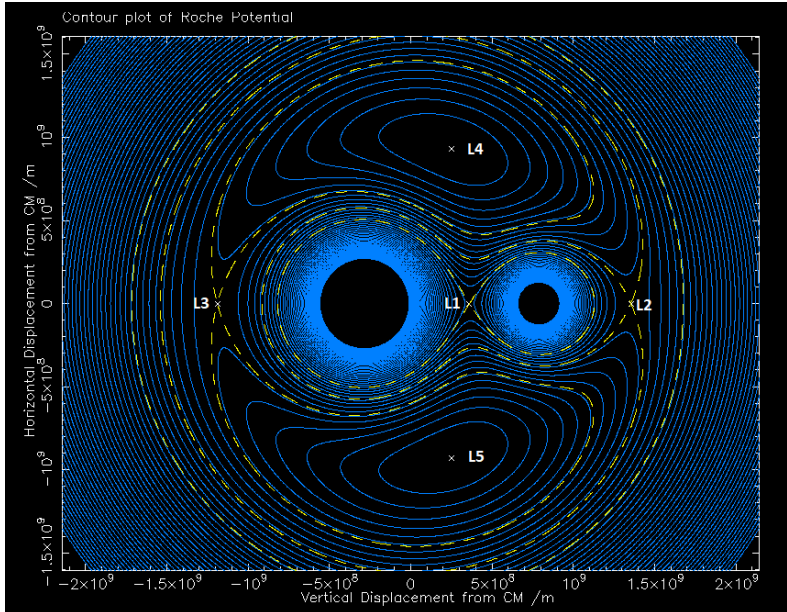


Figure 2.1: Equipotential lines of a two-body system in the co-rotating frame. The Lagrangian points are labelled, and the yellow-dashed lines show the equipotential surface at each point.

(marked by crosses) between two bodies is found in Figure 2.1.

The low mass of the second body relative to the first means the first two Lagrangian points sit at the same distance from the second mass. This distance can be written as:

$$R_{\text{Hill}} = \left| R \left[1 - \left(\frac{\mu_1}{3} \right)^{1/3} \right] - \mu_2 R \right|, \quad (2.17)$$

$$\approx \left| R \left[1 - \left(\frac{\mu_1}{3} \right)^{1/3} \right] - R \right|, \quad (2.18)$$

$$\approx R \left(\frac{m_2}{3m_1} \right)^{1/3}, \quad (2.19)$$

where R_{Hill} is the Hill radius. This radius is the approximate sphere for influence of the second less-massive body, and the approximations used here are valid for circular orbits, where R is equal to the semimajor axis a . Eccentric orbits introduce an additional term, essentially replacing the semimajor axis for periapsis distance such that $R_{\text{Hill}} \approx a(1 - e) \left(\frac{m_2}{3m_1} \right)^{1/3}$. If a second planet comes within a distance on the order of $\sim R_{\text{Hill}}$, it will receive a strong perturbation from the first planet.

Successive approaches will result in an increasingly unstable orbit, which can occur if the two planets have similar semimajor axes. Equation 2.19 doesn't consider the gravitational influence of the third body, whereas in planetary systems bodies 2 and 3 would both be planets with comparable mass. We can take into account perturbations from the third body by introducing the mutual Hill radius, $R_{\text{Hill,mut}}$, for two bodies of mass m_1 and m_2 orbiting a much more massive central body of mass M (Chambers et al. 1996):

$$R_{\text{Hill,mut}} = \left(\frac{a_1 + a_2}{2} \right) \left(\frac{m_1 + m_2}{3M} \right)^{1/3}, \quad (2.20)$$

where a_p is the semimajor axis of body p . In the case of $a_1 \sim a_2$, the mutual Hill radius in terms of the Hill radius of body 1 is $R_{\text{Hill,m}} \approx R_{\text{Hill}} \times ((m_1 + m_2)/m_1)^{1/3}$. Then, if m_1 is the more massive body the factor $((m_1 + m_2)/m_1)^{1/3}$ is at most $\sim 2^{1/3} \sim 1.26$. So the mutual Hill radius is of the order of the Hill radius of the more massive of the two planets when considering close encounters between neighbours, as long as $e \ll 1$.

2.2.3 Resonances

Resonance phenomena will occur when a physical system is driven at a frequency that forms a small integer ratio with the system's natural response frequency, and results in large-amplitude oscillations. A commonly used example of demonstrating a resonance is driving a swing; applying a periodic force applied at the natural frequency of the swing will cause the swing to rapidly increase its amplitude. The same effect can be observed in planetary dynamics where periodic forces, such as perturbations of a planet by that of another, occur at an integer ratio of natural frequency of the system, such as the orbital period. These perturbations can accumulate and result in instability of the system, or sometimes may have the opposite effect and increase long-term stability. There are three key types of resonances which apply to

the dynamical evolution of planetary systems. One type of resonance is a spin-orbit resonance, where an integer ratio exists between the rotation and orbital periods of a planet (such as the planet Mercury, which is found in a 3:2 spin-orbit resonance (Colombo 1965; Pettengill and Dyce 1965) or even our own moon, tidally locked in a 1:1 spin-orbit resonance). A second type are MMRs, likely the most well-known type where the orbital periods of two planets can be expressed as an integer ratio. Finally, secular resonances are where the periapsis or ascending nodes of two bodies precess at speeds that can also be represented as an integer ratio. The two types which are important to consider in this work are secular and mean motion resonances.

Mean-motion resonances

Mean-motion resonances appear throughout our Solar System, not just among planets but also between their natural satellites. The Laplace resonance of three of Jupiter's moons, Io, Europa and Ganymede, is one of the most well-known. The three moons are located in a 1:2:4 orbital resonance, where Io completes two and four orbits for every orbit of Europa and Ganymede respectively. The planets Pluto and Neptune are located in a 2:3 MMR, which is an example of a stable resonance, as it prevents the occurrence of close encounters between the two planets – even at the points where the two orbits cross (Malhotra 1995). MMRs are also partially responsible for instability in the asteroid belt, where regions corresponding to resonances with Jupiter in semimajor axis space are depleted (Lecar et al. 2001), known as the Kirkwood gaps. In fact, instability of asteroids in these regions are caused by the overlap of MMR with secular resonances of Jupiter and Saturn, and as a consequence their evolution is chaotic, with the asteroids eventually driven to high eccentricities and become disrupted as their orbits become planet-crossing (Moons and Morbidelli 1995). However, as mentioned previously, not all resonances are unstable. For example, there are relatively stable regions in the 2:1 MMR (Moons,

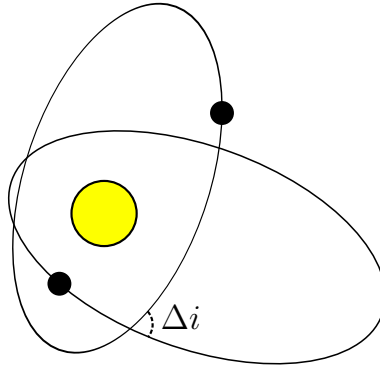


Figure 2.2: Relative inclination between two orbiting planets. Lidov-Kozai can occur when $\Delta i \gtrsim 39^\circ$

Morbidelli, and Migliorini 1998), although perturbations from other bodies can drive bodies out of these regions.

Secular resonances

Secular resonances are also present in the Solar System. The $g_a = g_6$ resonance exists at the inner edge of the asteroid belt between the asteroids and Saturn, where g_x is the precession frequency of the perihelion of body x (the planets are usually denoted as the n th planet from the Sun). In this region of the asteroid belt the perapsis of an orbit will precess at the same rate as Saturn's. Secular resonances generally result in the evolution of the eccentricity and inclination of bodies and cause instability via planet crossings. In some simulations of the Solar System, there is a future $g_1 = g_5$ between Mercury and Jupiter which cause instability in the inner planets (Jacques Laskar 2008; J. Laskar and Gastineau 2009).

Another resonance can arise between two bodies whose orbits are significantly inclined ($\gtrsim 39^\circ$) with respect to each other, and is known as a Lidov-Kozai (LK) resonance (or LK mechanism). First discovered by Lidov (1962), the pericentre of an orbiting body librates due to a resonance in the precession of the periapses and orbit normals. An image depicting the orbital planes can be seen in Figure 2.2.

An interesting effect of this resonance is that, in the test particle limit with the outer

body in a circular orbit, an oscillation of the eccentricity and inclination occur at the same frequency and the vertical component of the angular momentum is conserved (Y. Lithwick and S. Naoz 2011). This mechanism can drive eccentricities of the test particle to large values to produce orbit crossings and potentially collisions with the central body, whilst the semimajor axis is unaffected. Kozai (1962) investigated this effect on asteroids in the Solar System. When their orbits are significantly inclined with respect to Jupiter, secular evolution of the eccentricity caused the orbits to become sun-grazing. The work in this chapter generates systems where the inner Kepler planets are initialised approximately in the same orbital plane, so LK oscillations will not be produced in systems just consisting of these planets. However, this effect will be important when considering the evolution of systems with an added inclined perturber, as whilst the observed distribution of Kepler planets may suggest coplanarity in the majority of systems (e.g. Fang and Margot (2012)) the architecture of the outer regions of these systems are poorly observed and could contain outer planets in inclined orbits. It is therefore important to consider the potential effects of this mechanism on the stability of the inner planets, as this effect can cause the orbits of inner bodies to flip, even with small eccentricities of the outer perturbing body (S. Naoz et al. 2013). An order-of-magnitude calculation of the timescale in the test particle limit to quadrupole order is derived in Antognini (2015), yielding a timescale of:

$$\tau_{\text{LK}} \approx \frac{8}{15\pi} \left(1 + \frac{m_1}{m_3}\right) \left(\frac{P_{\text{out}}^2}{P_{\text{in}}}\right) (1 - e_{\text{out}}^2)^{3/2}, \quad (2.21)$$

Here m_1 is the mass of the central body and m_3 of the outer perturber ($m_2 = 0$ is the mass of the perturbed body in the test particle limit), P is the orbital period, e is the eccentricity and the subscripts in and out refer to the inner and outer orbits. This equation is derived under the assumption that the system is hierarchical, i.e. $P_{\text{out}} \gg P_{\text{in}}$, and so when considering a perturbing body in a Jupiter-like orbit this

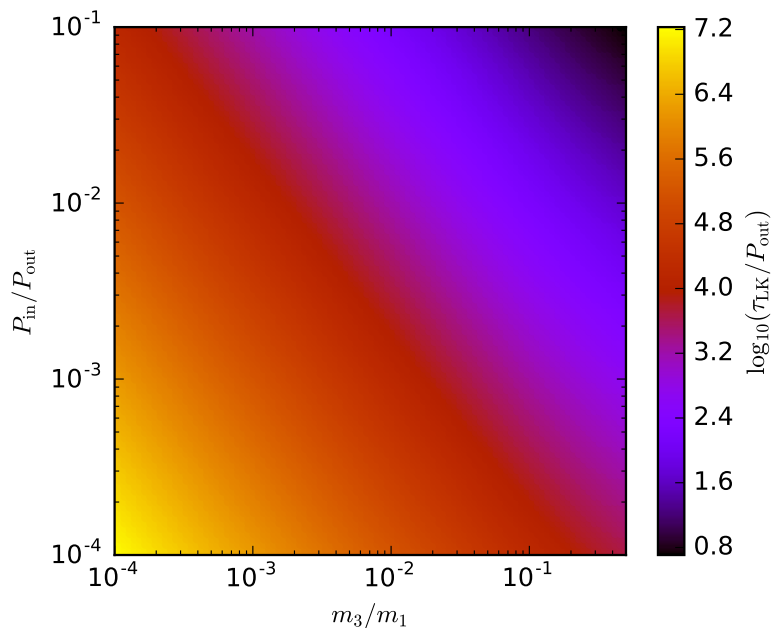


Figure 2.3: The LK timescale from equation 2.21 over a range of period ratios of the inner:outer orbit and mass ratios between the outer perturber and central body, plotted for $e_{\text{out}} = 0.0$.

would apply to inner planets on short periods, where $P_{\text{in}} \lesssim 0.12$ years. Figure 2.3 shows the LK for a range of orbital period ratios of the inner and outer bodies and a range of perturbing body masses. A Jupiter-like perturber orbiting a solar-like star will have a mass ratio $m_3/m_1 \sim 10^{-3}$, and in a Jupiter-like orbit would result in LK oscillations of an inner planet on a ~ 0.1 year orbit on a timescale of $\sim 10^5$ years. The timescale becomes very short for higher mass ratios, which you might expect for giant planets orbiting a low-mass star or even a planet orbiting a star with a binary stellar companion. The eccentricity of the outer body also has an effect, although at a value equal to that of Jupiter’s at $e \sim 0.5$ this is small. For a 50%, 90% and 99% reduction in the equivalent timescale for a perturber in a circular orbit requires eccentricities of $e \sim 0.608$, $e \sim 0.886$ and $e \sim 0.977$ respectively, although at high eccentricities the octupole-level coefficient $\epsilon_{\text{oct}} \equiv (e_{\text{out}}/(1 - e_{\text{out}}^2))(a_{\text{in}}/a_{\text{out}})$ becomes significant and reduces this timescale further (see equation 79, Antognini (2015)).

2.3 Previous works

2.3.1 Stability of hypothetical systems

The boundary of stability is well known for two planets in a circular orbit around their star. If the planets are spaced sufficiently far apart, they can be shown to never experience a close encounter if their spacing by semimajor axis satisfies the equation (Gladman 1993):

$$\frac{\Delta_a}{R_{\text{Hill,m}}} \gtrsim 2\sqrt{3}. \quad (2.22)$$

where $\Delta_a = a_2 - a_1$. Planets spaced within ~ 3.5 mutual Hill radii will eventually experience a close encounter where the planets approach within their mutual Hill radius and potentially destabilise the system. The situation is more complicated when increasing the number of bodies to the system, and this criterion no longer applies. Many three body systems with planets spaced to satisfy Equation 2.22 can still undergo a close interaction in a relatively short timescale, as found by Chambers et al. (1996). In fact, it was found that the time until the first encounter in planetary systems with a fixed number of planets of equal mass and equally spaced as Δ_a could be approximately predicted by the function $\log t = b\Delta_a/R_{\text{Hill,m}} + c$. The parameters b and c are dependent on the number of planets and their masses. This relationship was found to hold even with variations up to a factor of ~ 5 in planet masses and small $\sim 20 - 25\%$ variations from the mean planet spacing. This equation suggests, assuming that the relationship holds for higher planetary spacings and planetary masses, that there will always be a point in time where planets will perform a close approach, and likely mean that all planetary systems (of three bodies or more) will eventually become unstable. Work on two-planet stability was extended to hierarchical planets ($a_{\text{out}}/a_{\text{in}} \in [3 - 10]$) in eccentric and inclined orbits in Petrovich (2015), which found a boundary for systems to be long-term stable ($\gtrsim 10^8$ orbits of the innermost planet). The ratio of the periapsis of

the outer planet to the apoapsis of the inner planet needs to be spaced larger than $r_{p,\text{out}}/r_{a,\text{in}} \gtrsim 2.4[\max(\mu_{\text{in}}, \mu_{\text{out}})]^{1/3}(a_{\text{out}}/a_{\text{in}})^{1/2} + 1.15$, where μ_p is the mass ratio of planet p (inner or outer) to the host star.

A similar relationship was also observed by Zhou et al. (2007), this time between the spacing of equally-spaced planets (by mutual Hill radii) in eccentric coplanar orbits and the first orbit crossing times in multi-planet systems. The time difference between first encounters and orbit crossings are believed to be small (Duncan and Lissauer 1997), with either of them able to precede the other. For low mass planets ($\mu \equiv m_p/m_* = 10^{-10} - 10^{-4}$, the ratio of the mass of each planet to that of the star's), the orbit crossing time in years were found to be approximately calculated using $\log t_c = A + B \log(k_0/2.3)$, where $A = -2 + \tilde{e}_0 - 0.27 \log \mu$ and $B = (18.7 + 1.1 \log \mu)\tilde{e}_0$. $\tilde{e}_0 = e/h$, with e as the starting eccentricity for all planets in the system, $h = (a_{i+1} - a_i)/(a_{i+1} + a_i)$ and k_0 is the initial separation of the planets in units of the mutual Hill radius. This fit was observed to accurately predict the crossing times over a wide range of separations for systems, although a small correction was required at the lower end of the mass range $\mu = 10^{-9}$. Zhou et al. (2007) also find that mean-motion resonances between more massive planets was found to have a large impact on the crossing time. The best fit for the orbit crossing time, again in years, for high mass planets was found to be $\log t_c \approx -5.0 + 2.2k_0$ – only investigated for circular orbits. The 2:1 MMR present in massive-planet systems resulted in orbit crossings occurring up to $\sim 10^3$ times quicker than predicted by the best fit.

The timescale for orbital crossings was also investigated in Smith and Lissauer (2009) for planetary systems of three and five equal mass planets, equally spaced in mutual Hill radii (noting that in their definition they use the total mass of the system, rather than just the mass of the host star – but ignoring the effect of ignoring the masses of the planets is negligible.). They found that systems with planets within ~ 3 mutual Hill radii all started orbit crossing after ~ 10 years, and the correlation

between crossing time and planet spacing only became linear in the logarithm of time for larger spacings. Planets in these systems initially start well-spaced in longitude, λ , which they believe results in reduced variability in crossing times for systems with small spacings. Similarly to Chambers et al. (1996), they also find lower multiplicities to be more stable, but unlike Chambers et al. (ibid.) find no significant difference in stability for different planet masses unless the planets are spaced more than $\gtrsim 8.4$ mutual Hill radii apart. They also look at the impact of a Jupiter-like on the stability of the five-planet systems, and find that it reduces the time until planet crossing occurs by a small amount in a circular orbit, and a slightly larger effect is observed with Jupiter's eccentricity. Systems of planets with small eccentricities $e \sim 0.001$ and inclinations $\sin i \sim 0.001$ were discovered to start planet crossing by up to an order of magnitude sooner than having the planets in circular orbits. Systems of planets with alternating prograde/retrograde orbits (i.e. when counting from the closest planet to the star outwards, the evenly-numbered planets are orbiting in one direction and the odd-numbered are orbiting in the opposite direction) can survive for much longer times before orbit crossings occur, likely due to reduced interaction times between neighbouring planets.

The studies mentioned above mainly focussed on low mass planets ($\mu \ll 10^{-3}$), although Zhou et al. (2007) do find a difference between the evolution of a small number of high mass ($\mu \gtrsim 10^{-3}$) systems they investigated. Morrison and Kratter (2016) perform a more in-depth study on the stability of high mass planet systems and find that extrapolation of stability time from low mass data performs poorly at predicting the actual stability of these systems. Instead, the stability times for these systems fit better when expressing the spatial distance between semimajor axes in terms of the size of the overlap zone of first order MMRs. However, even rescaling this distance there is a large spread in instability time, which they believe to be at least partially due to second order resonances – which become more important as planets are perturbed to higher eccentricities where they are able to overlap with

first order MMRs, creating additional chaotic evolution.

2.3.2 The stability of the Solar System

The stability of planets in the Solar System has been investigated many times, and its evolution has been determined chaotic in numerous studies, e.g. G. J. Sussman and J. Wisdom (1988), J. Laskar (1989), J. Laskar (1990), G. J. Sussman and J. Wisdom (1992), and Y. Lithwick and Y. Wu (2011). The chaotic behaviour means that very small variations in the parameters of the Solar System will result in a large divergence over a long enough timescale. The Lyapunov time is a measure of the length of time it takes for the difference between two chaotic systems with variations in parameters to increase by a factor of e (note that e in this context is Euler's number). For the Solar System, this time is on the order of 5 Myr (J. Laskar 1989; J. Laskar 1999). This also means that it is impossible to determine the absolute fate of the Solar System with any appreciable accuracy for times much longer than the Lyapunov time, as the inability to perfectly measure the properties of every body in the Solar System (even if any objects other than planets are excluded) will result in many possible outcomes by the time the Sun reaches the end of its main-sequence life. Instead, to measure the stability of the Solar System, multiple integrations of the Solar System with small variations in parameters consistent with measured parameters can be performed for use with statistical analysis, as in J. Laskar and Gastineau (2009). In $\sim 1\%$ of their 5 Gyr-long simulations of the Solar System, with variations in orbital parameters consistent with measured uncertainties, Mercury will be driven to a high enough eccentricity for potential collisions with Venus as well as the Sun. One of the 2,501 integrations performed even resulted in instability of all of the terrestrial planets. So overall, it would appear that the Solar System is most likely to remain dynamically stable, at least until the Sun reaches the end of the main sequence. Even though it is not investigated in this work, stellar evolution can

play an important role on the stability of a planetary system. Post-main sequence, the Sun will experience two expansions in radius as it evolves on the red giant branch (RGB) followed by the asymptotic giant branch. These expansions will result in the Sun enveloping both Mercury and Venus (Rybicki and Denis 2001). The fate of the Earth is more uncertain, but Schröder and Connon Smith (2008) finds that the Earth will likely be engulfed towards the end of the RGB phase, as tides between the Earth and the convective envelope prevents the sufficient growth of Earth’s orbit due to solar mass loss to prevent it from escaping. Dynamically, the outer planets are expected to remain stable for billions of years after the end of the Sun’s main sequence phase (Duncan and Lissauer 1998).

2.3.3 Stability of exoplanetary systems

Less work has been performed on the dynamical stability of individual Kepler systems, although they can also be used to help constrain orbital parameters of detected systems (e.g. Kane (2015)) as well as investigate the possibility of planets existing in the outer parts of planetary systems where detectability remains poor (e.g. Jontof-Hutter et al. (2017)).

A. J. Mustill et al. (2015) find that migrating massive planets on eccentric orbits are often able to destabilise inner planetary systems modelled on three-planet Kepler Objects of Interest, although in a few cases the outer giant planet is ejected instead. This was followed up in A. J. Mustill et al. (2016), which looks at the stability of more three-planet Kepler Objects of Interest (removing likely false-positives and some cuts applied) as part of a system with an outer giant planet and a binary companion, or with an outer system of four giant planets. In the latter case, the four giant planets are spaced 4-6 mutual Hill radii apart, close to the boundary of stability. They find that the inner systems are stable in $\sim 75\%$ of cases in both configurations, where no planets are lost in the inner system after 10^7 years. Binary

companions which are in eccentric ($e \gtrsim 0.5$) orbits eject at least one planet in $\sim 50\%$ of cases, and more massive outer giant planets and tighter binaries also increase the likelihood for instability. Kozai oscillations can be observed in the systems with a significantly-inclined binary, and cause instability of the inner Solar System via driving the eccentricity of the giant planet and produce close encounters. In the systems containing just multiple giant planets, it was found that even an unstable outer system left the inner system intact in 63% of cases.

2.3.4 Comparison to this work

The majority of studies on the stability hypothetical multi-planet systems consider planets that are all evenly spaced in terms of mutual Hill radii and generally of equal mass. Unlike A. J Mustill et al. (2016), only hypothetical, compared to observed, systems are generated based on the bivariate log-normal distribution modelled on Kepler candidates, which also results in a larger range of multiplicities. With each planet being drawn independently from each other, this results in a large range in the potential gravitational interaction strength between neighbouring planets relative to the host star – even within a single system. This means there will likely be differences in the stability timescales of these systems when comparing to previous studies of hypothetical systems. This work will look at the overall stability of the period-radius distribution after integrations are performed as well as investigating the timescale over which these systems become unstable, and compare them to the results of previous studies. The timescale over which unstable systems become unstable can also be used to estimate when stable systems will become unstable, compared to the age of the Solar system (and the main-sequence lifetimes of average stars).

2.4 Methodology

This work comprises of three key stages: the generation of planetary systems based on Kepler candidate data, performing the n-body integrations and analysis. Details of each stage are given in the following sections.

2.4.1 Generating planetary systems

Every system is generated with the same host star, chosen to share the same parameters as the Sun. As a result, any planets with the same semimajor axis will also have the same orbital period under the assumption that the Keplerian potential of the star is dominant. Samples of the period-radius distribution described in section 2.2.1 are used to generate the period and radius of each planet, as well as the number of planets in a system.

Planet properties

The initial orbital period and radius of the planet are generated from the bivariate distribution discussed in section 2.2.1. The mass of the planet is calculated assuming a rock-like composition (due to their typical size), and uses the mass-radius relationship in Weiss and Marcy (2014) to convert from a radius to mass. The semimajor axis is simply found from Kepler’s third law, ignoring any other planets in the system where $a^3 = GMP^2/4\pi^2$. Here, G is the gravitational constant and M is the sum of the masses of the planet and the host star. Planets begin on nearly circular orbits in approximately the same orbital plane, consistent with observations in multi-planet systems (Xie et al. 2016). The argument of periapsis and the longitude of the ascending node are drawn uniformly between 0 and 2π . Table 2.1 shows the constraints on the orbital parameters in more detail, including the eccentricity and inclination of the orbit.

Symbol	Property	Constraint
M	Mass	$2.69(R/R_{\oplus})^{0.93}M_{\oplus}$
R	Radius	See section 2.2.1
a	Semimajor axis	Calculated from period (section 2.2.1)
e	Eccentricity	$\mathcal{N}(0.01, 0.001^2)$
i	Inclination	$\mathcal{N}(5.0^{\circ}, (2.5^{\circ})^2)$
ω	Arg. of periapsis	$\mathcal{U}(0, 2\pi)$
Ω	Long. of ascending node	$\mathcal{U}(0, 2\pi)$

Table 2.1: Constraints on the parameters used for generating the planetary systems, where applicable. $\mathcal{N}(\mu, \sigma^2)$ represents a normally-distributed variable with mean μ and standard deviation σ . $\mathcal{U}(a, b)$ is a uniformly-distributed variable in the range $(a, b]$. The planets therefore are slightly inclined to the reference plane.

In total, 2,000 planetary systems are created containing 7,850 planets generated from the period-radius distribution, yielding an average of 3.925 planets per system. Each planet is initialised at a random point in their orbit uniform in mean anomaly.

2.4.2 Numerical integrations

All integrations performed in this work make use of the *IAS15* integrator, found in the *REBOUND* package (Rein and Spiegel 2015). This is a 15th-order n-body integrator with adaptive step-size control. To begin with, each system is integrated for a total of one million inner orbital periods of the innermost planet belonging to that system. Systems are marked unstable if the order of the planets by their semimajor axis changes at any point during integration, and the time of the first order change is recorded. Integration then proceeds until completion of the one million inner orbits, and the final orbital parameters are then stored.

Only the initial and final properties of the systems are stored in the initial integrations due to the large number of systems integrated. To be able to analyse the evolution of systems in more detail, individual systems are selected to integrate and store the orbital parameters of each body periodically. 16 stable systems consisting of Kepler-only planets are selected for long-term integrations, with the aim of reach-

ing simulation times approaching ~ 1 Gyr. Another range of systems are selected and integrated for ~ 1 Myr with periodic output of orbital elements. These systems contain a mixture of perturbing bodies in the aligned and inclined configuration so we can observe the effect of having the more massive planet present, and see if the causes of instability differ from that of just Kepler-only systems. The evolution of the planets of these systems can be used to identify how systems either remain in a stable configuration or become unstable, including planet ejections, and see if they can be used to predict stability of other planetary systems.

Integrations in this work made use of University of Birmingham's BlueBEAR HPC, allowing multiple planetary systems to be integrated simultaneously across multiple nodes ¹.

2.4.3 Analysis of results

Stability

The first method that will be used to determine the stability of these systems is to check the proportion of systems which retain the same planet ordering by semimajor axis after one million inner orbital periods. The time where the first reordering event occurred is recorded during integration, so that the number of systems becoming unstable as a function of time can be found. The relatively large number of systems generated would require a vast amount of computation resources in order to integrate them all for \gtrsim Gyr timescales. To reduce this requirement, a small number of stable systems as judged by this method will be integrated for a longer period of time. 32 stable systems are selected and integrated for $\sim 10^8$ years², up to a factor of ~ 1000 times longer than the original one million inner orbits, far closer to the \sim Gyr

¹<http://www.birmingham.ac.uk/bear>

²32 systems can be integrated on a single node on the BlueBEAR high-performance computing (HPC) cluster with 1 system per logical core

timescale comparable to the age of the Solar System. These systems will be used as a probe to determine if the shorter integrations can be used as a reasonable probe for the long-term stability of systems. Additionally, a number of unstable systems will be integrated individually to determine the causes of instability. A second measurement of stability will be performed, relaxing the constraint for maintaining the same order of planets and just counting the fraction of planets which become gravitationally unbound from the host star and are ejected from the system. This is because some systems may undergo reordering of the planets, but potentially end up in a stable configuration and remain bound to the star.

Symbol	Property	Constraint
M	Mass	$U(0.5, 2)M_{\text{J}}$
a	Semimajor Axis	$\mathcal{N}(a_{\text{J}}, 0.1a_{\text{J}})$
e	Eccentricity	e_{J}
i	Inclination	$\mathcal{N}(i_{\text{J}}, 0.5^\circ) \parallel \mathcal{N}(50^\circ, 5^\circ)$
ω	Arg. of Periapsis	$\mathcal{U}(0, 2\pi)$
Ω	Long. of Ascending Node	$\mathcal{U}(0, 2\pi)$

Table 2.2: The parameters of the outer Jupiter-like perturber. The subscript J refers to Jupiter’s value for the relevant property. $\mathcal{N}(\mu, \sigma^2)$ represents a normally-distributed variable with mean μ and standard deviation σ . $\mathcal{U}(a, b)$ is a uniformly-distributed variable in the range $(a, b]$.

Two additional sets of integrations of the same 2,000 systems are performed for the same one million inner periods, adding a Jupiter-like perturber in an aligned orbit in the first set and in an inclined configuration in the second (recall that the lifetime of the Kepler mission and requiring two transits to be seen by the telescope means that these perturbers are unobservable by the telescope). This body will act as an external perturber in the planetary systems, and its larger mass compared to the other planets will increase the strength of gravitational interactions between planets relative to planet-star interactions. The exact distributions used to obtain the properties of the perturbing body can be found in Table 2.2, and they are randomly initialised uniform in mean anomaly. The first set of these new

integrations is performed with the perturber in an approximately coplanar orbit with the other planets, and a second set with a large mutual inclination between the orbital planes ($\sim 45^\circ$). The stronger perturbations should increase the number of unstable systems and ejected planets, and the presence of the outer giant planet could be a more realistic representation of a typical planetary system (and closer to the structure of our Solar System). When the perturbing bodies are in the inclined configuration, the inner planets are able to undergo LK oscillations and their eccentricities can be driven to large values, resulting in planet-crossing events and more close-approaches between planets. An approximate probability of a close encounter resulting from an eccentric planet crossing the orbit of another planet can be calculated by considering the circumference of an orbit that is crossed, and dividing it by the typical Hill sphere radius of a planet. This can be written as:

$$p(\text{CE}) = \frac{R_{\text{Hill}}}{C}, \quad (2.23)$$

where C is the circumference. For an ellipse, this results in:

$$p(\text{CE}) = \frac{R_{\text{Hill}}}{4a \int_0^{\pi/2} \sqrt{1 - e^2 \sin^2 \theta} d\theta}, \quad (2.24)$$

$$= \frac{(1 - e)m^{1/3}}{(3M)^{1/3} 4 \int_0^{\pi/2} \sqrt{1 - e^2 \sin^2 \theta} d\theta}, \quad (2.25)$$

with m the mass of the planet and M is approximately the mass of the host star. Note that this probability does not depend on the semimajor axis of the orbit. If we assume the planet that's orbit is crossed is approximately circular, then we can substitute in the circumference for a circle. Then we can simplify the expression to:

$$p(\text{CE}) \approx \left(\frac{m}{24\pi^3 M} \right)^{1/3}, \quad (2.26)$$

$$\sim 0.1 \left(\frac{m}{M} \right)^{1/3}. \quad (2.27)$$

Assuming $m \sim M_{\oplus}$ and $M \sim M_{\odot}$, the probability is roughly $\sim 0.15\%$. In a single orbit crossing event the chance of a close encounter is very small, but these planets have relatively short orbital periods of $\lesssim 1$ year. In just ~ 3000 planet crossings there is a 99% chance of a close encounter occurring, and this would only take a few thousand years if only one orbit was crossed per orbit of the eccentric planet. With multiple planets in a typical system, there is potentially multiple orbital crossings for each orbit of the eccentric planet around the host star, and each orbit of another planet will be crossed twice per orbit.

The results of this work are also compared to Chambers et al. (1996). The function to predict the time of the first encounter based on planet spacing (refer to section 2.3) is used to attempt to predict the stability timescales of Kepler planetary systems. There are, however, some differences between these two sets of planetary systems. In Chambers et al. (ibid.), the difference in masses between any two planets were no more than a factor of 5, whereas in this work the mass of planets can vary by over an order of magnitude without even considering the Jupiter-like perturbers. There is an even larger difference in the spacing of the planets; whilst Chambers et al. (ibid.) only varied the spacing slightly from a mean value each planet in this work is independently given an orbital period, meaning that any planetary system can have huge variations between any neighbouring planets. Another factor to consider is, in the initial integrations, only the time of first reordering by semimajor axis is recorded (τ_{stab}) rather than the first close encounter. These two timescales are probably comparable, as a close encounter is likely to cause some disruption to the system as well as successive close encounters occurring on a short timescale (every ~ 1000 years) once planets start to become orbit crossing. So the linear fit is attempted to predict the stability timescale of planetary systems with a fixed number of planets based on the spacing of the planets. As the variations in planet spacings are large, this fit will be attempted with both the average spacing between

neighbouring planets in a system and the closest spacing:

$$\log \tau_{\text{stab}} = b\Delta_a/R_{\text{Hill,mut}} + c, \quad (2.28)$$

$$\log \tau_{\text{stab}} = b\langle \Delta_a/R_{\text{Hill,mut}} \rangle + c, \quad (2.29)$$

where $\langle \Delta_a/R_{\text{Hill,mut}} \rangle$ is the arithmetic mean of $\Delta_a/R_{\text{Hill,mut}}$ for each set of neighbours. b and c will be found using a least-squares fitting algorithm, finding the minimum sum of vertical deviations $R^2 \equiv \sum_{i=1}^n (f(x_i, a, b) - y_i)^2$ over n points of data. $f(x_i, b, c)$ is set to either of Equations 2.28-2.29, with x_i equal to the (mean) planet spacing, y_i is the actual stability time, b is the gradient and c a constant. A minimum appears in R^2 when $dR^2/db = dR^2/dc = 0$, which occurs when (Press et al. 2002, pp. 666-668):

$$b = \frac{SS_{xy} - S_x S_y}{SS_{xx} - (S_x)^2}, \quad (2.30)$$

$$c = \frac{S_{xx} S_y - S_x S_{xy}}{SS_{xx} - (S_x)^2}, \quad (2.31)$$

with the variables S , S_j and S_{jk} (with j and k each as either x or y) as:

$$S \equiv \sum_{i=1}^n \frac{1}{\sigma_i^2}, \quad (2.32)$$

$$S_j \equiv \sum_{i=1}^n \frac{j_i}{\sigma_i^2}, \quad (2.33)$$

$$S_{jk} \equiv \sum_{i=1}^n \frac{j_i k_i}{\sigma_i^2}. \quad (2.34)$$

σ_i is the measurement error on i , which is set to 1 for all points. We can estimate the error on the parameters a and b using standard errors, given as (ibid., p. 668):

$$\text{SE}(b)^2 = \frac{S s^2}{SS_{xx} - (S_x)^2}, \quad (2.35)$$

$$\text{SE}(c)^2 = \frac{S_{xx} s^2}{SS_{xx} - (S_x)^2}, \quad (2.36)$$

where $s^2 \equiv \sum_{i=1}^n (y_i - \bar{y})^2 / (n - 2)$ is the estimator of the variance. This assumes a good fit, but allows a comparison between the equivalent parameters across the range of multiplicities of planets.

Measuring changes in the Kepler distribution

If we expect the observed distribution of planets to be a reasonably accurate compared with the true distribution, then we should expect that the distribution shouldn't change dramatically after the planetary systems are integrated. The initial and final distribution will be compared, measuring the difference between the two. Qualitatively, the appearance of the period-radius distribution can be examined for differences after integrations are performed.

We can also quantitatively compare by obtaining a kernel density estimation (KDE) of the initial and final distributions and calculating the difference between the two. The kernel density estimator of a function f using n identically and independently distributed samples x_1, x_2, \dots, x_n is defined as follows:

$$\hat{f}_h(x) = \frac{1}{n} \sum_{i=1}^n K_h(x - x_i), \quad (2.37)$$

$$= \frac{1}{nh} \sum_{i=1}^n K(x - x_i), \quad (2.38)$$

where h is the bandwidth, K_h is the scaled kernel and K is the kernel – a weighting function that is symmetric and is defined such that $\int_{-\infty}^{\infty} K(y)dy = 1$. The bandwidth h is a smoothing parameter. In this work we make use of the Gaussian kernel, $K(y) = e^{-y^2/2} / \sqrt{2\pi}$ and the bandwidth is selected based on Scott's rule (Scott 1992). The KDE is calculated uniformly in log-space in period and radius and the perturbing bodies are ignored.

Another method for comparing the two distributions is to calculate the Kullback-Leibler divergence (KLD), which can also be referred to as the relative entropy. This

is a measure of information that is lost when using one probability distribution (Q) to describe another (P). The KLD is calculated as follows (Kullback and Leibler 1951):

$$D_{\text{KL}}(P||Q) = \int_x p(x) \log \frac{p(x)}{q(x)} dx, \quad (2.39)$$

$$= \int_x \log \frac{P}{Q} dP, \quad (2.40)$$

where p and q are the probability densities for each of the distributions P and Q . A different base value can be used for the logarithm, and is chosen to be in base-2 for this work so that the information lost is measured in ‘bits’. The probability density of each distribution will be estimated using the same KDE of each distribution as described above. The KLD will be close to zero if the two distributions compared are similar to each other, with the lower limit of the KLD reaching zero when $P = Q$. As well as comparing the initial and final distributions of planets, the final distributions of the Kepler planets can also be compared across the various configurations of having no external perturbing body to one in a coplanar and highly-inclined orbit. This will allow the effect of the perturbers on the planets, particularly any migration.

Comparing the population of planets in stable and unstable systems

Comparing the distribution of all planets across all systems provides an overview but it is also important to identify any possible causes which result in the planets becoming unstable or even being ejected. Systems will be classified by looking at the spacing between the planets, in particular the smallest distance between any pair of planets by semimajor axis in the system in units of the largest Hill radius of the pair. The distance between a pair of planets, 1 and 2, using this definition is

therefore:

$$d_{12} = \frac{|a_1 - a_2|}{\max(R_{\text{Hill},1}, R_{\text{Hill},2})}, \quad (2.41)$$

with $R_{\text{Hill},p}$ as the Hill radius of planet p . It is expected that systems with planets that are well-spaced will remain stable as the perturbations between planets are small and unlikely to disturb their orbits around the star. The initial minimum distance between any pair of planets in a system will be known as d_{CPP} , and should provide some insight in predicting the stability of the systems even before integration. If the eccentricities of the planets remain small enough and interactions can be approximated as secular, the orbits will remain approximately circular and fixed, and d_{CPP} should accurately describe the typical distance between the strongest planet-planet interactions throughout the likely uneventful evolution of the system. Even in systems where some planets are driven to high eccentricities or migrate in semimajor axis to create stronger interactions, the initial value of d_{CPP} will likely have to be relatively small to create strong enough perturbations to evolve the orbits into these configurations. In the case of adding the external perturbing body may the d_{CPP} of systems that become unstable be larger than expected, as secular effects such as LK cycles can become important. The value of d_{CPP} for all stable and unstable systems will be investigated, to see if there is a well-defined boundary between systems that are more likely to stay stable or become unstable. The effect of external Jupiter-like perturbers on the boundary will also be explored.

The initial and final mean and standard deviation of the inclinations (ignoring perturbing bodies where applicable) are compared between stable and unstable systems. It is expected that the planets in stable systems will remain close to their initial inclination with a small standard deviation to indicate preservation of the disk-like structure. The mean inclination in unstable systems may increase significantly, depending on the number of planets that become unstable compared to the total number of planets (and whether the planet is ejected). A large final standard

deviation in the inclination will suggest break-up of the planetary disk.

Evolution of individual systems

Individual systems are chosen to be integrated to both find out if systems that are stable for the shorter one million orbital periods are also stable for longer timescales, and to look closely at the evolution of the orbital parameters of the planets over time. Periodic output allows the monitoring of the semimajor axis throughout integration to see how frequently planets reorder themselves, as well as planet crossings via the apses. Plotting the eccentricity against the inclination of each planet can make standard LK oscillations apparent (when the inclined perturber is added), where planets will approximately follow trajectories in $e-i$ space where the vertical projection of its angular momentum, L_z , is constant.

A search for secular resonances will be performed between pairs of planets by looking for coupled evolution of the semimajor axis and eccentricity between them. The output data of these parameters for each planet in a system are interpolated using cubic splines to obtain uniformly spaced points. This allows application of a fast fourier transform (FFT) on each data series to find frequencies at which the parameters oscillate at. A peak finding algorithm picks the 10 strongest peaks relative to the background (using a moving average of 20 surrounding points), which can be used to look for resonances. First order resonances are focussed on in this work, as they should dominate over any higher order resonances present in the systems. Potential resonances are flagged based on an integer multiple of one frequency being an integer multiple of another, with first order resonances meaning that the difference between the two integers is 1. This can be represented as:

$$af_1 - bf_2 = 0, \tag{2.42}$$

where f_1 and f_2 are the frequencies of two peaks being compared, and a and b are

the integer multiples, with $|a - b| = 1$ for first-order resonances. The width of the frequency bins after applying the FFT leads to some uncertainty in the frequencies of the peaks, and we take this source of error into account by modifying Equation 2.42 as follows:

$$af_1 - bf_2 \leq (a^2 + b^2)^{1/2} \Delta f, \quad (2.43)$$

where Δf is half of the frequency bin width. Pairs of frequencies that satisfy this condition are flagged as potential resonances between the two planets.

2.5 Results

The results of this project are split into two main sections. The first consists of the stability of the overall population, and measuring any differences in the period-radius distribution. The second section contains the results for individually chosen systems, where periodic properties of each body are stored during integration and evolution in orbital elements can be seen. Systems containing the Kepler planets are looked at initially in both cases, before proceeding to looking at the effects from adding the perturbing Jupiter-sized planet in the aligned and inclined configuration. Note that when systems are referred to as just stable or unstable, this means that they are considered stable by the order of the planets by semimajor axis. Other methods of stability will be explicitly mentioned.

2.5.1 Stability of the overall population

Numerical integrations of Kepler planets

Overall, 66.85% of systems containing just Kepler planets remain stable when monitoring the order of the planets over one million orbital periods of the innermost planet. A plot of the fraction of systems remaining stable over time is shown in

the left image of Figure 2.4. The rate of systems becoming unstable decreases over time, with $\sim 60\%$ of unstable systems becoming unstable within $\sim 10^3$ inner orbital periods and an almost (negative) linear relationship between the surviving fraction and $\log t$. Also shown in the same Figure is a plot of the length of time that unstable systems remained stable for, plotted against the smallest distance between any pair of planets in the system in units of the larger Hill radius of the pair. As expected, systems with smaller d_{CPP} are generally the first to become unstable by semimajor axis ordering, with a clump of systems becoming unstable within 10^3 concentrated at $d_{\text{CPP}} \lesssim 4$, and instability in systems with greater planet spacing take longer. However, it is found that even systems where the planets are well-spaced in semi-major axis ($d_{\text{CPP}} \gtrsim 10$) can undergo rearrangement of the planets within just one million orbital periods. This timescale is short (typically several magnitudes shorter than the age of the Solar System) considering the planets are initially in circular orbits and there is no massive perturbing body present in the system, inclined or otherwise.

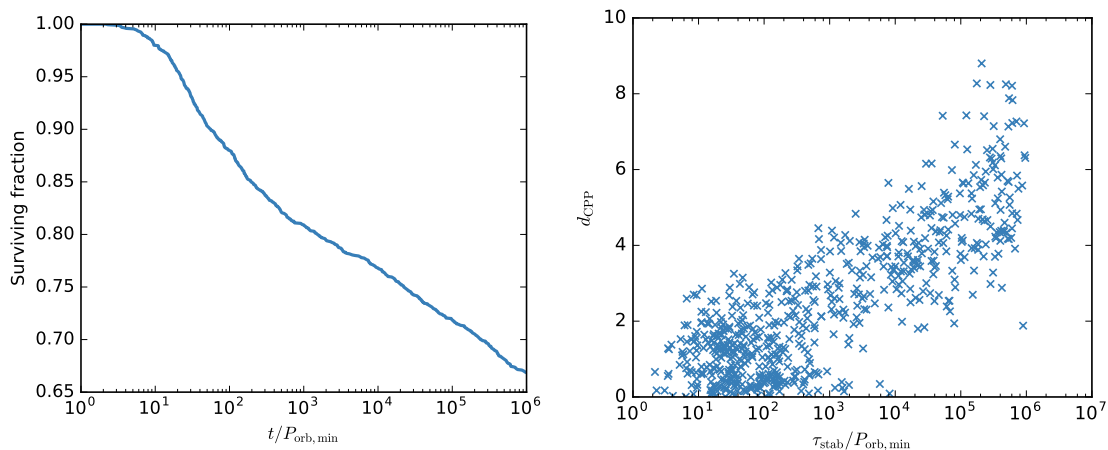


Figure 2.4: The plot to the left is the fraction of systems remaining stable versus integration time, determined by ordering of the planets. On the right is a scatter plot of the stability time of unstable systems versus the smallest planet pair distance in units of Hill radii, d_{CPP} .

Next the planet spacing is looked at in more detail, including in systems that remained stable during integration. Figure 2.5 contains histograms of d_{CPP} for both

stable and unstable systems. The left panel shows that all but three systems with $d_{\text{CPP}} \lesssim 3$ remain stable, and in contrast only a few systems with $d_{\text{CPP}} \gtrsim 9$ become unstable. It is likely that if the integrations proceeded for longer, the two remaining stable systems with $d_{\text{CPP}} \lesssim 3$ would eventually become unstable due to the relatively strong planet-planet interactions – unless they happen to be located in a resonance that protects the planets from close encounters (which is unlikely due to the random generation of planets in these systems). The boundary between the two states, where the number of stable systems and unstable systems is approximately equal, falls between $d_{\text{CPP}} \sim 5-6$.

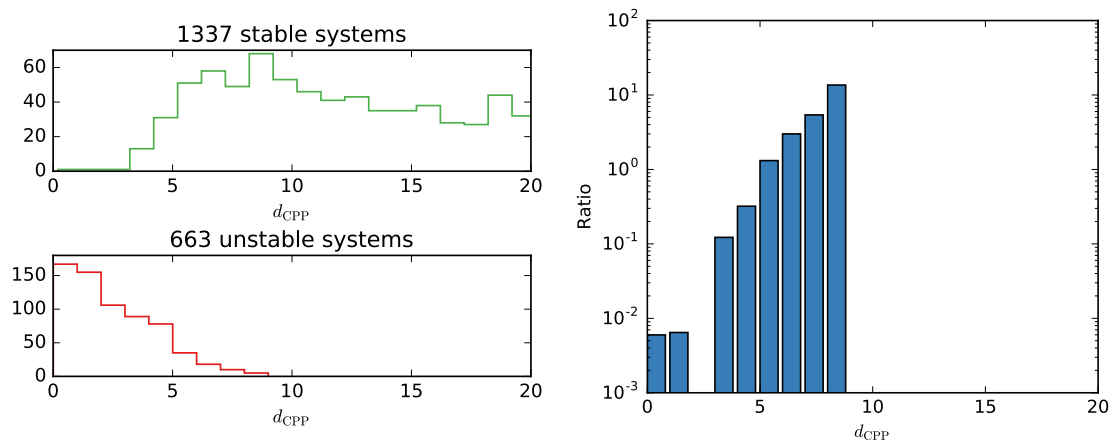


Figure 2.5: Histograms of planet spacings (by d_{CPP}) for both stable and unstable systems (left), and a histogram of the ratio of stable to unstable systems across planet spacing (right). Spaces are present in the right panel where no stable or unstable systems fall within a bin.

The frequency of multiplicities of Kepler planets are plotted for each system marked by stability in figure 2.6. It is immediately apparent that systems of fewer planets are much more likely to remain stable during integration, with the fraction of unstable systems increasing with larger systems. Drawing a larger number of planets from the same distribution makes it more likely for any two planets to have similar orbital periods, leading to close orbits in space and strong planet-planet interactions which can end up in instability. This is illustrated in Figure 2.7, with the left panel showing the spread of d_{CPP} of each system plotted against the number

of Kepler planets. The systems generally remaining stable can be seen to occupy $d_{\text{CPP}} \gtrsim 10$, but the range in this value decreases with increasing multiplicity as the system becomes more packed. The right panel displays the mean value for d_{CPP} for each multiplicity, with the standard error shown as a error bar in the y-axis. The negative trend is clear, although the standard error grows relatively large for $N_{\text{pl}} \gtrsim 10$ due to the low number of systems containing a large number of planets. In addition to the increase in the number of planets reducing the typical planet spacing, there will also be an effect from the increase in number of planets being able to potentially provide stronger planet-planet interactions relative to between a planet and the host star, especially if conjunctions occur.

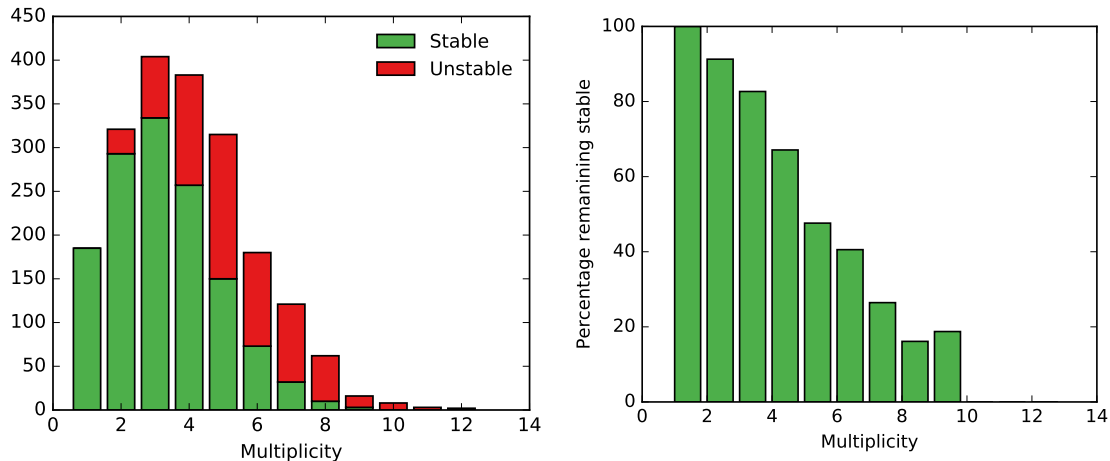


Figure 2.6: Frequency of each multiplicity of Kepler planets, marked by stability after one million inner orbital periods. Also shown in the right image is the percentage of systems remaining stable at each multiplicity.

Figure 2.8 shows the initial and final orbital period and radius of every Kepler planet, separated into belonging to a stable or unstable system. As the integrations only consider the treatment of planets as point-like particles, planets can only migrate along the y-axes in the graphs. Around the edges of the bulk of the distribution, individual stars can be seen to evolve in orbital period by comparing the two graphs, but on the whole, the distribution obtained after integration looks very similar to the initial distribution. Even when looking at stars belonging to the unstable systems, a lot of them remain at a similar position which suggests that not all of the planets

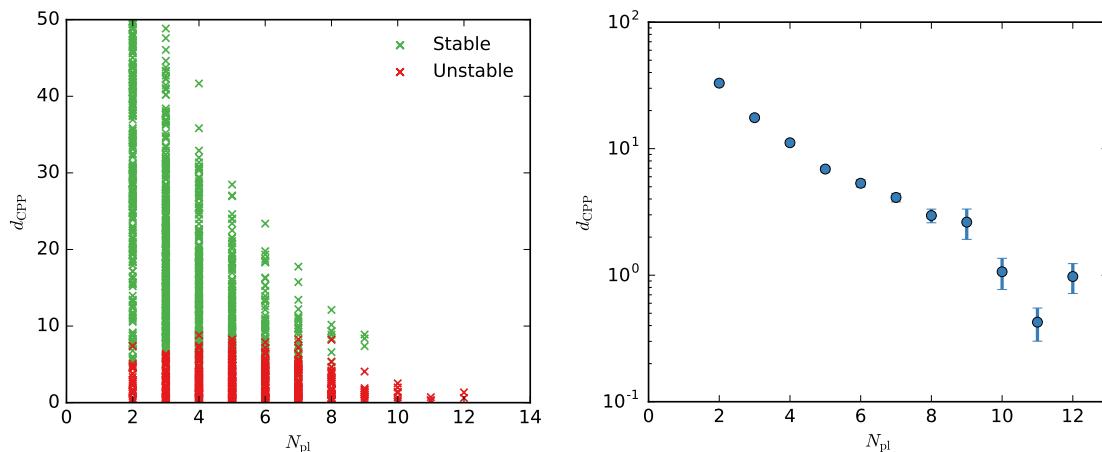


Figure 2.7: A scatter plot of the multiplicity of systems versus the smallest planet spacing (d_{CPP}) by stability is shown on the left and the mean d_{CPP} for each multiplicity is shown on the right, along with the standard error σ/\sqrt{N} .

are involved in the instability of unstable systems (e.g. it may be the case that two planets in a system may be initialised in very close orbits and swap throughout, with the remaining planets being unaffected). This figure can be reproduced using KDE, allowing a more quantifiable comparison between the initial and final distribution. Figure 2.9 shows a KDE of the initial distribution in the left panel, and the difference between the initial and final KDE in the right panel. The left panel clearly shows the bivariate log-normal distribution, with the right panel showing a migration of Kepler planets from the bottom part of the densest region to mainly higher orbital periods. Note that the scale on the right panel is far smaller, with the densest regions showing a $\sim 5\text{-}8\%$ change in density. This shows that the distribution is relatively stable during integration, even with a non-insignificant amount of systems being deemed unstable.

Whilst the orbital period (or equivalently, the semimajor axis) is used to measure the changes in the period-radius distribution, evolution of other orbital elements are also important when actually looking at the stability of planetary systems. Changes in eccentricity can create close encounters between planets without requiring any changes in the semimajor axis. Planets which become significantly inclined can also introduce LK oscillations of any internal planets, again resulting in exploration of

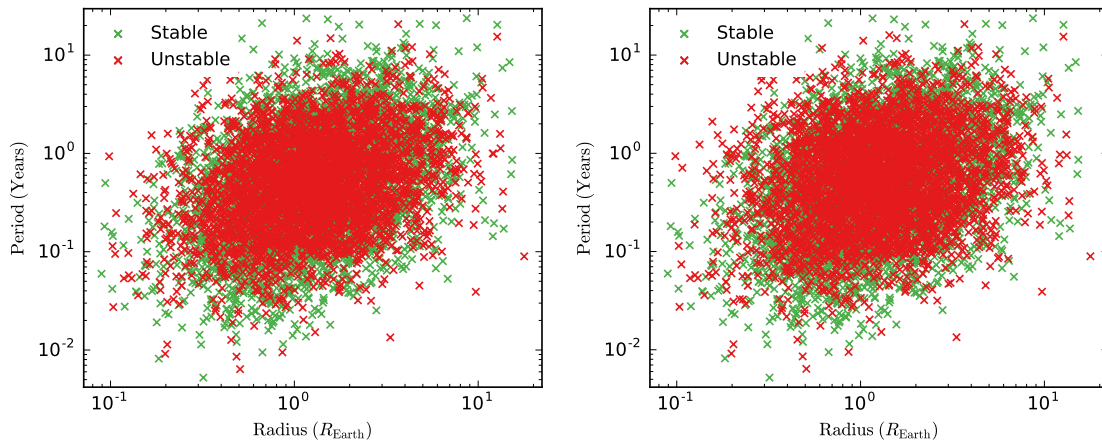


Figure 2.8: Scatter plots of the initial (left) and final (right) period and radius for each planet. The colour denotes whether that planet belongs to a system which is stable (green) or unstable (red).

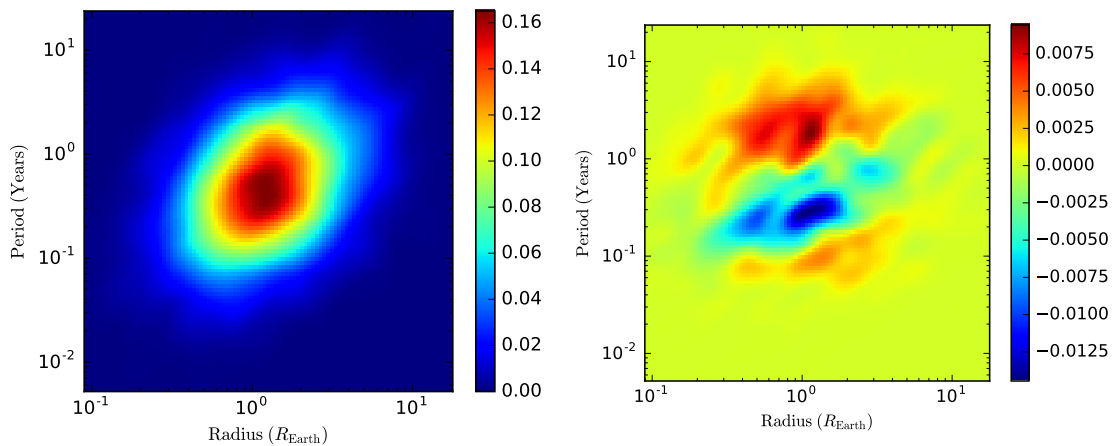


Figure 2.9: KDE plots of the initial (left) and difference between the final and initial (right) period-radius distribution.

eccentricity space and potentially creating close encounters. These close encounters could end up reordering the planets, and even lead to ejections of planets from the system. A plot of the mean and standard deviation of the inclination of the Kepler planets is shown in Figure 2.10. The planets begin in approximately the same orbital plane (which is slightly-inclined to the reference plane - recall Table 2.1), and in the case of stable systems remain in a disk-like structure, albeit slightly wider. A number of unstable systems end up with larger mean inclinations, although still remain fairly small on the scale of the critical angle for the LK mechanism or retrograde orbits. The standard deviation also grows in these unstable systems,

some of them reaching $i_{\text{SD}} \gtrsim 10^\circ$. For small planetary systems with a few bodies, this value of standard deviation still means that the planets are relatively aligned. However, the average inclination of planets in systems with large multiplicities can mask single bodies reaching significantly large inclinations. This can be checked by plotting the inclinations of each individual planet, and is shown in the left panel of Figure 2.11. The majority of planets end up in low inclination orbits, although several exceed the critical angle required for LK oscillations. There are also 5 planets which have reached a high enough orbit to be moving in a retrograde motion (relative to the other planets in the system), which is surprising considering that this set of integrations contains only Kepler planets which began in aligned orbits. Only three planets with inclinations above $\sim 20^\circ$ belong to stable systems. The right panel in the same figure shows the final eccentricities of the Kepler planets. The same trend is seen where planets belonging to stable systems are all found at low values, in this case only 2 exceeding $e \sim 0.2$. Tens of planets are able to reach moderate eccentricities, with several reaching $e \sim 0.8$. This high eccentricity likely means that these planets are orbit-crossing with other planets in their systems, and will likely be dynamically disrupted in the future potentially leading to ejections. The planets belonging to unstable systems with parameters close to their initial values are likely distant in semimajor axis to the planets which have changed order by semimajor axis in that system, so their orbits remain unperturbed.

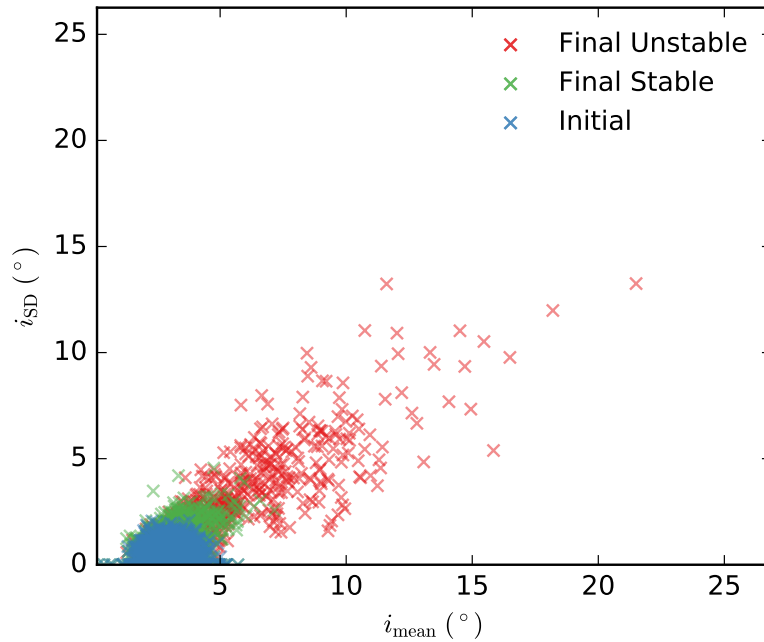


Figure 2.10: The mean and standard deviation of inclination of Kepler planets for each planetary system, including both the initial (blue) and final distributions, with the latter marked as stable or unstable by semimajor axis ordering. The planets are initially slightly-inclined to the reference plane (Table 2.1).

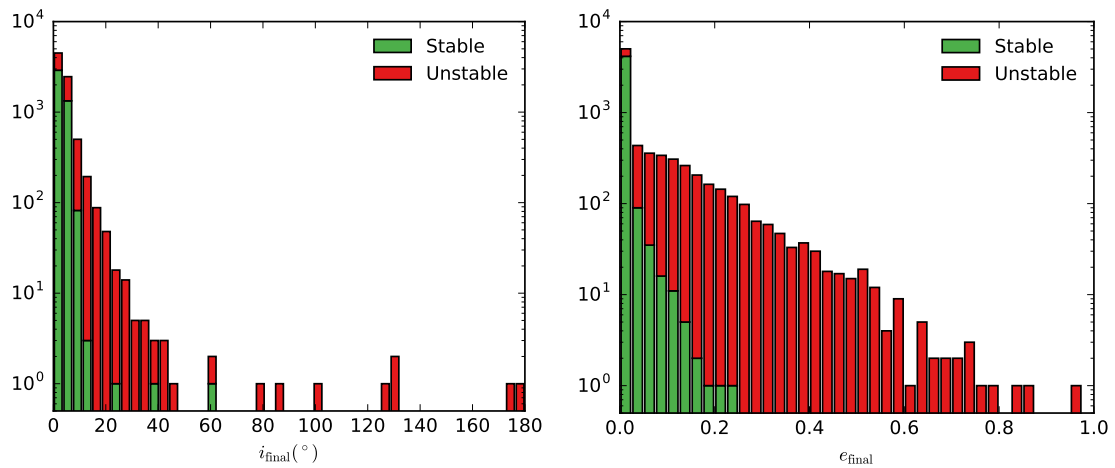


Figure 2.11: Histograms of the final inclinations (left) and final eccentricities (right) of Kepler planets, marked by belonging to stable or unstable systems. The inclination is measured with respect to the reference plane (see Table 2.1).

Integrating the Kepler planets with Jupiter-like perturbers

Integrations of the Kepler planets were performed again with the addition of Jupiter-like perturbers present (see section 2.4.3 for more details). The additional perturbers create stronger planet-planet interactions and increases the number of systems which become unstable, but only by 4.5% to 62.35%. Like in the case of just integrating the Kepler planets alone, Figure 2.12 shows that most of the systems that become unstable do so within the first $\sim 10^3$ orbits of the innermost planet. Past 10^2 orbits the surviving fraction is declining approximately linearly with $\log t$. It is also shown that there is a relationship between the length of time a system remains stable and the spacing of the closest two planets in that system, although there are a few systems where $d_{\text{CPP}} \gtrsim 8$ which are still able to become unstable in the order of ~ 100 orbits of the innermost planet. Note that the d_{CPP} here considers spacing between the Kepler planets and the Jupiter-like perturber as well as just between Kepler planet pairs. This means that the value of d_{CPP} for each system will be at most the same value as found in Figure 2.4, or smaller if there are Kepler planets orbiting closely to the Jupiter-like perturber. There is an increase in the number of systems with $d_{\text{CPP}} \gtrsim 10$ becoming unstable, even in just hundreds of orbits of the innermost planet.

Next we can compare the fate of the systems by planet spacing to the results with the integrations containing only Kepler planets. Despite the slightly larger number of unstable systems, the shape of the distribution of d_{CPP} for unstable systems shown in Figure 2.13 is the same as before – including the number of well-spaced systems going unstable. The distribution for stable systems, however, looks quite different. Instead of plateauing past $d_{\text{CPP}} \gtrsim 10$, the distribution appears more symmetrical. This is due to the perturber being in a relatively fixed position, which sets an upper limit on the planet spacing due to its higher mass. Additionally all of the previously excluded 1 Kepler planet systems are included, and are more likely to be stable

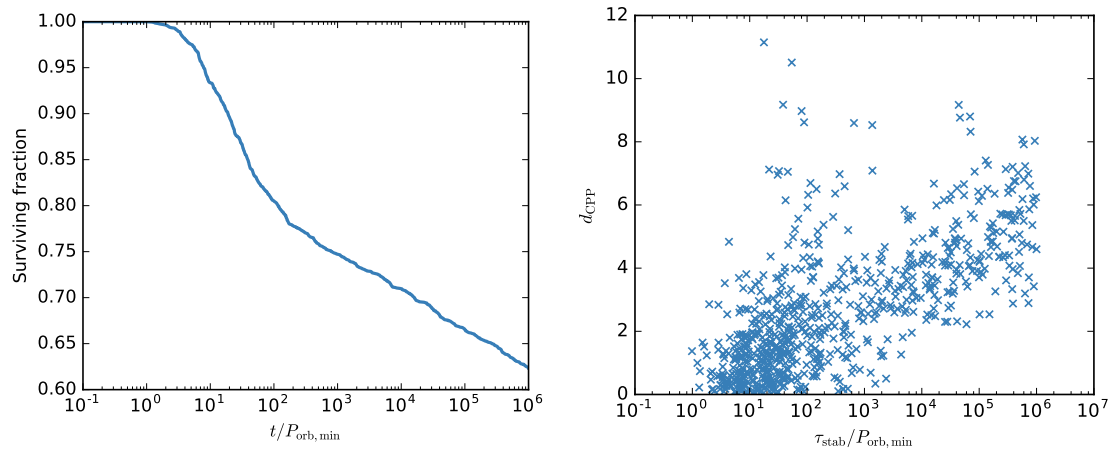


Figure 2.12: Surviving fraction of stable systems as a function of time (left) and the time systems remained stable versus d_{CPP} (right) for integrations with Jupiter-like perturbing bodies present.

due to a typically large planet spacing between the single Kepler planet and the perturbing body, meaning that eccentricity would need to be excited to large values before close encounters could occur. The boundary where the ratio of stable to unstable systems remains in the same location as before, where $d_{\text{CPP}} \sim 5$, which isn't too surprising because of the increase in number of unstable systems being small.

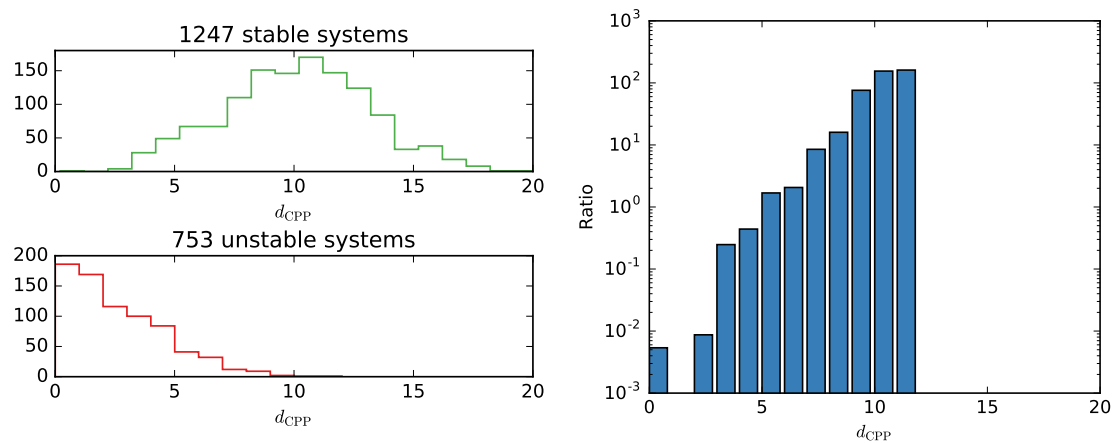


Figure 2.13: Histograms of planet spacings (by d_{CPP}) for both stable and unstable systems (left), and a histogram of the ratio of stable to unstable systems across planet spacing (right) when Jupiter-like perturbers are present. Spaces are present in the right panel where no stable or unstable systems fall within a bin.

There is no significant change to the ratio of stable to unstable systems by number

of Kepler planets present in the system, with only a slight increase across the board for systems with 2 or more Kepler planets (Figure 2.14). Systems with just one Kepler planet present all remain stable after integration, even with the Jupiter-like perturber present. So the effect of the perturber in these integrations is just swapping the order of two Kepler planets relatively close to each other after creating close encounters between them, rather than destabilising the system as a whole.

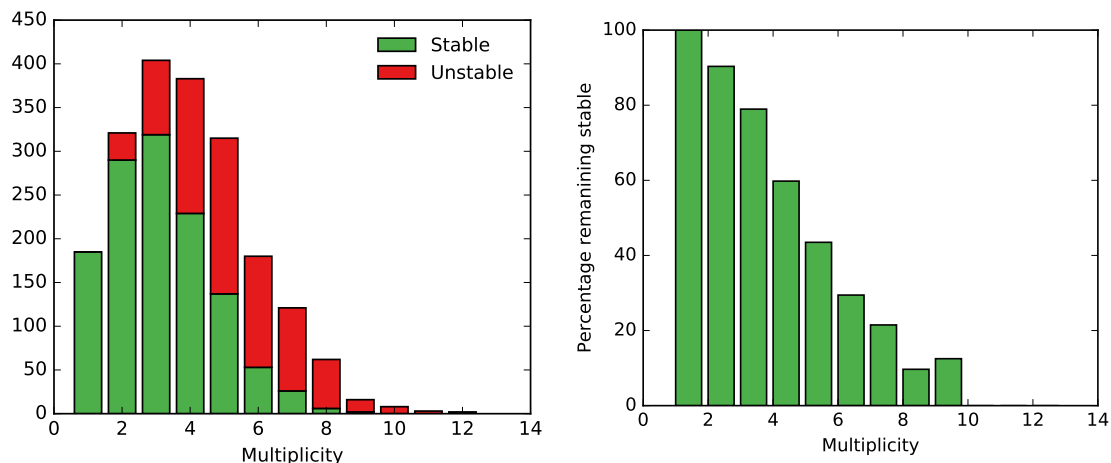


Figure 2.14: Frequency of multiplicity of Kepler planets in systems with aligned perturbers, marked by stability after one million inner orbital periods. Also shown in the right image is the percentage of systems remaining stable at each multiplicity. The Jupiter-like perturber is ignored in the count.

So far the results have indicated that the introduction of the Jupiter-like perturbers has only slightly affected the stability of these systems. We now look at their effect on the period-radius distribution of the Kepler planets. Figure 2.15 shows a scatter plot of the initial and final orbital period of each planet. The perturbing bodies are included to show the overlap between them and the distribution of Kepler planets, which fall just over 1 magnitude in orbital period from the peak of the distribution. Unlike in the integrations of the Kepler planets alone, there are a number of planets which are scattered to higher orbital periods, with several exceeding $\sim 10^4$ years. One such planet reaches a very large period of $\sim 3 \times 10^7$ years, or $\sim 3 \times 10^4$ AU. We can perform an order of magnitude calculation to find the limit in semimajor axis where the gravitational attraction of a neighbouring star approaches that of the

planet’s host star, based on the average separation distances between stars. If we consider our Milky Way to have a total stellar mass of $\sim 50 \times 10^9 M_{\odot}$ (McMillan 2017), then based on typical masses of stars this means there are $\sim 10^{11}$ stars in the galaxy. Approximating the stellar disk of the Milky way as a cylinder ~ 12 kpc in radius and ~ 0.3 kpc thick (Rix and Bovy 2013), then these stars are contained within a volume $\sim 5 \times 10^{11} \text{ pc}^3$, or roughly 1 star per $\sim 5 \text{ pc}^3$. The typical distance between stars is then ~ 2 pc or $\sim 3.6 \times 10^5$ AU. This distance corresponds to at minimum an order of magnitude larger than the orbital periods of the scattered planets, so these planets should remain gravitationally bound to their host star (although this result may be different for stars that are members of binaries). Looking at the overall distribution of Kepler planets using the KDE (Figure 2.16), the main depletion area is the same as before. Planets are migrating from this region to mainly wider orbits at approximately the same magnitude. The relatively small number of scattered planets can also be easily seen in this plot, which shows that the distribution is relatively stable even with the addition of these massive planets.

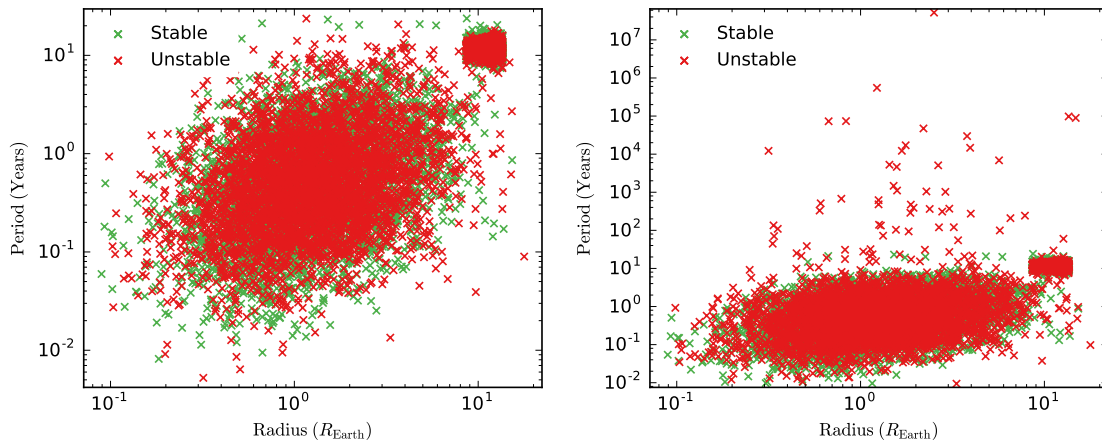


Figure 2.15: Scatter plots of the initial (left) and final (right) period and radius for each planet. The colour denotes whether that planet belongs to a system which is stable (green) or unstable (red). The massive Jupiter-like planets are included, seen to be covering a small area at large planetary radii.

The planetary disks in stable systems again appear to remain intact, with a small change in the mean and standard deviation of inclination for the Kepler planets in

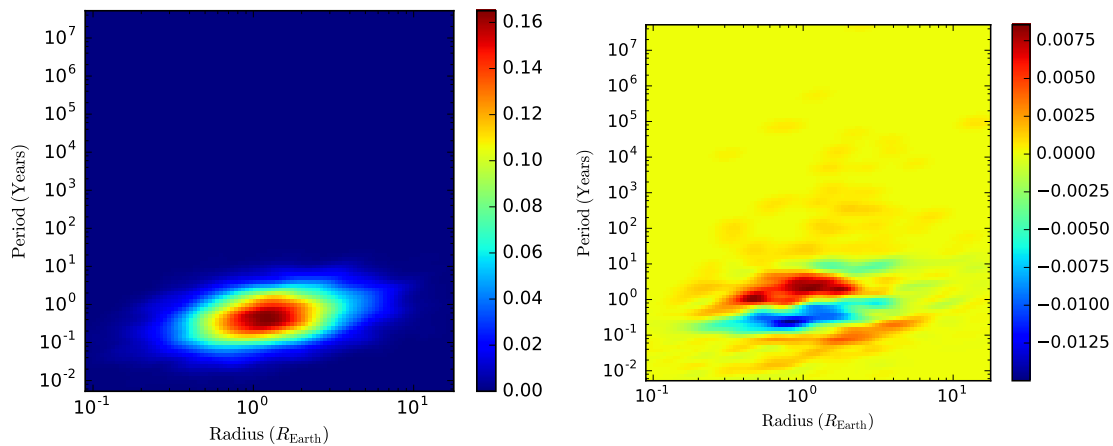


Figure 2.16: KDE plots of the initial (left) and difference between the final and initial (right) period-radius distribution from integrations with Jupiter-like perturbers added. Only Kepler planets are included in the calculation of the KDE.

each system (Figure 2.17). The picture for unstable systems is also mostly the same as for the Kepler-only integrations. Several of the unstable systems evolve to a very large mean inclination for the Kepler planets, surpassing 90° suggesting retrograde orbits are present. Their high standard deviations also suggest that the planetary disk has been disrupted, except for the lone system with $i_{\text{SD}} = 0.0^\circ$, meaning a lone Kepler planet in the system which is thrown into a retrograde orbit by interactions with the Jupiter-like perturber. If we look at the actual distribution of inclinations of each planet, as shown in the left panel of Figure 2.18, the distribution looks very similar to the integrations of just Kepler planets. This isn't unexpected because the Jupiter-like perturber is approximately in the same plane as the Kepler planets, so the planets only experience a weak secular torque in their angular momentum. However if we look at the right panel, many more Kepler planets mainly belonging to unstable systems have been excited to moderate-high eccentricities $e \gtrsim 0.5$. Perturbations from the massive planet have driven the eccentricity of tens of planets to eccentricities approaching 1. These planets will be orbit-crossing with every other planet in the system and will likely be ejected if the integration continued for longer.

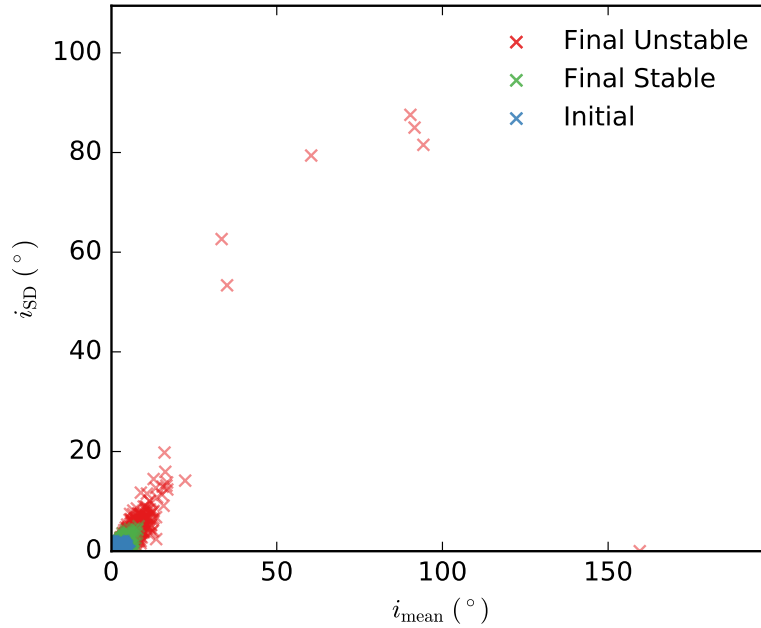


Figure 2.17: The mean and standard deviation of inclination (measured with respect to a reference plane, see Table 2.1) of Kepler planets for each planetary system, including both the initial (blue) and final distributions, with the latter marked as stable or unstable by semimajor axis ordering. This is from the integration run with Jupiter-like perturbers present. The planets are initially slightly-inclined to the reference plane (Table 2.1).

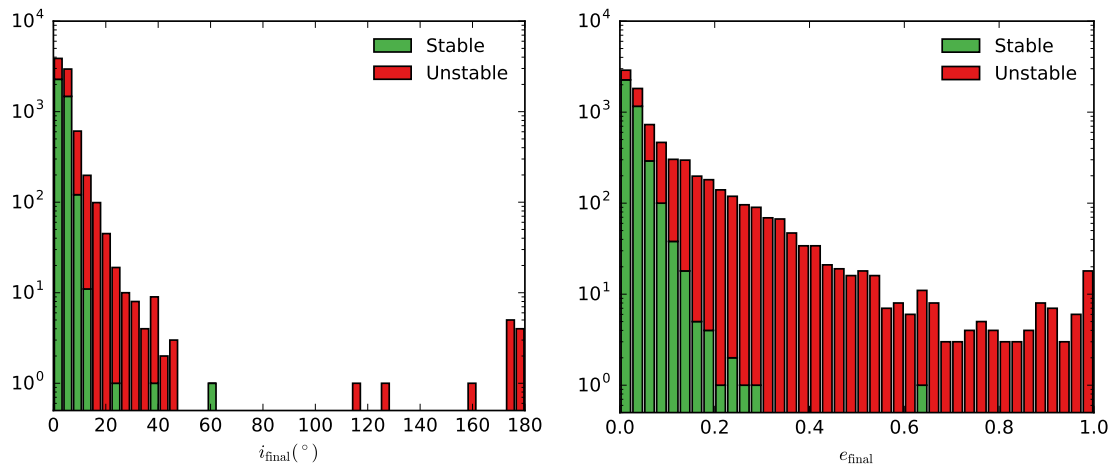


Figure 2.18: Histograms of the final inclinations (left) and final eccentricities (right) of Kepler planets integrated with Jupiter-like perturbers, marked by belonging to stable or unstable systems. The inclination is measured with respect to a reference plane (Table 2.1).

Numerical integrations of Kepler planets with a Jupiter-like perturber in an inclined orbit

Finally, we place the massive planet in an orbit moderately inclined $\sim 50^\circ$ relative to the orbital planes of the Kepler planets. The significant misalignment of the angular momentum vectors introduces additional evolutionary processes, such as LK oscillations. This time the majority of systems are now unstable, with 48.35% of systems stable after integration (Figure 2.19). The relationship between d_{CPP} and τ_{stab} is the same as in previous integrations, but the gradient appears steeper here. These inclined perturbers are able to destabilise systems with even larger spacings.

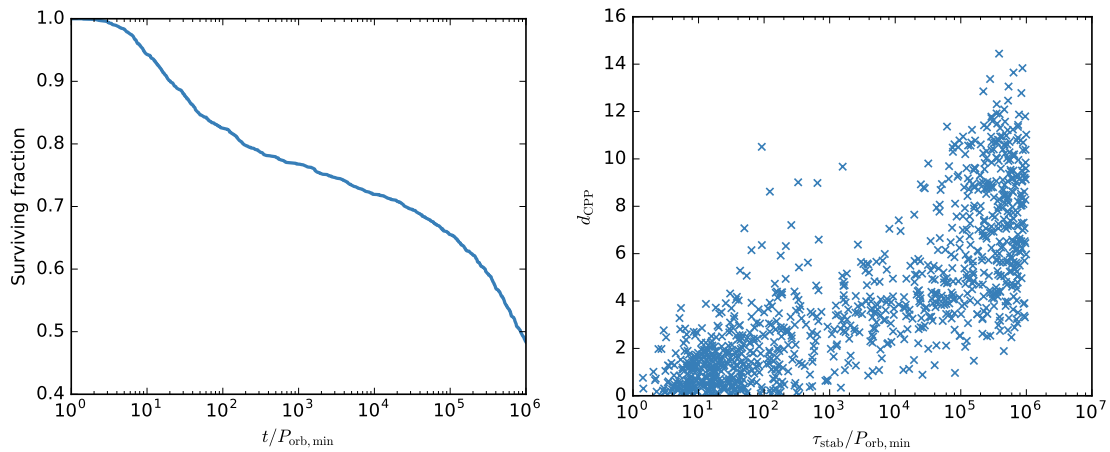


Figure 2.19: Surviving fraction of stable systems as a function of time (left) and the time systems remained stable versus d_{CPP} (right) for integrations with Jupiter-like planets in inclined orbits present.

This time unstable systems appear across an even larger range in d_{CPP} , with the tail falling off much more slowly, which can be seen in Figure 2.20. What’s interesting is the boundary between more stable systems versus more unstable systems d_{CPP} bin is still relatively unaffected, sitting slightly higher at ~ 6 , although now the ratio maintains a magnitude of ~ 1 until the spacing reaches $d_{\text{CPP}} \gtrsim 11$ – which is where a large number of additional unstable systems originate from.

The ratio of stable to unstable systems by multiplicity is, unsurprisingly, the lowest

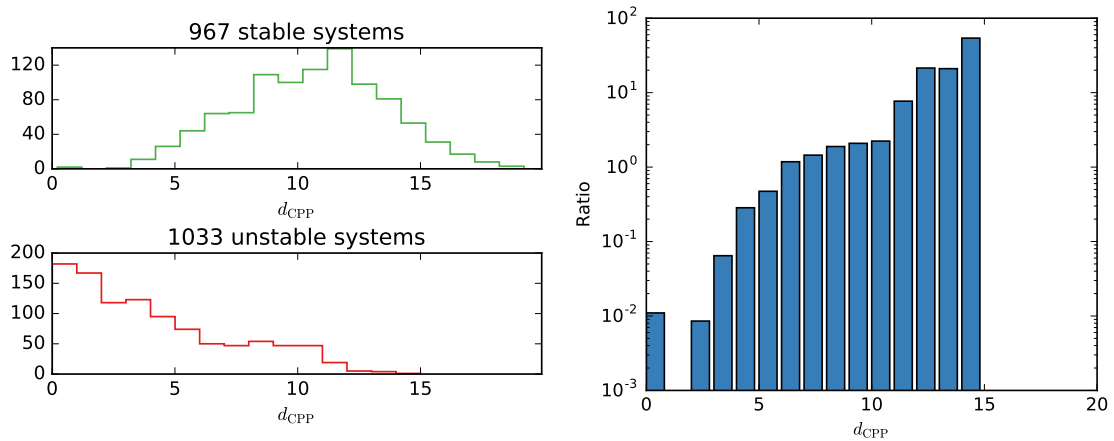


Figure 2.20: Histograms of planet spacings (by d_{CPP}) for both stable and unstable systems (left), and a histogram of the ratio of stable to unstable systems across planet spacing (right) when Jupiter-like perturbers in the moderately inclined configuration are present. Spaces are present in the right panel where no stable or unstable systems fall within a bin.

in this final set of integrations (Figure 2.21). Systems with 8 or more planets are very unlikely to maintain the same ordering of the planets, and even a small number systems with a single Kepler planet are driven to instability – potentially with the ejection of the planet as the orbit would have crossed that of the perturbing body.

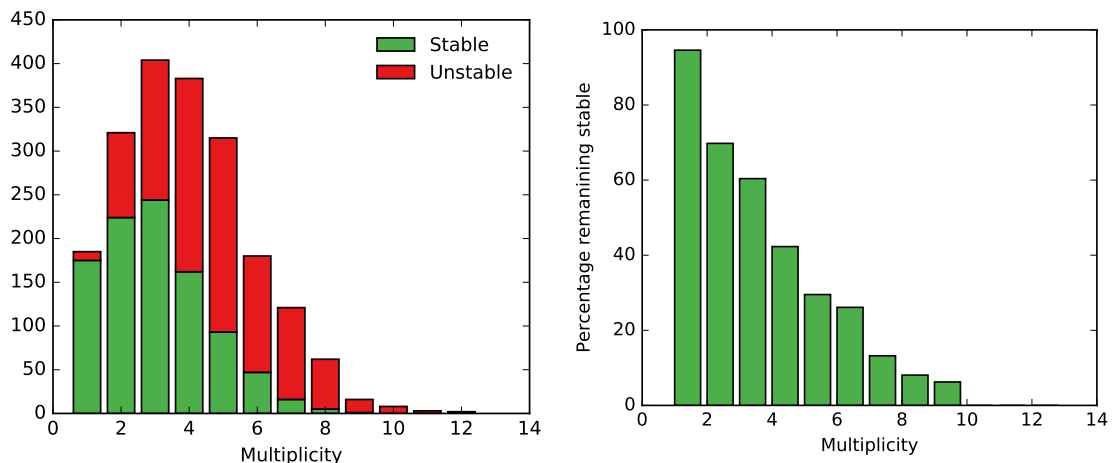


Figure 2.21: Frequency of multiplicity of Kepler planets in systems with inclined perturbers, marked by stability after one million inner orbital periods. Also shown in the right image is the percentage of systems remaining stable at each multiplicity. The Jupiter-like perturber is ignored in the count.

The number of planets scattered into high periodicity orbits is not considerably

different than with the perturbers in aligned orbits with the Kepler planets, as can be seen in figure 2.22. The change in the period-radius distribution is larger with changes in density of $\sim 10\text{-}20\%$ observed (2.23), the largest differences occurring around at the left and right edges, again following a trend of migrating to larger orbital periods. One may have expected a larger change given that over half of the planetary systems were measured unstable, and likely means that only a small number of planets shifted in semimajor axis in each system.

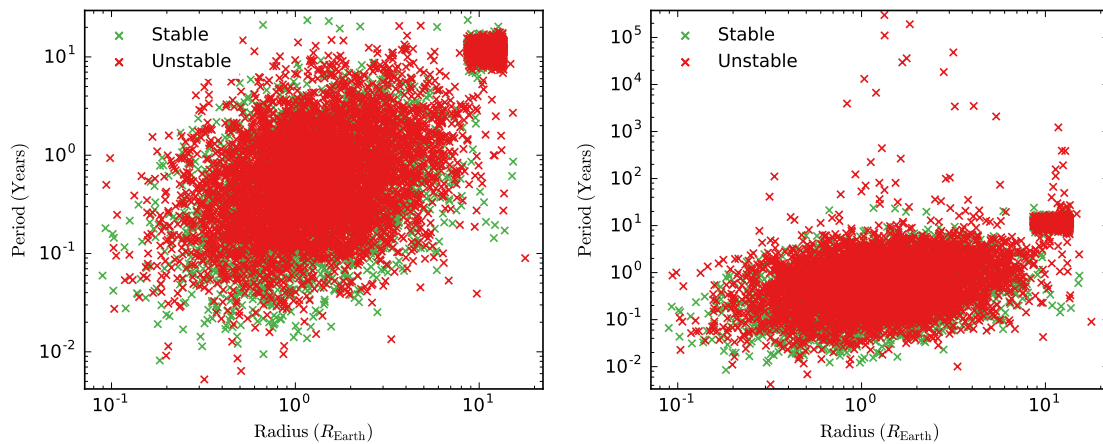


Figure 2.22: Scatter plots of the initial (left) and final (right) period and radius for each planet. The colour denotes whether that planet belongs to a system which is stable (green) or unstable (red). The massive perturbers are again shown.

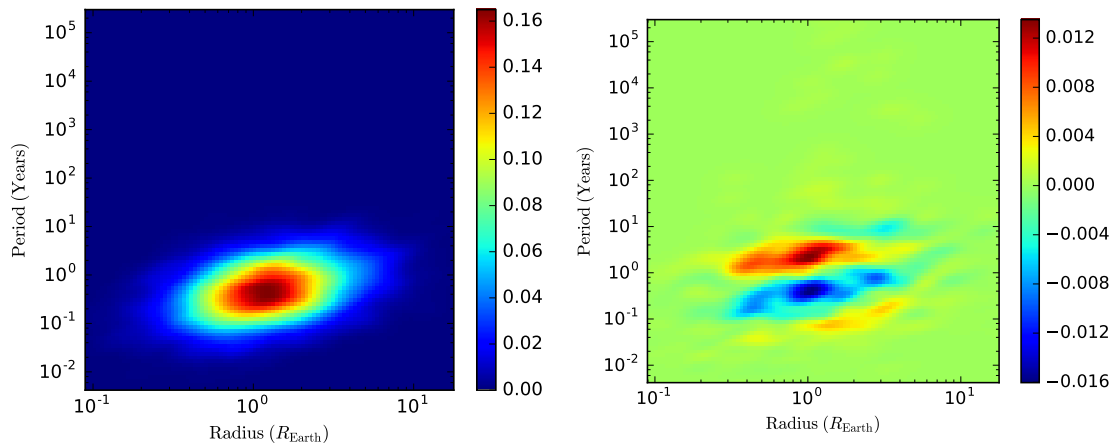


Figure 2.23: KDE plots of the initial (left) and difference between the final and initial (right) period-radius distribution. Only Kepler planets are included in the calculation of the KDE.

The distribution of the mean and standard deviations of inclination of Kepler plan-

ets is more interesting when the integrations are performed with inclined Jupiter-like planets added to the systems. Figure 2.24 shows a large spread in both the mean and standard deviation, particularly for unstable systems. Some stable systems reach fairly large standard deviations in inclination, but are typically concentrated at low values $i_{\text{SD}} \lesssim 5^\circ$. This is more clearly shown in Figure 2.25, with histograms of the standard deviation of the inclinations for each system. The thin planetary disk survives in over 50% of stable systems, and even a significant (~ 200) number of unstable systems maintain a standard deviation below $\sim 5^\circ$. The overall final distribution of inclinations of Kepler planets is shown in the left panel of Figure 2.26 appears almost uniform from $0 - 90^\circ$, with a sharp drop off for planets in retrograde orbits. The eccentricity distribution shown in the right panel is fairly surprising, it shows that there a large number of planets in stable systems reaching moderate ($\gtrsim 0.5$) eccentricities whilst still maintaining stability. It is likely that longer integrations will eventually lead to close interactions with other planets in the system for these planets, particularly if the Jupiter-like perturber continues to drive the eccentricities to increasingly larger values.

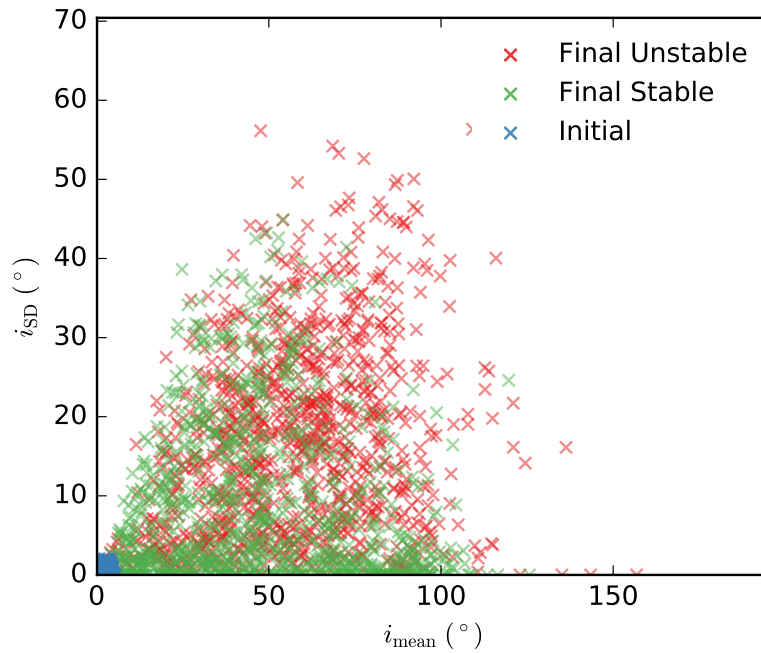


Figure 2.24: The mean and standard deviation of inclination of Kepler planets for each planetary system, including both the initial (blue) and final distributions, with the latter marked as stable or unstable by semimajor axis ordering. This is from the integration run with inclined Jupiter-like perturbers present. The planets are initially slightly-inclined to the reference plane (Table 2.1).

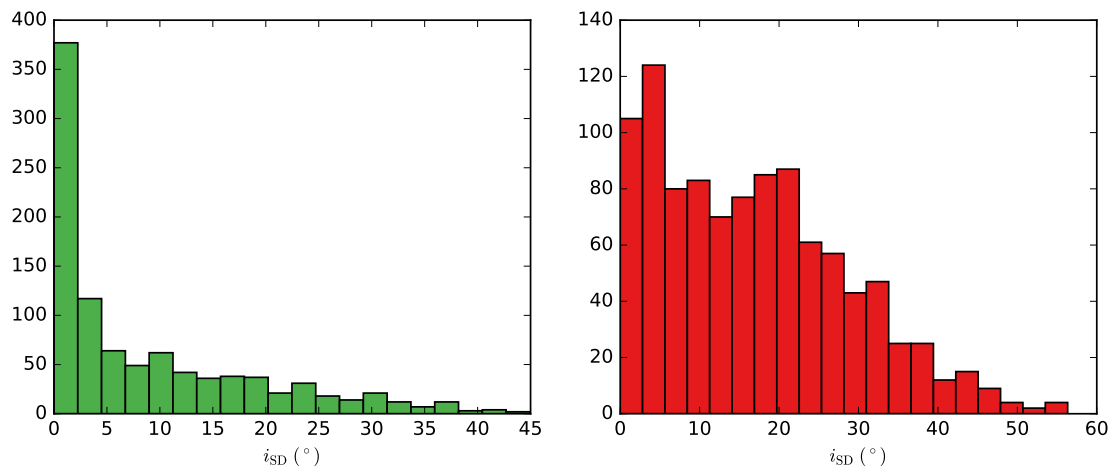


Figure 2.25: Histogram of the standard deviation of the final inclinations in each stable (left) and unstable (right) systems. Lower values indicates a more disk-like structuring of the planets.

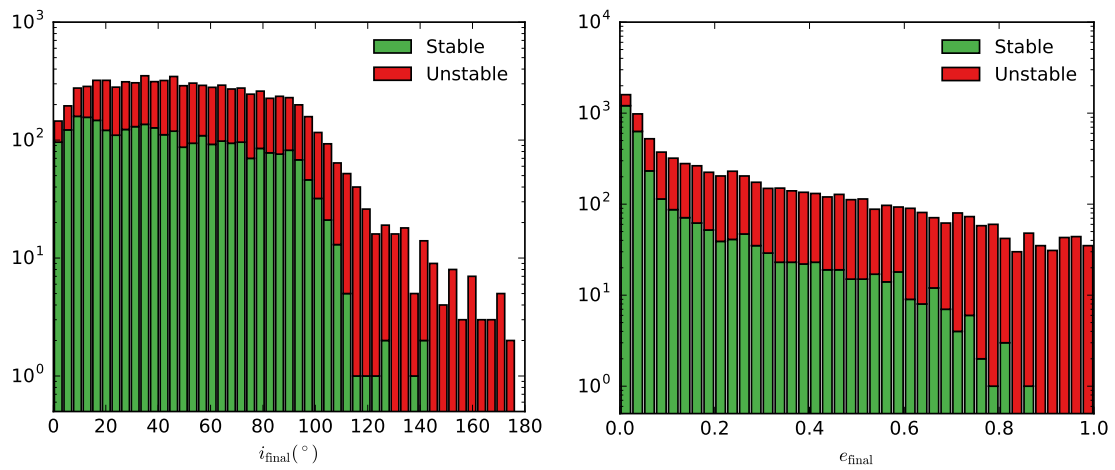


Figure 2.26: Histograms of the final inclinations (left) and final eccentricities (right) of Kepler planets integrated with Jupiter-like perturbers in inclined orbits, marked by belonging to stable or unstable systems.

2.5.2 Comparisons between the final distributions

This section looks at directly comparing the period-radius distributions obtained in each integration run. To begin with, the KLD is calculated for each combination of the initial distribution with each of the final distributions obtained in the three sets of integrations, representing the amount of information lost when one of the distributions is used to approximate another. To measure these values, we calculate the KDE at 10,000 points (100 in each dimension) uniformly in log-space over the same area containing the bulk of the period-radius distribution, contained within the range $10^{-5} - 5 \times 10^{-4}$ AU ($\sim 0.1 - 10 R_{\oplus}$) in planet radius and $0.01 - 100.0$ years in orbital period. The results are displayed in Table 2.3, where it can be seen that $D_{\text{KL}} \ll 1$ in each case. When approximating the initial distribution, over twice as much information is lost when using either final distribution with perturbers or inclined perturbers when compared to the final distribution of just the Kepler planets - with the final distribution with inclined perturbers as expected being the largest. A similar result is obtained in the reverse scenario, where the initial distribution can be used to approximate either of the final distributions. Here, the information lost when using the initial distribution to approximate the final distribution in period-radius with just Kepler planets is just under an order of magnitude smaller when compared to the other final distributions obtained with perturbing Jupiters present. Even with these variations, the overall differences remain small. This is reinforced when comparing the KDE of the final period-radius distribution between integrations of just Kepler planets and both sets with perturbing bodies. Figure 2.27 shows the differences in the KDE for both cases, showing small fluctuations in both cases (note the scale is comparable to the differences between the initial and final distributions, even the integrations of systems with only Kepler planets). There are similarities in some of the depleted areas of parameter space, such as the area around ~ 10 years and $\sim 10^{-4}$ AU. This area contains Kepler planets orbiting closely to the perturber,

so it isn't surprising to see a decrease of planets occupying this region.

P	Q			
	Initial	Final (KP)	Final (JLP)	Final (IJLP)
Initial	0.0	3.55×10^{-3}	7.92×10^{-3}	9.07×10^{-3}
Final (KP)	3.67×10^{-3}	0.0	5.53×10^{-3}	5.53×10^{-3}
Final (JLP)	2.56×10^{-2}	2.18×10^{-2}	0.0	3.06×10^{-3}
Final (IJLP)	2.42×10^{-2}	1.94×10^{-2}	2.92×10^{-3}	0.0

Table 2.3: KLD calculated for the initial and various final planet distributions in Period-Radius, including just Kepler planets (KP), with a Jupiter-like perturber (JLP) and inclined Jupiter-like perturber (IJLP), in base-2. The result in each case represents the amount of information lost when Q is used to describe P . Note that perturbers are not included in the calculation of the KDE, and hence don't affect the KLD directly.

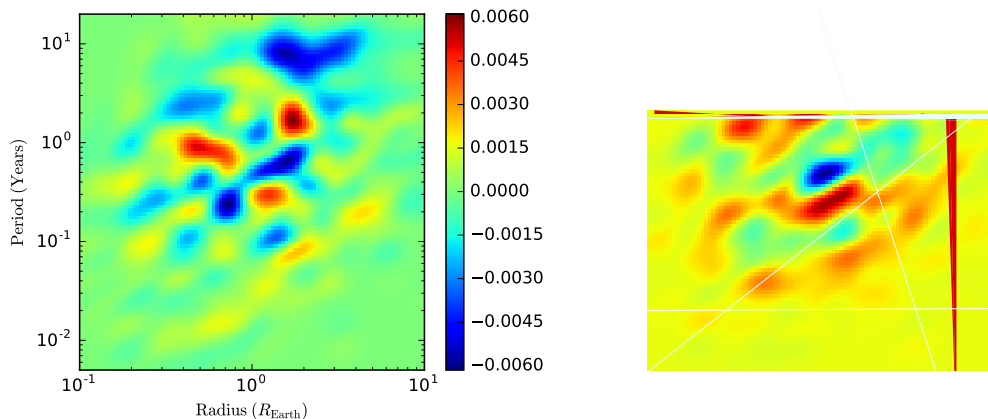


Figure 2.27: Difference in the KDE of final period-radius distributions of Kepler planets, comparing integrations with Jupiter-like perturbers (left) and inclined Jupiter-like perturbers (right) with just integrations of Kepler planets.

2.5.3 The instability of the planetary systems

Predicting instability

This section looks at predicting the time of instability for systems by semimajor axis ordering, based on the work in Chambers et al. (1996). Lines of best fit were calculated by obtaining parameters for Equations 2.28-2.29. There was no correlation found between the average spacing of planets in a given system and the length of time a system remained stable, as shown in the right panel of Figure 2.28, plotted for

planetary systems of four Kepler planets. The left panel shows a strong correlation when the minimum spacing is used instead, which is expected as this is essentially the same as the d_{CPP} versus τ_{stab} plots in the previous sections – the only difference is the units have been rescaled and we are focussing on systems with a fixed number of planets. The minimum spacing Δ_{min} is the smallest value for $\Delta_a/R_{\text{Hill,mut}}$ between any pair of planets in a system.

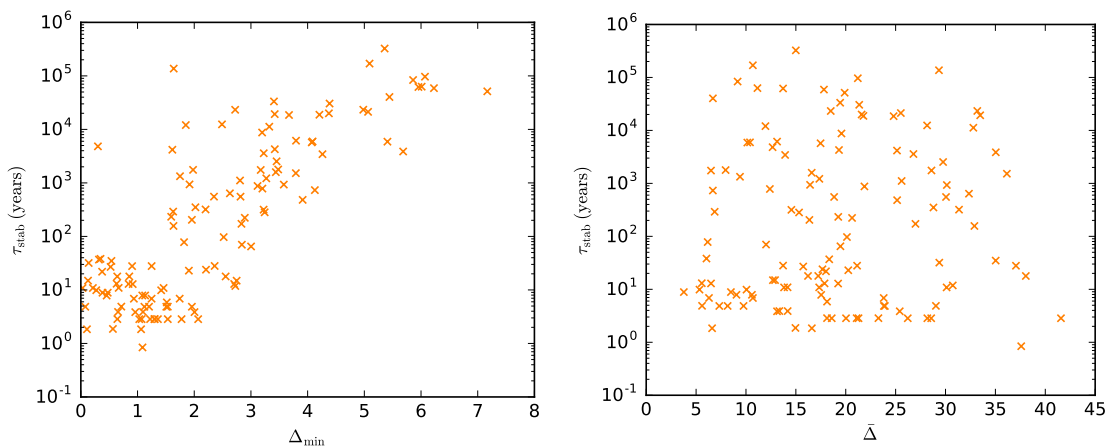


Figure 2.28: The stability timescale versus minimum spacing (left) or mean spacing (right) for each planetary system containing 4 Kepler planets (and no perturbing bodies), in units of mutual Hill radii.

An attempt has been made to reproduce figure two of Chambers et al. (1996) in Figure 2.29, shown for the same multiplicities (although missing $N = 20$ as there were no systems with this many planets). This is a plot of systems that contain only Kepler planets, and no perturbing bodies. Visually, the data for the three multiplicities seem similar to each other, although there are no ten-planet systems with $\Delta_{\text{min}} \gtrsim 2.5$. The lack of systems containing ten-planet systems that become unstable appears to have a large effect on the overall fit, as the gradient of the line looks significantly shallower than for the systems of fewer planets, and would predict that even well spaced systems where $\Delta_{\text{min}} \sim 8$ would become unstable within 1000 years if extrapolated. The lines of best fit look more reasonable for the other two multiplicities, suggesting that stability in excess of one million years can be achieved with well-spaced systems.

The parameters for the line of best fit for each multiplicity is shown in Table 2.4, along with values from Chambers et al. (ibid.) for the same multiplicity. The parameter b shows the strength of the dependence on the closest planet spacing for any given multiplicity, and it can be seen to become smaller at a decreasing rate over the range of two-eight planets. The parameters for nine and in particular ten planets are significantly different, and is potentially due to the small amount of data available for these multiplicities. Importantly, there are no systems containing nine or 10 planets which become unstable from $\sim 100 - 10^6$ years or with the Δ_{\min} between 3 – 8, whilst there are several systems at these multiplicities which are able to remain stable for one million inner orbital periods. The estimated errors on b is of order of the difference between the best-fit values across systems with four-eight planets, so that there is no significant change in the dependency on the smallest planet spacing in the system. This is a sign that the distance nearest neighbours are far more important than the number of planets overall, and is still consistent with the result that planetary systems with more planets in them are more likely to become unstable in one million inner orbital periods, as each Kepler planet is generated from a sample of the same distribution so the smallest spacing between planets in a system typically decreases when adding more bodies (which is the reason for a lack of high Δ_{\min} systems with $N \gtrsim 9$). When comparing the fitted parameter b to Chambers et al. (ibid.), we see that systems with four-eight planets are roughly in agreement, especially when comparing to using the arithmetic average of spacings in a system (the parameters are not shown here, but there was a lack of correlation after fitting parameters, which is expected from Figure 2.28). This likely means that the stability timescale for which planets reorder is a good approximation to the timescale of the first close encounter (to reorder would need orbit crossings, where close encounters become likely and frequent), and the closest spacing between any pair of planets is more important than the average neighbour distance.

The least-squares fits obtained for planetary systems with aligned Jupiters are sim-

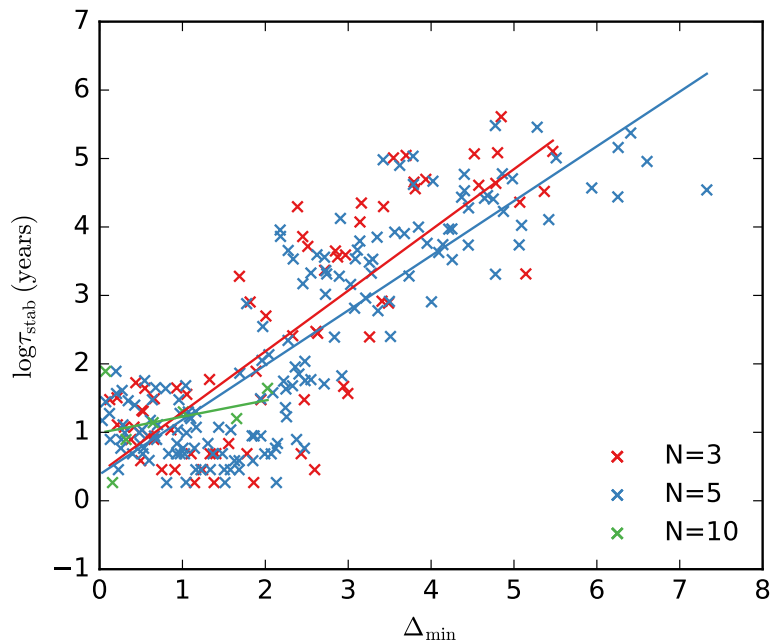


Figure 2.29: An attempt to reproduce figure 2 in Chambers et al. (1996), noting that the parameters on each axis are not exactly the same in each case. Only systems consisting of Kepler planets are shown here.

ilar to the Kepler only case, although in a couple of cases the fitting parameters become skewed by a small number of high $\Delta_{\min} \gtrsim 5$ systems which become unstable on very short timescales, an example of which is shown in Figure 2.30. Excluding these systems results in similar parameters as calculated in Table 2.4 for the remaining majority of systems (not shown here). The more interesting case is when we look at systems with Jupiter-like perturbers that are inclined relative to the Kepler planets. The relationship between stability time and the smallest planet spacing for a system appears to fit best to a piecewise function. This isn't all too surprising since looking back at Figure 2.19 we can see that, except for some outliers, shows the same trend with an increase in stability time until $d_{\text{CPP}} \sim 5$ before a wall is hit and a larger spacing doesn't appear to preserve the ordering of planets. Figure 2.31 shows a strong relationship between the minimum spacing and stability time for $\Delta_{\min} \lesssim 5$, with a similar expected stability time versus minimum spacing to Kepler planet-only systems with $\tau_{\text{stab}} \sim 10^4 - 10^5$ years at $\Delta_{\min} \sim 5$ for three and five planets. However, above this value the stability time doesn't increase with minimum

N	Fitted parameters		Chambers et al. (1996)	
	b	c	b	c
2	0.944 ± 0.098	0.156 ± 0.084		
3	0.888 ± 0.070	0.407 ± 0.042	1.176 ± 0.051	-1.663 ± 0.274
4	0.733 ± 0.043	0.538 ± 0.019		
5	0.799 ± 0.030	0.384 ± 0.013	0.765 ± 0.030	-0.030 ± 0.192
6	0.790 ± 0.033	0.482 ± 0.015		
7	0.728 ± 0.041	0.668 ± 0.022		
8	0.681 ± 0.063	0.396 ± 0.032		
9	0.820 ± 0.038	0.391 ± 0.026		
10	0.237 ± 0.157	0.991 ± 0.101	0.757 ± 0.038	-0.508 ± 0.244

Table 2.4: Parameters for the fit $\log \tau_{\text{stab}} = b\Delta_a/R_{\text{Hill}} + c$ for Kepler-only planetary systems that become unstable within one million inner orbital periods.

spacing past for $\Delta_{\text{min}} \gtrsim 5$. The parameters for the piecewise line of best fits for these two ranges are shown in Table 2.5 for up to ten planets (although there are no unstable ten-planet systems with $\Delta_{\text{min}} > 5$. The gradient of the lines of best fit for the small minimum spacings are comparable to the Kepler-planets only case. The gradient of the line of best fit for $\Delta_{\text{min}} > 5$ is very shallow for two-seven planets, and is consistent with $b \sim 0$ when considering the errors across the entire range (the small number of eight and nine planet systems results in a large uncertainty).

N	$\Delta_{\text{min}} \leq 5$		$\Delta_{\text{min}} > 5$	
	b	c	b	c
2	0.749 ± 0.131	2.06 ± 0.912	0.056 ± 0.028	4.988 ± 0.391
3	1.109 ± 0.160	-0.283 ± 0.154	-0.003 ± 0.005	5.174 ± 0.033
4	0.992 ± 0.094	0.179 ± 0.060	0.068 ± 0.021	4.012 ± 0.082
5	0.746 ± 0.094	0.361 ± 0.042	0.018 ± 0.008	4.686 ± 0.029
6	0.788 ± 0.071	0.247 ± 0.029	0.041 ± 0.075	4.064 ± 0.272
7	0.726 ± 0.094	0.289 ± 0.049	0.033 ± 0.041	4.541 ± 0.347
8	0.813 ± 0.084	0.261 ± 0.051	0.291 ± 0.530	1.672 ± 5.411
9	0.534 ± 0.098	0.353 ± 0.056	0.484 ± 0.747	0.290 ± 10.623
10	0.559 ± 0.136	0.416 ± 0.099		

Table 2.5: Parameters for the piecewise fit of $\log \tau_{\text{stab}} = b\Delta_a/R_{\text{Hill}} + c$ for systems with Kepler planets and inclined perturbers, showing a lack of correlation between spacing and stability time when $\Delta_{\text{min}} > 5$.

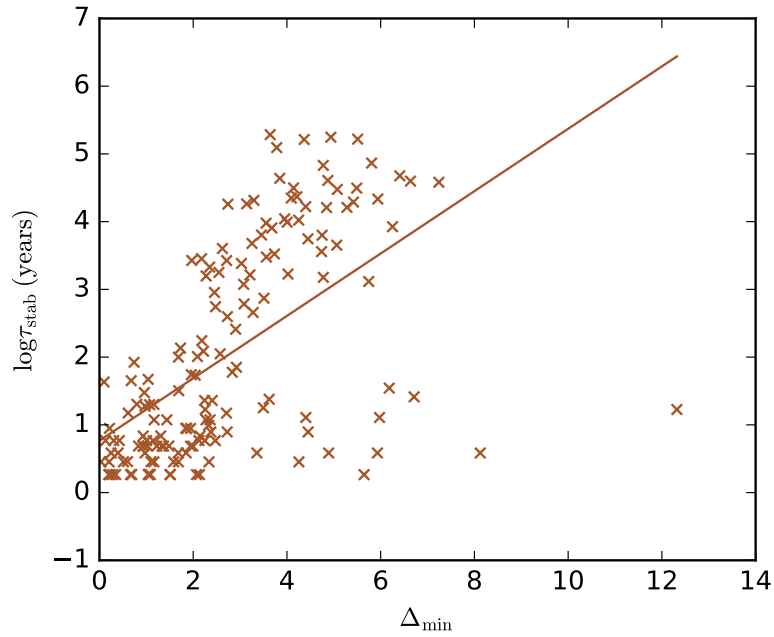


Figure 2.30: An example of the line of best fit being skewed by some high $\Delta_{\min} \gtrsim 5$ systems which become unstable on a short timescale, effectively reducing the gradient. This system contains five Kepler planets and 1 aligned Jupiter-like perturbing body which is included in the calculation of Δ_{\min} .

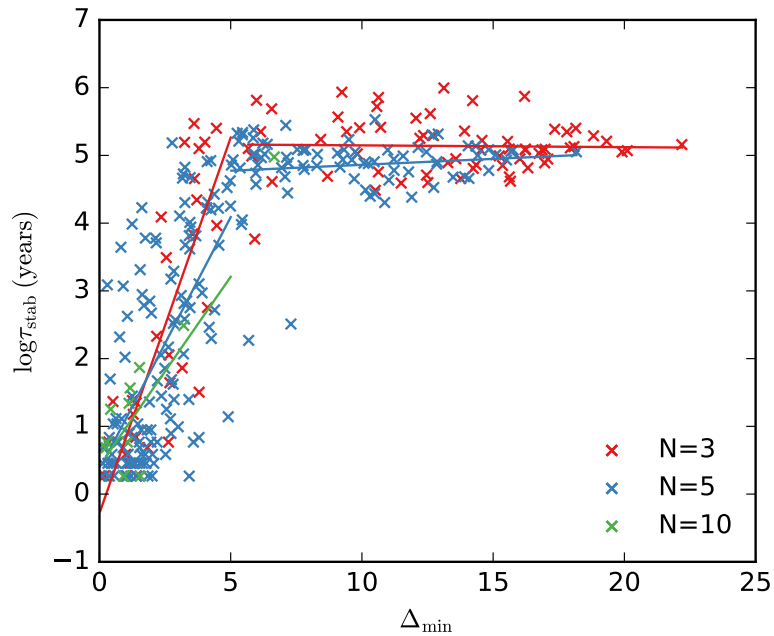


Figure 2.31: A plot of the stability time as a function of the closest planet spacing for planetary systems with inclined perturbers, shown for the same multiplicities as Figure 2.29 with a piecewise line of best fit (parameters can be found in Table 2.5).

So for Kepler planet-only systems the smallest spacing between any pair of planets in a system appears to be the strongest factor in determining when systems become unstable, although there is a reasonably large spread over $\sim 1-2$ magnitudes for any given value in Δ_{\min} , particularly for smaller values where the range can be greater. We also have to consider that not all systems become unstable within one million orbital periods, especially considering the majority of systems remain stable when they consist of just Kepler planets. Figure 2.32 shows the actual integration time for every stable system, and their minimum planet spacing. Only a handful of systems are integrated for longer than 10^6 years, and these are all either systems of just two planets or have a minimum spacing $\Delta_{\min} \gtrsim 5$, which predicts instability on the order of $\sim 10^5$ years for a system with three planets. It's unsurprising to see the systems surviving for the longest time are those with fewer planets, although this is partially affected by the increasing likelihood of creating systems with a shorter minimum orbital period from a higher number of random draws. In general, the systems which are spaced $\Delta_{\min} \lesssim 5$ have been integrated for $\sim 10^5$ years, with a small number of systems approaching $\sim 10^6$ years. However, as mentioned previously there is a spread over a reasonably large range in stability times. This shouldn't be surprising, as the minimum spacing is not the only factor which determines the stability of a planetary system – we already see the small effect of having additional number of planets by observing how the fitted parameter b changes with multiplicity. These other effects are very clearly seen in systems with inclined Jupiter-like perturbers, where the spacing appears to have no effect past 5 mutual Hill radii and instead another property of the systems are dominant. For Kepler planet-only systems, there is likely to be a difference in the time remains stable if you have $N > 2$ planets spaced equally apart with Δ_{\min} , than if you have two planets spaced with Δ_{\min} and the remaining spaced much further apart. In the first case, the planets that do not lie on the outside will be feel multiple perturbations at the same order of magnitude. In the latter case, the two planets may be isolated enough to be

able to ignore the other planets when considering their evolution – and this could greatly reduce the probability of close encounters that drive instability. Inclined Jupiters can cause the inner Kepler planets to undergo Lidov-Kozai oscillations. Recalling that the approximate timescale in the test particle limit is $\tau_{\text{LK}} \sim 8/15\pi(1 + m_{\text{star}}/m_{\text{out}})(P_{\text{out}}^2/P_{\text{in}})(1 - e_{\text{out}})^{3/2}$, the timescale for a Kepler planet orbiting in 0.1 years and a Jupiter-mass planet in a 10 year circular orbit is $\sim 170,000$ years (the timescale decreases for higher inner orbital periods, but is only valid for $a_{\text{out}} \gg a_{\text{in}}$). Inner planets can therefore undergo oscillations in the million inner orbital period simulations, and oscillations in eccentricity can create close encounters via orbit crossings.

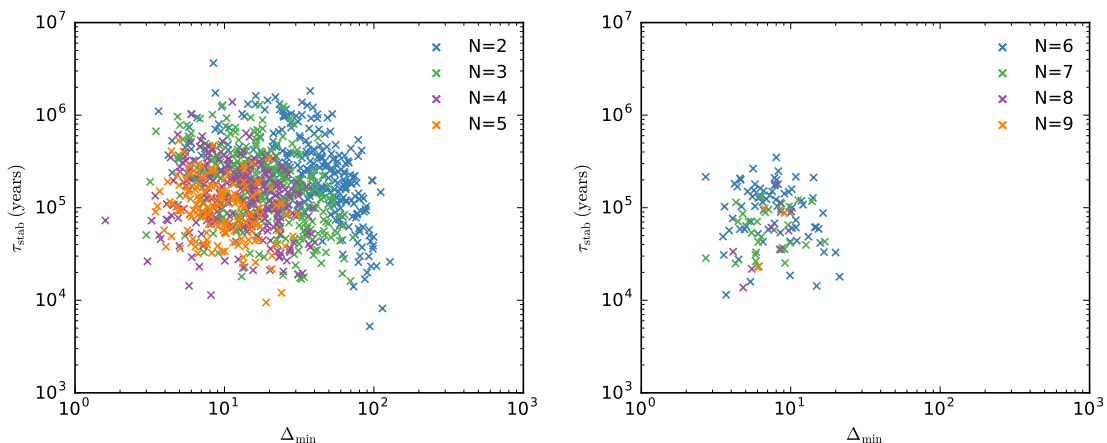


Figure 2.32: The integration time in units of years (instead of inner orbital periods) for stable Kepler planet-only systems that were integrated for one million inner orbital periods, categorised by multiplicity and split into two plots for clarity.

In fact, we can calculate the minimum eccentricity required for two orbits to begin crossing. Consider two Kepler planets being perturbed by an external Jupiter planet, with semimajor axis of a_1 for the inner planet and a_2 for the outer and are separated with spacing Δ_a . Focussing on the inner planet, it will begin to cross the orbit of the outer Kepler planet when its apoapsis is equal to the semimajor axis of the outer Kepler planet, $r_{\text{apo},1} \equiv a_1(1 + e_1) = a_2$. Rewriting in terms of the eccentricity, we

have:

$$e_1 = \frac{a_2 - a_1}{a_1}, \quad (2.44)$$

$$= \frac{\Delta R_{\text{Hill,mut}}}{a_1}, \quad (2.45)$$

$$(2.46)$$

where $\Delta = \Delta_a/R_{\text{Hill,mut}}$. For a given value of Δ , we can calculate the semimajor axis of the second body through rearrangement of the expression for Δ and substituting in the mutual Hill radius:

$$\Delta = 2 \left(\frac{a_2 - a_1}{a_1 + a_2} \right) \left[\frac{3M}{m_1 + m_2} \right]^{1/3}, \quad (2.47)$$

$$\gamma = \left(\frac{a_2 - a_1}{a_1 + a_2} \right), \quad (2.48)$$

$$a_2 = a_1 \left(\frac{1 + \gamma}{1 - \gamma} \right), \quad (2.49)$$

where M is the mass of the central body as before and $\gamma = \Delta((m_1 + m_2)/24M)^{1/3}$.

We can then substitute the expression for a_2 in Equation 2.49 into Equation 2.44, yielding:

$$e_1 = \frac{2\gamma}{1 - \gamma}. \quad (2.50)$$

The minimum eccentricity required for the inner planet is calculated for some example configurations in Table 2.6. For two relatively small planets from the Kepler distribution, the eccentricity required of just the inner planet for planet crossings to occur is small even for relatively large $\Delta \sim 10$ spacing between the planets. The eccentricity requirements are higher (by a factor of ~ 4) when the mass of the Kepler planets are towards the higher end of the distribution and the spacing reaches $\Delta > 10$, with an unbound orbit required for the largest spacings. However, this doesn't take into account of perturbations in eccentricity of the outer body. Setting the apoapsis of the inner body to the periapsis of the outer body and assuming per-

turbations on each planet are approximately equal resulting in similar eccentricity fluctuations (such as from a Jupiter-like perturber), then the minimum eccentricity required falls to $e = (a_2 - a_1)/(a_1 + a_2) = \gamma$ – approximately half of e_1 for small γ with an increasing difference as the planet spacing grows. Orbit crossings are therefore possible even for large $\Delta \gtrsim 10$ with reasonably small eccentricity perturbations, even without any secular changes in semimajor axis. The perturbations from the inclined Jupiter, potentially as LK oscillations, appear to be driving the eccentricities of the Kepler planets to large values (recall Figure 2.26 for final eccentricities of Kepler planets in these systems) and causing close encounters rather than through evolution of the semimajor axis (which is small as measured by changes in the orbital period distribution).

R_1 (AU)	R_2 (AU)	m_1	m_2	Δ	$e_{1,\min}$
				1.0	0.01
				3.0	0.03
10^{-5} ($0.23 R_{\oplus}$)	10^{-5} ($0.23 R_{\oplus}$)	$0.70 M_{\oplus}$	$0.70 M_{\oplus}$	5.0	0.05
				10.0	0.11
				20.0	0.24
				1.0	0.04
				3.0	0.11
10^{-4} ($2.35 R_{\oplus}$)	10^{-4} ($2.35 R_{\oplus}$)	$5.95 M_{\oplus}$	$5.95 M_{\oplus}$	5.0	0.19
				10.0	0.42
				20.0	1.06

Table 2.6: The minimum eccentricity required of the inner planet for orbit crossings between two Kepler planets, calculated for two small and two large Earth-like planets over a range of planet spacings.

Redefining stability

To this point, systems have been categorised as stable or unstable by the preservation of the order of Kepler planets by semimajor axis. However, there appears to be a disparity between the number of systems which go unstable and their impact on the period-radius distribution of the Kepler planets. It seems that whilst these planets

swap order in semimajor axis order, the distribution remains largely unaffected. We now look at redefining stability of systems where stable systems are those which the planets remain gravitationally bound to their host star. Table 2.7 contains the number of gravitationally unbound Kepler planets for each integration run, and the number of unique planetary systems they are found in. With this definition of stable, only a very small fraction of systems become unstable within one million inner orbital periods – even with the Jupiter-like perturbers added. It can be seen, on average, that each unstable system when defined in this sense contains multiple (about two-three) unbound Kepler planets.

Configuration	Unbound planets	Unstable systems
KP	15 (0.19%)	6 (0.30%)
JLP	68 (0.87%)	39 (1.95%)
IJLP	138 (1.76%)	57 (2.85%)

Table 2.7: Redefining stability: number of gravitationally unbound Kepler planets and the number of systems containing these unbound Kepler planets (ignoring the previous definition of stability by semimajor axis ordering) in each configuration (Kepler planets only, with Jupiter-like perturbers and with inclined Jupiter-like perturbers respectively).

Looking back at the final eccentricity distribution of Kepler planets in Figure 2.11, the number of gravitationally unbound planets will increase very slowly with longer integrations of just Kepler planets as the vast majority of planets are still on almost almost circular orbits. The number of ejected planets is expected to increase over longer integrations when the inclined Jupiter-like perturbers are added to the systems, as there are hundreds of planets with $e \gtrsim 0.8$. Figure 2.33 shows the highest eccentricity planet that is still bound to the host star after integration for each system for $e > 0.8$, for both configurations of the Jupiter-like perturber. Some of these systems already have a planet that has been ejected from the system, marked in red, but the majority of systems are still currently stable. The multiplicity of these systems, which can reach as high as twelve or thirteen planets, means that the high eccentricity planet(s) will experience encounters every $\lesssim 1000$ orbits. A single

close encounter may not result in an ejection, but it will become increasingly likely as the number of encounters increases and these systems will likely become unstable within $\lesssim 10^6$ years.

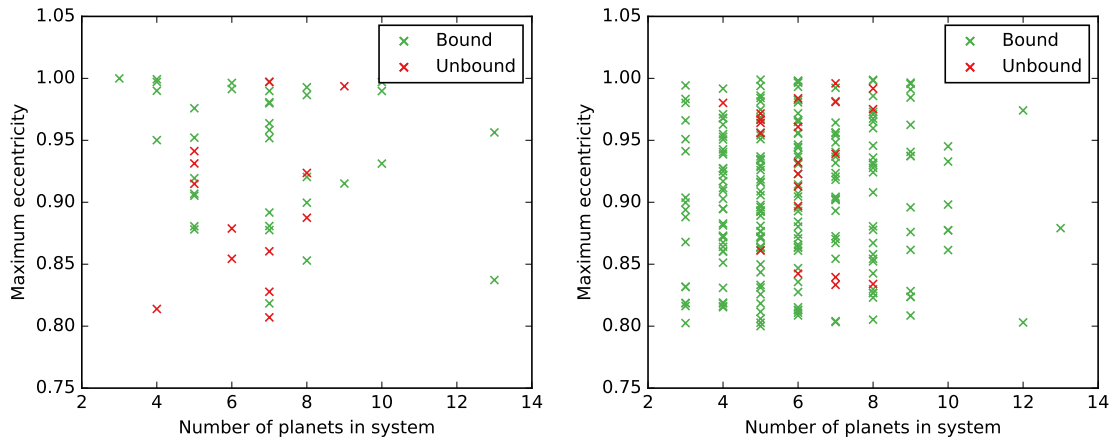


Figure 2.33: Maximum eccentricity (shown for $e > 0.8$) of bound planets after one million inner orbital periods against the number of Kepler planets in the system, denoted by whether any gravitationally unbound planets already exist. The left panel is for systems with a Jupiter-like perturber, and the right panel is when the Jupiter-like perturber is in the inclined configuration.

2.6 Conclusion

To summarise, period-radius distribution for Kepler planets is found to be stable when randomly generating each planet in a system independently of each other. Approximately two thirds of Kepler-only planet systems are dynamically stable when observing changes in the ordering by semimajor axis, with the fraction decreasing by just $\sim 5\%$ when a massive Jupiter-like planet is added. Adding a Jupiter-like planet in a highly-inclined orbit results in a small majority of systems becoming unstable by semimajor axis order, but still has little effect on the period-radius distribution as estimated using a KDE. However, when the giant planet has a large inclination relative to the inner planets the mean inclination of planets rises significantly. The standard deviation of the inclination also grows in this configuration, particularly for unstable systems.

Planets which experience close encounters are commonly found to swap positions in semimajor axis, and are mainly caused by excitations in eccentricity rather than changes in the semimajor axes of planets. Close encounters rarely result in the total ejection of a planet, with only fifteen planets across six systems ejected in Kepler-planet only systems and rising to one hundred and thirty-eight ($< 2\%$) planets in fifty-six systems when including inclined perturbers. All other planets remain bound to the host star, even when considering the typical sphere of influence of the host star over neighbouring companions.

Systems of planets which are closely spaced are less likely to remain stable over one million inner orbital periods, and a correlation was found between the length of time a system remained stable and the smallest spacing between any pair of planets as measured as Δ . The number of planets was also found to have an effect on the stability timescale when the minimum planet spacing is held constant. A line of best fit for each multiplicity was found for the stability timescale as a function of Δ_{\min} , and can predict when a system will become unstable by semimajor axis order to within 1 order of magnitude for most Kepler-planet only systems. The trends observed in the lines of best fit were the same as observed in Chambers et al. (1996), although the fitted parameters are slightly different which results in different expected stability timescales. Adding a Jupiter-sized perturbing body in the same plane as the Kepler planets increases the spread in stability timescales, with some outliers heavily affecting the fitted parameters, but the same trend was observed. This correlation between stability time and minimum planet spacing was also seen in systems with inclined Jupiter-sized perturbers, but the correlation disappeared for $\Delta_{\min} \gtrsim 5$, and the stability times of widely-spaced systems fell between $\sim 5 \times 10^4 - 10^6$ years. The spread in stability times indicates there were more factors determining the timescales other than just multiplicity and minimum planet spacing.

2.7 Discussion

So the majority of Kepler-planet only systems are stable, especially when looking at planet ejections. To get from the results of this project to the actual stability of real planetary systems, there are several things needed to be considered. For example, Jupiter-like bodies placed in the outer part of the system reduces the stability, but there is still uncertainty in the prevalence of these bodies in the outer regions of planetary systems. Only recently have such bodies started to be detected (Kipping et al. 2016) due to the length of observations required, with many more candidates which require follow-up observations (Wang et al. 2015; Osborn et al. 2016). These observations will help give a better idea of how frequent these outer-system planets are. In fact, it is estimate that at least 20% of compact Kepler systems of inner planets also contain at least one outer planet orbiting $\gtrsim 3$ AU (Uehara et al. 2016). This work has shown that single outer bodies can have a small effect on stability through eccentricity excitation in coplanar orbits, and larger effects when the mutual inclination is significant and can create LK oscillations. Eccentric outer bodies are expected to have an even larger impact on the stability of systems (A. J. Mustill et al. 2015). The presence of multiple giant planets spaced close to the boundary of stability in the outer system can create instabilities in the outer system itself (A. J. Mustill et al. 2016), whilst leaving the inner system unaffected in most cases.

As of today, there have been planets observed in 2,633 systems, with 586 of these systems containing multiple planets. Based on this work, it is possible that the majority of these systems have at least one outer perturber in an aligned configuration. This outer perturber rarely causes planet ejections, and does little to affect the period-radius distribution of planets – meaning that the effect of an aligned perturber is only potentially observably through eccentricity excitations, which is infrequently measured. Only recently have we started to observe outer bodies in planetary systems (Kipping et al. 2016), with many more candidates requiring follow-up observations

(Wang et al. 2015; Osborn et al. 2016). It is estimated that at least 20% of compact Kepler systems also contain at least one outer planet orbiting $\gtrsim 3$ AU (Uehara et al. 2016), which is consistent with the results of this work. The presence of such outer planets, particularly if giant, could mean that inner planets in observed multi-planet systems have experienced reordering by semimajor axis multiple times in their history.

The effect of an inclined outer giant planet on the inclination of the inner planets is more significant. The growth in the standard deviation of the inclination of inner planets by this outer body results in a very low probability to be able to observe multiple planets in these systems using the transit method, and thus we can conclude that the presence of outer bodies are very unlikely in any of the observed multi-planet systems. This inclined configuration also increases the eccentricity of planets on a relatively short timescale, and after a few Gyrs it is likely that the large eccentricities will have caused the majority of such systems to become unstable. Even a system with a single inner planet could be driven to a large enough eccentricity to become sun-grazing or start crossing orbits with this outer perturber, and as mentioned earlier in the chapter is one of the potential outcomes of Mercury due to interactions with Jupiter. Therefore if outer bodies are common in planetary systems, we expect them to be approximately aligned with any inner planets present.

As of the 19th October 2017, there are currently 3,532 confirmed planets (NASA 2017b). The parameters of planets in the multi-planet systems can be used to find lower limits on the planet spacings in these systems (due to some planets missing properties required to calculate the spacing, and potential for missing planets that are inclined relative to the others present in the system), which can be compared to the results from the numerical integrations. In total, the quantity d_{CPP} was calculated in 336 planetary systems observed by the Kepler telescope and is shown in Figure 2.34. Planets which did not have a direct measurement for their mass (and

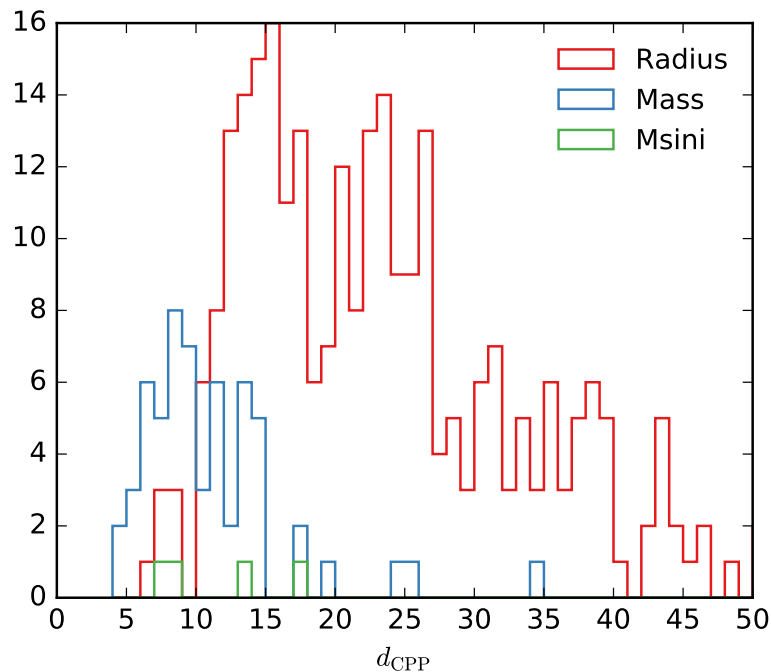


Figure 2.34: The minimum planet spacing measured as d_{CPP} for confirmed planets in Kepler systems, with the colours denoting the method for calculating the mass of the dominant planet in the closest planet-pair.

where possible for masses measured with a factor of inclination of the orbital plane relative to the observer), their mass was calculated using the mass-radius relationship from Weiss and Marcy (2014) with their radius. The peak of the distribution occurs at $d_{\text{CPP}} \sim 15$, and there is an extended tail where some systems are very widely-spaced. Therefore the majority of these systems are likely to be and remain stable. There are a small number of systems with a spacing of $d_{\text{CPP}} \sim 5$. Recalling the results of the numerical simulations without perturbers and with aligned perturbers (Figures 2.5 and 2.13), a small number of systems became unstable by semimajor axis ordering up to $d_{\text{CPP}} \lesssim 10$ – and this is on a timescale of just 1 million inner orbital periods. This means that the observed Kepler systems may have or may experience reordering of their planets. It is expected based on the numerical integrations that the probability of planet ejections in these systems is small.

Stellar binaries are not investigated in this work, although are about as common in the field as individual stars. A close-orbiting binary companion can be thought of as

a very massive outer body to a planetary system, and excite eccentricities through scattering and via LK oscillations similarly to a outer giant planet. In coplanar orbits they can excite the eccentricities in the outer system which can occasionally destabilise inner system planets (A. J Mustill et al. 2016).

The spacing of planets in this work range from very close $\Delta_{\min} \lesssim 3$ to very large $\Delta_{\min} > 20$, but don't necessarily accurately reflect that of real planetary systems (although it is unlikely that these systems are also uniformly spaced). The current observed distribution of spacings is distributed about a mean of $\bar{\Delta} \sim 12$ (Pu and Y. Wu 2015), and unsurprisingly find few systems with $\bar{\Delta} < 5$. The typical stellar age of a Kepler system is also comparable to the age of the Sun, on the order of \sim Gyr (Walkowicz and Basri 2013; McQuillan et al. 2014). The best-fit parameters for systems of up to 9 Kepler-planets from Table 2.4 predict a spacing of ~ 12 will be stable for at least a \sim Gyr timescale by semimajor axis order – which has been found to be an underestimate of stability time if measured by planet ejections. This result appears consistent with the Kepler spacing observations, and the reduction in stability from highly-inclined outer perturbers suggests that the typical planetary system likely doesn't contain a body in this configuration.

The amount of available computational resources restricted the length of time these integrations lasted. A small number of stable planetary systems by semimajor axis ordering were selected for longer \sim Gyr integrations, the results of which can be seen in section A.7. These integrations find that almost all well-spaced ($\Delta_{\min} > 10$) Kepler-only planet systems remain stable for timescales $\gtrsim 0.1$ Gyr, and could potentially survive as long as the age of the Solar System – particularly for systems with the largest minimum planet spacings. Again ejections are found to be rare with only a single planet ejected from one of the two unstable systems. From these integrations it is estimated that about $\gtrsim 38\%$ of all Kepler-planet only systems could remain stable for ~ 0.1 billion years without experiencing changes in the ordering

of planets by semimajor axis, and it is expected that the majority of systems will not experience planet ejections as eccentricity excitation is low. The instability timescale of these systems were predicted based on their planet spacing. One of the unstable systems lasted an order of magnitude longer than predicted, whilst the other became unstable by a factor of ~ 5 more quickly than expected. There were also several systems which appeared marginally-stable which had lasted longer than predicted, which indicates that just using the minimum planet spacing alone is not sufficient for accurately predicting stability timescales.

2.7.1 Limitations

The majority of integrations only lasted for one million inner orbital periods because of limited CPU time available, far shorter than the lifetime of a typical main sequence star or even the Solar System’s current age. This means the measuring stability for longer timescales is reliant on either extrapolating stability timescales based on minimum planet spacing, or applying the results from the small sample of long-term integrations to attempt to determine long-term stability for all systems. Even in these longer integrations, no system was observed to become unstable when the planet spacing satisfied $\delta_{\min} > 11$ – which are expected to go unstable on \gtrsim Gyr timescales. The low number of systems chosen for the long integrations also means that there is a reasonable large uncertainty in the true ratio of stable to unstable systems found at this timescale. Ideally, integrations would have been performed for $\gtrsim 1000$ systems for $\gtrsim 10^9$, the typical age of Kepler systems and on the order of the age of the Solar System. The host star was also the same for each system, modelled as the Sun. The Sun is slightly heavier than the average star, meaning that planet-planet interactions would be slightly stronger relative to the star for average stellar masses, although not by a significant amount. More massive stars would decrease the relative strength of gravitational interactions between planets, but their time on

the main-sequence can be short-lived. The central stars in each system were treated as point-masses, and only interact gravitationally with the planets and experiencing no evolution. Stellar evolution will likely become very important once a star reached the end of its main sequence, with planets close to the star likely to be encompassed as the surface of the star expands (Veras 2016).

Assumptions are also made on the structure of these planetary systems. The Kepler planets are placed in coplanar orbits (with small fluctuations) for the integrations in this work, so LK cycles don't occur – although these planets are generally closely spaced whereas this effect arises in hierarchical triple systems where $a_{\text{out}} \gg a_{\text{in}}$.

Collisions between planets and between a planet and the host star are ignored in simulations. However, planets that approach close enough for a collision to occur will also strongly gravitationally scatter and likely become unstable by semimajor axis order, and result in the ejection of one of the planets. The probability of a collision between planets is also smaller than just experiencing a close encounter within its Hill radius. A collision with the Sun would require an eccentricity of $e \gtrsim 0.99$ for a typical Kepler planet, which will mean they cross orbits of every other planet present in the system and become dynamically unstable by semimajor axis order even without these collisions. A number of these planets still remain bound to the host star after becoming unstable, and about $\lesssim 10$ planets end up colliding with the star with a Jupiter-like perturber in both the aligned and inclined configurations.

References

- [1] Chris Aldridge and Kirsty Stroud. “Modelling the Kepler Data Using Bayesian Inference”. In: *Year 4 Master’s Project Report* (2014).
- [2] J. M. O. Antognini. “Timescales of Kozai-Lidov oscillations at quadrupole and octupole order in the test particle limit”. In: *MNRAS* 452 (Oct. 2015), pp. 3610–3619. DOI: 10.1093/mnras/stv1552. arXiv: 1504.05957 [astro-ph.EP].
- [3] K. Batygin and G. Laughlin. “On the Dynamical Stability of the Solar System”. In: *ApJ* 683, 1207-1216 (Aug. 2008), pp. 1207–1216. DOI: 10.1086/589232. arXiv: 0804.1946.
- [4] J. E. Chambers, G. W. Wetherill, and A. P. Boss. “The Stability of Multi-Planet Systems”. In: *Icarus* 119 (Feb. 1996), pp. 261–268. DOI: 10.1006/icar.1996.0019.
- [5] R. Cloutier, D. Tamayo, and D. Valencia. “Could Jupiter or Saturn Have Ejected a Fifth Giant Planet?” In: *ApJ* 813, 8 (Nov. 2015), p. 8. DOI: 10.1088/0004-637X/813/1/8. arXiv: 1509.05397 [astro-ph.EP].
- [6] G. Colombo. “Rotational Period of the Planet Mercury”. In: *Nature* 208 (Nov. 1965), p. 575. DOI: 10.1038/208575a0.
- [7] M. J. Duncan and J. J. Lissauer. “Orbital Stability of the Uranian Satellite System”. In: *Icarus* 125 (Jan. 1997), pp. 1–12. DOI: 10.1006/icar.1996.5568.

-
- [8] M. J. Duncan and J. J. Lissauer. “The Effects of Post-Main-Sequence Solar Mass Loss on the Stability of Our Planetary System”. In: *Icarus* 134 (Aug. 1998), pp. 303–310. DOI: 10.1006/icar.1998.5962.
- [9] J. Fang and J.-L. Margot. “Architecture of Planetary Systems Based on Kepler Data: Number of Planets and Coplanarity”. In: *ApJ* 761, 92 (Dec. 2012), p. 92. DOI: 10.1088/0004-637X/761/2/92. arXiv: 1207.5250 [astro-ph.EP].
- [10] W. M. Farr et al. “The Occurrence of Earth-Like Planets Around Other Stars”. In: *ArXiv e-prints* (Dec. 2014). arXiv: 1412.4849 [astro-ph.EP].
- [11] B. Gladman. “Dynamics of systems of two close planets”. In: *Icarus* 106 (Nov. 1993), p. 247. DOI: 10.1006/icar.1993.1169.
- [12] D. Jontof-Hutter et al. “Outer Architecture of Kepler-11: Constraints from Coplanarity”. In: *ArXiv e-prints* (Mar. 2017). arXiv: 1703.08829 [astro-ph.EP].
- [13] S. R. Kane. “Stability of Earth-mass Planets in the Kepler-68 System”. In: *ApJ* 814, L9 (Nov. 2015), p. L9. DOI: 10.1088/2041-8205/814/1/L9. arXiv: 1511.02882 [astro-ph.EP].
- [14] D. M. Kipping et al. “A Transiting Jupiter Analog”. In: *ApJ* 820, 112 (Apr. 2016), p. 112. DOI: 10.3847/0004-637X/820/2/112. arXiv: 1603.00042 [astro-ph.EP].
- [15] Yoshihide Kozai. “Secular Perturbations of Asteroids with High Inclination and Eccentricity”. In: *AJ* 67.9 (Nov. 1962).
- [16] S. Kullback and R. A. Leibler. “On Information and Sufficiency”. In: *Ann. Math. Statist.* 22.1 (Mar. 1951), pp. 79–86. DOI: 10.1214/aoms/1177729694. URL: <http://dx.doi.org/10.1214/aoms/1177729694>.
- [17] J. Laskar. “A numerical experiment on the chaotic behaviour of the solar system”. In: *Nature* 338 (Mar. 1989), p. 237. DOI: 10.1038/338237a0.

- [18] J. Laskar. “The Chaotic Motion of the Solar System: A Numerical Estimate of the Size of the Chaotic Zones”. In: *Icarus* 88 (May 1990).
- [19] J. Laskar. “The limits of Earth orbital calculations for geological time-scale use”. In: *Philosophical Transactions of the Royal Society of London Series A* 357 (Aug. 1999), p. 1735. DOI: 10.1098/rsta.1999.0399.
- [20] J. Laskar and M. Gastineau. “Existence of collisional trajectories of Mercury, Mars and Venus with the Earth”. In: *Nature* 459 (June 2009), pp. 817–819. DOI: 10.1038/nature08096.
- [21] Jacques Laskar. “Chaotic Diffusion in the Solar System”. In: *Icarus* 196.1 (July 2008).
- [22] M. Lecar et al. “Chaos in the Solar System”. In: *ARA&A* 39 (2001), pp. 581–631.
- [23] M. L. Lidov. “The evolution of orbits of artificial satellites of planets under the action of gravitational perturbations of external bodies”. In: *Planet. Space Sci.* 9 (Oct. 1962), pp. 719–759. DOI: 10.1016/0032-0633(62)90129-0.
- [24] Y. Lithwick and S. Naoz. “The Eccentric Kozai Mechanism for a Test Particle”. In: *ApJ* 742, 94 (Dec. 2011), p. 94. DOI: 10.1088/0004-637X/742/2/94. arXiv: 1106.3329 [astro-ph.EP].
- [25] Yoram Lithwick and Yanqin Wu. “Theory of Secular Chaos and Mercury’s Orbit”. In: *ApJ* 739.1 (Sept. 2011).
- [26] R. Malhotra. “The Origin of Pluto’s Orbit: Implications for the Solar System Beyond Neptune”. In: *AJ* 110 (July 1995), p. 420. DOI: 10.1086/117532. eprint: astro-ph/9504036.
- [27] P. J. McMillan. “The mass distribution and gravitational potential of the Milky Way”. In: *MNRAS* 465 (Feb. 2017), pp. 76–94. DOI: 10.1093/mnras/stw2759. arXiv: 1608.00971.

-
- [28] A. McQuillan, T. Mazeh, and S. Aigrain. “Rotation Periods of 34,030 Kepler Main-sequence Stars: The Full Autocorrelation Sample”. In: *ApJS* 211, 24 (Apr. 2014), p. 24. DOI: 10.1088/0067-0049/211/2/24. arXiv: 1402.5694 [astro-ph.SR].
- [29] M. Moons and A. Morbidelli. “Secular resonances inside mean-motion commensurabilities: the 4/1, 3/1, 5/2 and 7/3 cases.” In: *Icarus* 114 (Mar. 1995), pp. 33–50. DOI: 10.1006/icar.1995.1041.
- [30] M. Moons, A. Morbidelli, and F. Migliorini. “Dynamical Structure of the 2/1 Commensurability with Jupiter and the Origin of the Resonant Asteroids”. In: *Icarus* 135 (Oct. 1998), pp. 458–468. DOI: 10.1006/icar.1998.5963.
- [31] S. J. Morrison and K. M. Kratter. “Orbital Stability of Multi-planet Systems: Behavior at High Masses”. In: *ApJ* 823, 118 (June 2016), p. 118. DOI: 10.3847/0004-637X/823/2/118. arXiv: 1604.01037 [astro-ph.EP].
- [32] C. D. Murray and S. F. Dermott. *Solar system dynamics*. 1999.
- [33] A. J. Mustill, M. B. Davies, and A. Johansen. “The Destruction of Inner Planetary Systems during High-eccentricity Migration of Gas Giants”. In: *ApJ* 808, 14 (July 2015), p. 14. DOI: 10.1088/0004-637X/808/1/14. arXiv: 1502.06971 [astro-ph.EP].
- [34] A. J. Mustill, M. B. Davies, and A. Johansen. “The effects of external planets on inner systems: multiplicities, inclinations, and pathways to eccentric warm Jupiters”. In: *ArXiv e-prints* (Sept. 2016). arXiv: 1609.08058 [astro-ph.EP].
- [35] Smadar Naoz et al. “Secular Dynamics in Hierarchical Three-Body Systems”. In: *MNRAS* 431.3 (May 2013).
- [36] NASA. *Kepler Discoveries*. NASA. Feb. 8, 2017. URL: <https://kepler.nasa.gov/Mission/discoveries/>.

- [37] NASA. *NASA exoplanet archive*. Oct. 19, 2017. URL: <https://exoplanetarchive.ipac.caltech.edu/index.html> (visited on 10/19/2017).
- [38] H. P. Osborn et al. “Single transit candidates from K2: detection and period estimation”. In: *MNRAS* 457 (Apr. 2016), pp. 2273–2286. DOI: 10.1093/mnras/stw137. arXiv: 1512.03722 [astro-ph.EP].
- [39] C. Petrovich. “The Stability and Fates of Hierarchical Two-planet Systems”. In: *ApJ* 808, 120 (Aug. 2015), p. 120. DOI: 10.1088/0004-637X/808/2/120. arXiv: 1506.05464 [astro-ph.EP].
- [40] G. H. Pettengill and R. B. Dyce. “A Radar Determination of the Rotation of the Planet Mercury”. In: *Nature* 206 (June 1965), p. 1240. DOI: 10.1038/2061240a0.
- [41] W. H. Press et al. *Numerical recipes in C++ : the art of scientific computing*. 2002.
- [42] B. Pu and Y. Wu. “Spacing of Kepler Planets: Sculpting by Dynamical Instability”. In: *ApJ* 807, 44 (July 2015), p. 44. DOI: 10.1088/0004-637X/807/1/44. arXiv: 1502.05449 [astro-ph.EP].
- [43] Hanno Rein and David S. Spiegel. “IAS15: A Fast, Adaptive, High-Order Integrator for Gravitational Dynamics, Accurate to Machine Precision over a Billion Orbits”. In: *MNRAS* 446 (2015), pp. 1424–1437.
- [44] H.-W. Rix and J. Bovy. “The Milky Way’s stellar disk. Mapping and modeling the Galactic disk”. In: *A&A Rev.* 21, 61 (May 2013), p. 61. DOI: 10.1007/s00159-013-0061-8. arXiv: 1301.3168 [astro-ph.GA].
- [45] K. R. Rybicki and C. Denis. “On the Final Destiny of the Earth and the Solar System”. In: *Icarus* 151 (May 2001), pp. 130–137. DOI: 10.1006/icar.2001.6591.

-
- [46] K.-P. Schröder and R. Connon Smith. “Distant future of the Sun and Earth revisited”. In: *MNRAS* 386 (May 2008), pp. 155–163. DOI: 10.1111/j.1365-2966.2008.13022.x. arXiv: 0801.4031.
- [47] David W. Scott. *Multivariate Density Estimation: Theory, Practice and Visualization*. John Wiley & Sons, Aug. 31, 1992.
- [48] A. W. Smith and J. J. Lissauer. “Orbital stability of systems of closely-spaced planets”. In: *Icarus* 201 (May 2009), pp. 381–394. DOI: 10.1016/j.icarus.2008.12.027.
- [49] G. J. Sussman and J. Wisdom. “Chaotic evolution of the solar system”. In: *Science* 257 (July 1992), pp. 56–62. DOI: 10.1126/science.257.5066.56.
- [50] Gerald J. Sussman and Jack Wisdom. “Numerical Evidence that the Motion of Pluto is Chaotic”. In: *Science* 241 (July 1988).
- [51] S. Uehara et al. “Transiting Planet Candidates Beyond the Snow Line Detected by Visual Inspection of 7557 Kepler Objects of Interest”. In: *ApJ* 822, 2 (May 2016), p. 2. DOI: 10.3847/0004-637X/822/1/2. arXiv: 1602.07848 [astro-ph.EP].
- [52] D. Veras. “Post-main-sequence planetary system evolution”. In: *Royal Society Open Science* 3, 150571 (Feb. 2016), p. 150571. DOI: 10.1098/rsos.150571. arXiv: 1601.05419 [astro-ph.EP].
- [53] L. M. Walkowicz and G. S. Basri. “Rotation periods, variability properties and ages for Kepler exoplanet candidate host stars”. In: *MNRAS* 436 (Dec. 2013), pp. 1883–1895. DOI: 10.1093/mnras/stt1700. arXiv: 1309.2159 [astro-ph.SR].
- [54] J. Wang et al. “Planet Hunters. VIII. Characterization of 41 Long-period Exoplanet Candidates from Kepler Archival Data”. In: *ApJ* 815, 127 (Dec.

- 2015), p. 127. DOI: 10.1088/0004-637X/815/2/127. arXiv: 1512.02559 [astro-ph.EP].
- [55] Lauren M. Weiss and Geoffrey W. Marcy. “The Mass-Radius Relation for 65 Exoplanets Smaller than 4 Earth Radii”. In: *ApJ* 783 L6.1 (Jan. 2014).
- [56] A. Wolszczan and D. A. Frail. “A planetary system around the millisecond pulsar PSR1257 + 12”. In: *Nature* 355 (Jan. 1992), pp. 145–147. DOI: 10.1038/355145a0.
- [57] J.-W. Xie et al. “Exoplanet orbital eccentricities derived from LAMOST-Kepler analysis”. In: *Proceedings of the National Academy of Science* 113 (Oct. 2016), pp. 11431–11435. DOI: 10.1073/pnas.1604692113. arXiv: 1609.08633 [astro-ph.EP].
- [58] J.-L. Zhou, D. N. C. Lin, and Y.-S. Sun. “Post-oligarchic Evolution of Protoplanetary Embryos and the Stability of Planetary Systems”. In: *ApJ* 666 (Sept. 2007), pp. 423–435. DOI: 10.1086/519918. arXiv: 0705.2164.

Chapter 3

Tidal disruptions of stellar binaries by a massive black hole

3.1 Preamble

This chapter presents the work published in Bradnick et al. (2017) titled “Stellar binaries in galactic nuclei: tidally stimulated mergers followed by tidal disruptions”, carried out by myself, Professor Ilya Mandel and Professor Yuri Levin. The source file was recompiled for the thesis to maintain consistent formatting, but is otherwise the same as originally submitted to Monthly Notices of the Royal Astronomical Society (MNRAS). Each of the following sections for this chapter are those from the published paper, including images. Complementary material is provided in the appendix. More specifically, section A.3 contains more detail on the outer orbits of the stellar binary around the massive black hole (MBH), section A.4 for the Runge-Kutta Cash-Karp method used for calculating the effects from stellar tides, section A.5 for the approximate tidal disruption radii of a single star and a binary by a MBH, and finally section A.6 for an order of magnitude calculation of the fluctuations in the orbital energy of the stellar binary by the MBH.

The work performed in this chapter considers the dynamical evolution of stellar binaries whose centre of mass is orbiting a MBH with very high eccentricity $\gtrsim 0.98$, where tidal perturbations caused by the MBH can drive the stars to merge. The systems were generated, integrated and their evolution plotted and analysed by myself. The initial draft of the paper was written by me, and the editing was shared between all authors. Many discussions took place between authors throughout the project, including on the approach to the problem and methods used for analysis.

3.2 Abstract

We investigate interactions of stellar binaries in galactic nuclear clusters with a MBH. We consider binaries on highly eccentric orbits around the MBH that change due to random gravitational interactions with other stars in the nuclear stellar clus-

ter. The pericentres of the orbits perform a random walk, and we consider cases where this random walk slowly brings the binary to the Hills tidal separation radius (the so-called empty loss-cone regime). However, we find that in a majority of cases the expected separation does not occur and instead the members of the binary merge together. This happens because the binary's eccentricity is excited by tidal interactions with the MBH, and the relative excursions of the internal eccentricity of the binary far exceed those in its internal semimajor axis. This frequently reduces the pericenter separation to values below typical stellar diameters, which induces a significant fraction of such binaries to merge ($\gtrsim 75\%$ in our set of numerical experiments). Stellar tides do not appreciably change the total rate of mergers but circularise binaries, leading to a significant fraction of low-eccentricity, low-impact-velocity mergers. Some of the stellar merger products will then be tidally disrupted by the MBH within $\sim 10^6$ years. If the merger strongly enhances the magnetic field of the merger product, this process could explain observations of prompt relativistic jet formation in some tidal disruption events.

3.3 Introduction

Dozens of tidal disruption event (TDE) candidates have been observed at a variety of wavelengths, including X-rays (Komossa and Greiner 1999; Komossa, Halpern, et al. 2004; Levan et al. 2011; Burrows et al. 2011), UV (Gezari, Heckman, et al. 2009; Bloom et al. 2011), optical (van Velzen et al. 2011; Gezari, Chornock, et al. 2012; Chornock et al. 2014; Holoien et al. 2014; Arcavi et al. 2014) and radio (Zauderer et al. 2011). The physics of tidal disruptions, including the theoretical investigation of TDE lightcurves, have been explored by Rees (1988), Phinney (1989), Magorrian and Tremaine (1999), Lodato et al. (2009), Strubbe and Quataert (2009), MacLeod et al. (2012), Guillochon and Ramirez-Ruiz (2013), Shen and Matzner (2014), Shiokawa et al. (2015), and Bonnerot, Rossi, et al. (2016) and others.

The majority of stars are members of stellar binaries. Binaries in a galactic nuclear cluster can scatter off other objects in the dense ($\gtrsim 10^6 \text{ pc}^{-3}$) stellar cluster (Spitzer and Hart 1971; Antonini, Faber, et al. 2010) surrounding the central MBH onto highly eccentric orbits around the MBH. Tidal interactions with the MBH can then separate the binary; in the classical picture, one component may be ejected as a hypervelocity star (Hills 1988; Yu and Tremaine 2003; Gualandris et al. 2005; Brown et al. 2005; Sari et al. 2010; Brown 2015), while the other may be subsequently tidally disrupted by the MBH.

Mandel and Levin (2015) investigated binaries which were scattered toward the MBH from large radii. A single scattering event could move such binaries onto nearly radial orbits around the MBH, fully populating the loss cone around the MBH (Lightman and Shapiro 1977). The component stars of such binaries may be tidally disrupted directly following the tidal separation of the binary, leading to double TDEs; Mandel and Levin (2015) estimated that 5 to 10 percent of all TDEs could be double TDEs. Only about 6% of the simulated binaries in the full loss cone were brought to merger by tidal interactions with the MBH.

We complete the earlier work of Mandel and Levin (*ibid.*) by considering binaries that are scattered toward the MBH from smaller radii. The reduced lever arm means that such binaries cannot immediately transition onto nearly radial orbits, i.e., into the loss cone for tidal separation, but may instead gradually and stochastically approach the tidal-separation loss cone through small angular momentum changes over many orbits. Binaries on orbits that pass within a few tidal separation radii from the MBH experience tidal perturbations. These perturbations can significantly change the angular momentum of the inner binary without significantly modifying its energy. The eccentricity of the inner binary can be driven close to unity, resulting in a binary merger. In contrast to the low fraction of tidally stimulated mergers of binaries in the full loss cone, we find that 80% of the empty loss cone binaries which

we simulate result in high-eccentricity mergers, with the remainder becoming tidally separated.

When stellar tides between the binary components are introduced following an equilibrium tide model (Hut 1981), the merging fraction drops slightly to 75%, with the remaining binaries being tidally separated. In the presence of stellar tides, about half of the binaries merge at high eccentricity as before, but the other half merge with low eccentricities ($e \lesssim 0.2$) due to efficient tidal circularization of the binary's inner orbit. As a result of stellar tides, these binaries merge at lower semimajor axes.

Mergers of binaries on less eccentric orbits around the MBH as a result of Lidov-Kozai (LK) resonances (Lidov 1962; Kozai 1962) and stellar evolution have been previously considered by Antonini, Faber, et al. (2010), Prodan et al. (2015), and Stephan et al. (2016). In particular, Antonini, Faber, et al. (2010) also investigated stellar binaries around an MBH with lower eccentricities than in this study, concluding that LK oscillations played a dominant role in producing stellar mergers. However, as we show here, LK resonance is suppressed for binaries on highly eccentric orbits around the MBH because scattering relaxation interactions with the surrounding stellar cusp change the angular momentum of the binary's centre of mass around the MBH on a timescale that is shorter than the LK timescale. Moreover, merger products from lower-eccentricity orbits are less likely to tidally interact with the MBH shortly after merger.

On the other hand, the merger products arising from binaries on very eccentric orbits around the MBH can be tidally disrupted by the MBH on timescales of a million years or less. As well as being more massive and appearing rejuvenated, the merger products can have their magnetic fields strongly enhanced as a result of the merger (Wickramasinghe et al. 2014; Zhu et al. 2015) [however, Guillochon and McCourt (2017) and Bonnerot, Price, et al. (2016) criticized the Zhu et al. (2015)

result, arguing that it did not incorporate a satisfactory magnetic field divergence cleaning scheme]. Prompt jets have been observed in the Swift J164449.3+573451 TDE (Bloom et al. 2011; Burrows et al. 2011; Levan et al. 2011; Zauderer et al. 2011). Initial large-scale magnetic fields can aid in prompt jet production (Tchekhovskoy et al. 2014a), but may not be required (Parfrey et al. 2015). Tidal disruptions of the products of recent tidally stimulated mergers with amplified magnetic fields may be potential candidates for prompt jet formation.

The structure of this paper is as follows. In section 3.4 we provide details of our binary population model, integration methods, the evolution of the angular momentum of the orbit around the MBH and the stellar tides model. We present our results in section 3.5. We discuss the implications of the results and the limitations of this work in section 3.6.

3.4 Methods

We numerically integrate the trajectories of 1000 individual stellar binaries on highly eccentric orbits around an MBH, following an approach similar to Gould and Quillen (2003). We model the very eccentric orbit around the MBH as a parabolic orbit and numerically integrate only the near-periapsis portion of the orbit, over ~ 20 inner orbital periods, where tidal effects from the MBH on the inner binary are greatest. We make use of the *IAS15* integrator in the *REBOUND* software package (Rein and Liu 2012; Rein and Spiegel 2015) (see acknowledgements for more details).

In between the integrated periapsis passages, the orbit around the MBH evolves due to two-body relaxation. Each system is evolved until the stellar binary is either tidally separated or undergoes a merger, defined as the stars approaching to a separation smaller than the sum of their radii.

We evaluate the impact of stellar tides by integrating the same set of 1000 simu-

lations with a simple prescription for equilibrium tides adapted from Eggleton and Kiseleva-Eggleton (2001). The following subsections contain details of the population model.

3.4.1 Binary population

We use the same approach as Mandel and Levin (2015) to generate the stellar binary properties. The mass M_1 of the primary star is generated from the Kroupa initial mass function (Kroupa 2001), in the range $M_1 \in [0.1, 100] M_\odot$. The mass of the secondary is drawn according to the mass ratio $q = M_2/M_1$ distribution $p(q) \propto q^{-3/4}$, $q \in [0.2, 1.0]$, consistent with observations (Duquennoy and Mayor 1991; Reggiani and Meyer 2011; Sana et al. 2013). The radius of each main-sequence star is set using the approximate relationship $R_* = (M_*/M_\odot)^k R_\odot$ (Kippenhahn and Weigert 1994), with $k = 0.8$ for $M_* < M_\odot$ and $k = 0.6$ when $M_* \geq M_\odot$.

The semimajor axis a of the stellar binary is randomly drawn from $p(a) \propto 1/a$ (Öpik 1924) with an upper limit of 1 AU and a lower limit set by the requirement that both stars must initially fit within their Roche lobes at periapsis (Eggleton 1983). The binary is further constrained to lie in the range of orbital periods $P_{\text{bin}} \in [0.1 \text{ days}, 1 \text{ year}]$. The upper limits in these constraints ensure that the binary is sufficiently compact to avoid disruption through interactions with other stars in the nuclear cluster.

The initial eccentricity distribution is based on Duquennoy and Mayor (1991), and is determined from the inner orbital period. Binaries with short periods (under 10 days) are placed on circular orbits and the remaining binaries have their eccentricities e drawn from a Gaussian with mean $\mu = 0.3$ and standard deviation $\sigma = 0.15$. The orbital plane of the inner (binary) orbit is randomly orientated with respect to the outer orbital plane (around the MBH), with the mutual inclination drawn uniformly in $\cos i \in [-1, 1]$ and the argument of periapsis and longitude of ascending node

uniformly drawn from $\omega, \Omega \in [0, 2\pi]$.

3.4.2 Outer orbit around the MBH

We consider binaries which have been scattered onto high eccentricity orbits around the MBH of mass $M_{\text{MBH}} = 10^6 M_{\odot}$. The angular momentum of the binary's orbit around the MBH will wander due to interactions with stars in the Bahcall-Wolf cusp. This cusp, with number density $n(r) \propto r^{-7/4}$, contains $N \sim 10^6$ stars in the MBH sphere of influence extending out to $\sim 1\text{pc}$ (Merritt 2004).

Mandel and Levin (2015) explored binaries in the full loss cone for which the typical change $\langle dh \rangle$ in angular momentum during one orbit around the MBH was larger than the minimum angular momentum for tidal disruption by the MBH (Lightman and Shapiro 1977):

$$h_{\text{LC}} \sim \sqrt{GM_{\text{MBH}}a \left(\frac{M_{\text{MBH}}}{M_{\text{bin}}} \right)^{1/3}}. \quad (3.1)$$

In this work, we instead focus on binaries which live in the empty loss cone and slowly explore the angular momentum space. This allows the MBH to gradually tidally perturb the inner orbit over many orbital passages near the MBH. The typical fractional evolution of the angular momentum per orbit for our population of binaries is $\langle dh \rangle / h_{\text{LC}} \sim 0.1$.

The timescale for two-body relaxation to change the angular momentum by that of a circular orbit ($h_{\text{circ}} = \sqrt{GM_{\text{MBH}}r}$) is given by Spitzer and Hart (1971):

$$\tau_{\text{relax}} = \frac{v^3}{15.4G^2nm_*^2 \log \Lambda}, \quad (3.2)$$

where $m_* \sim 0.5 M_{\odot}$ is the typical stellar mass, n is the local stellar density, $v \sim \sqrt{GM_{\text{MBH}}/r}$ is the typical stellar velocity at distance r from the MBH and $\Lambda \sim 0.4N$ is the Coulomb logarithm. The typical change in the angular momentum during one

orbit is given by

$$\langle dh \rangle = h_{\text{circ}} \left[\frac{P_{\text{out}}}{\tau_{\text{relax}}} \right]^{1/2}, \quad (3.3)$$

where P_{out} is the outer orbital period. We model this angular momentum evolution as a random walk, applying a single isotropically oriented kick to the outer orbit once per passage around the MBH. Each directional component of this 3D kick is drawn from $\Delta h_i = \mathcal{N}(0, (\langle dh \rangle / \sqrt{3})^2)$.

We randomly generate an entire trajectory of up to 1000 kicks prior to commencing the integration of a given binary. We start our simulation when the initial periapsis of the outer orbit is 5 times the tidal separation radius of the binary, defined as $r_{\text{p,out}} = 5R_{\text{TS}} \approx 5a(M_{\text{MBH}}/M_{\text{bin}})^{1/3}$ (Miller et al. 2005) where R_{TS} is the tidal separation radius of the binary and $M_{\text{bin}} = M_1 + M_2$ is the mass of the binary. The apoapsis distance is drawn to be consistent with the Bahcall-Wolf cusp with $n(r) \propto r^{-7/4}$, within the range $r_{\text{a,out}} \in [100r_{\text{p,out}}, 1 \text{ pc}]$. This yields a semimajor axis of $a_{\text{out}} = (r_{\text{p,out}} + r_{\text{a,out}})/2$ and a minimum initial eccentricity of $e_{\text{out}} > 0.98$. A kick trajectory is accepted if it results in the periapsis of the outer orbit reaching the tidal disruption radius of the binary’s hypothetical merger product.

3.4.3 Stellar tides

Many of our simulated binaries are on close orbits where stellar tides can efficiently circularise the orbit. We implement a simple equilibrium tide model (Hut 1981) between the inner binary stars, using equations formulated in Eggleton and Kiseleva-Eggleton (2001). We consider only the quadrupolar distortion of each star due to its inner binary companion, and ignore additional effects from stellar rotation. The periapsis of the inner binary is held constant while the eccentricity evolution follows

$$\frac{1}{e} \frac{de}{dt} = -V_1 - V_2, \quad (3.4)$$

Mass (M_{\odot})	α	β
< 0.43	0.23	2.3
$0.43 - 2.00$	1.00	4.0
$2.00 - 20.00$	1.50	3.5
$20.00 <$	2700.00	1.0

Table 3.1: Parameters used in the mass-luminosity relationship to obtain the approximate luminosity for a range of stellar masses (Duric (2012), Salaris and Cassisi (2005)).

where the component V_i for star i in the inner binary is calculated as

$$V_i = \frac{9}{\tau_{\text{TF},i}} \left[\frac{1 + (15/4)e^2 + (15/8)e^4 + (5/64)e^6}{(1 - e^2)^{13/2}} \right], \quad (3.5)$$

where $\tau_{\text{TF},i}$ is the tidal friction timescale. This timescale depends on the viscous timescale $\tau_{\text{v},i}$ and can be calculated using the expression (Eggleton and Kiseleva-Eggleton 2001)

$$\tau_{\text{TF},i} = \frac{\tau_{\text{v},i}}{9} \left(\frac{a}{R_i} \right)^8 \frac{M_i^2}{M_{\text{bin}} M_j} (1 - Q_i)^2, \quad (3.6)$$

where M_j is the mass of the binary companion. The term Q describes the quadrupole deformability of the star, and we adopt a value consistent with an $n = 3$ polytrope star, $Q = 0.021$ (calculated from the interpolation formula provided in Eggleton, Kiseleva, et al. (1998)). An estimate of the viscous timescale can be obtained based on the convective turnover timescale (Zahn 1977) and includes a factor from integrating the square of the rate-of-strain tensor of the time-dependent velocity field over the star (Eggleton and Kiseleva-Eggleton 2001), γ_i :

$$\tau_{\text{v},i} = \frac{1}{\gamma_i} \left(\frac{3M_i R_i^2}{L_i} \right)^{1/3}. \quad (3.7)$$

We set the value $\gamma_i = 0.01$ as in Eggleton and Kiseleva-Eggleton (ibid.), and the luminosity of the star, L , is determined from the mass-luminosity relationship $L/L_{\odot} = \alpha(M/M_{\odot})^{\beta}$, with the parameters α and β provided in Table 3.1.

As listed in Table 3.2, the tidal evolution timescale is much greater than the periap-

Timescale	Length (years)	Scaling
P_{bin}	$\sim 10^{-2}$	$\propto a^{3/2} M_{\text{bin}}^{-1/2}$
τ_{v}	$\sim 10^2$	$\propto M^{(1-\beta)/3} R^{2/3} \alpha^{-1}$
P_{out}	$\sim 10^4$	$\propto a_{\text{out}}^{3/2} M_{\text{MBH}}^{-1/2}$
τ_{LK}	$\sim 10^5$	$\propto P_{\text{out}}^2 P_{\text{bin}}^{-1} (1 - e_{\text{out}}^2)^{3/2}$
τ_{relax}	$\sim 10^9$	$\propto M_{\text{MBH}}^{3/2} a_{\text{out}}^{-3/2} n^{-1} m_*^2 \log 0.4N$
$\tau_{e=0.5}$	$\sim 10^7$	See section 3.4.3
$\tau_{e=0.9}$	$\sim 10^3$	"

Table 3.2: A comparison of relevant timescales relating to the binary. P_{bin} is the binary orbital period. The eccentricity evolution timescale is the median value for a given eccentricity.

sis passage timescale for our binaries. Therefore, we only include tidal evolution by adjusting the binary parameters between periapsis passages around the MBH. We calculate the median tidal evolution timescale $\tau_e = e/(de/dt)$ at two different fiducial values of the eccentricity to show the strong dependence on eccentricity. This timescale is longer than the $\sim 10^4$ -year outer orbital period for the majority of our binaries until the inner eccentricity reaches $e \sim 0.8$; above this value stellar tides become efficient in circularising half of the population over the course of an outer orbital period. We perform this tidal evolution using a fourth-order Runge-Kutta Cash-Karp method.

3.5 Results of numerical integrations

The internal angular momentum of stellar binaries gradually approaching the boundary of the loss cone around the MBH typically walks much more than their internal energy. Gradual tidal interactions between the stellar binary and the MBH cause only relatively small fluctuations in the inner binary's energy:

$$\frac{\delta E}{E} \sim \frac{\delta a}{a} \sim \frac{M_{\text{BH}}}{m_{\text{bin}}} \frac{a^3}{r_{\text{p,out}}^3} \sim \left(\frac{R_{\text{TS}}}{r_{\text{p,out}}} \right)^3. \quad (3.8)$$

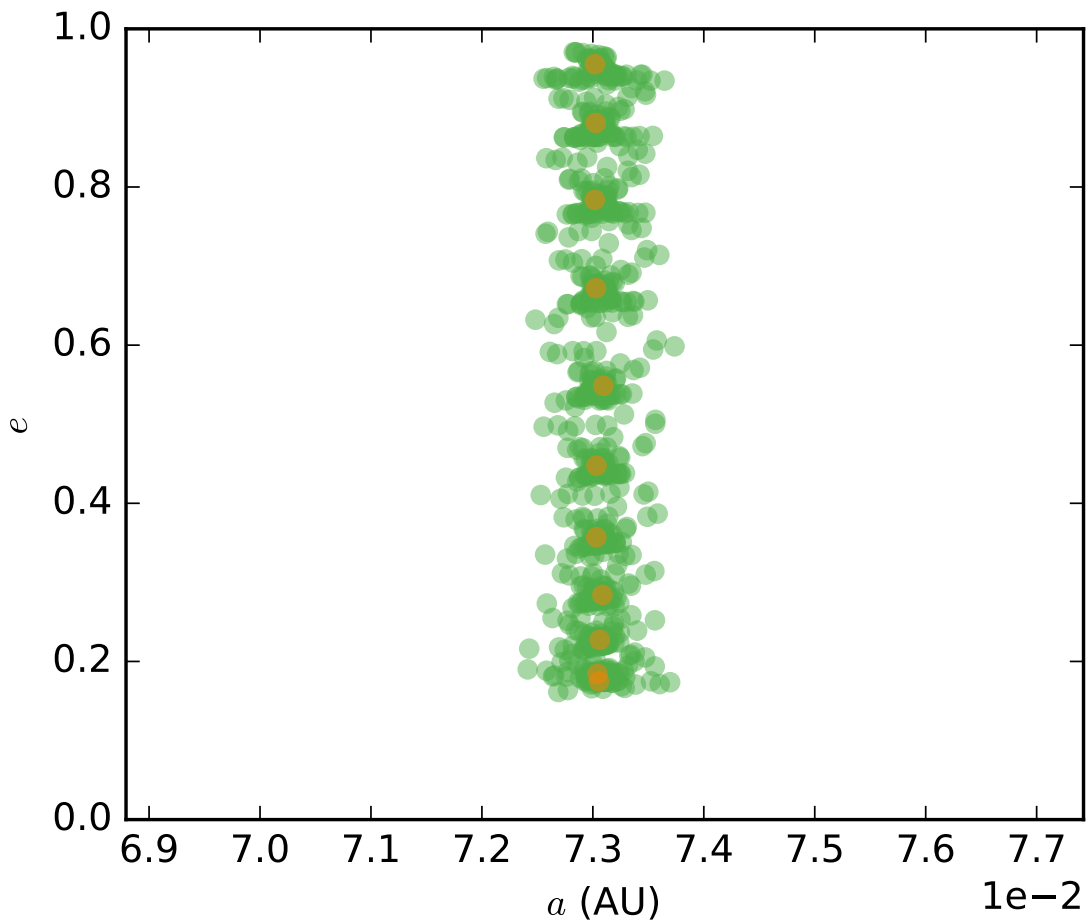


Figure 3.1: Typical evolution of a stellar binary gradually approaching the empty loss cone. The eccentricity is able to grow from an initially small value $e \sim 0.2$ to $e \gtrsim 0.95$ whilst the semimajor axis only varies slightly. Orange points mark the initial parameters of the inner binary for each orbit around the MBH, and the green points show the fluctuations during the near-periapsis passages.

On the other hand, the eccentricity of the inner binary is able to evolve efficiently through tidal torques. Figure 3.1 illustrates the typical evolution of a stellar binary; the eccentricity can be seen to grow from an initially small value of $e \sim 0.2$ to $e \gtrsim 0.95$ while the semimajor axis stays constant to within $\pm 1\%$.

These eccentricity fluctuations do not represent classical LK resonances. The LK timescale for $M_{\text{bin}} \ll M_{\text{MBH}}$ and $1 - e_{\text{out}} \ll 1$ is (Antognini 2015):

$$\tau_{\text{LK}} \approx \frac{8}{15\pi} \frac{P_{\text{out}}^2}{P_{\text{bin}}} (1 - e_{\text{out}}^2)^{3/2} \approx 0.5 \frac{r_{\text{p,out}}^{3/2}}{r_{\text{TS}}^{3/2}} \frac{P_{\text{out}}^2}{P_{\text{bin}}}. \quad (3.9)$$

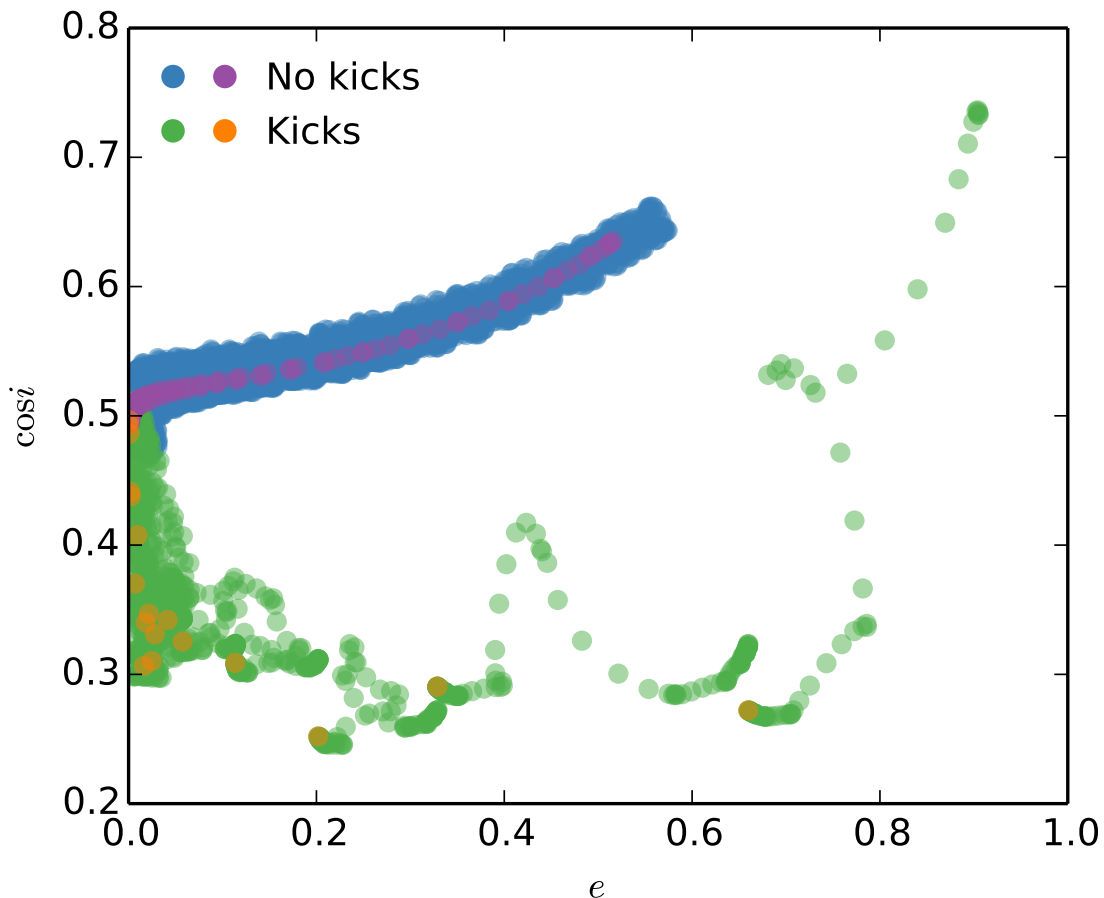


Figure 3.2: The evolution of the inner orbit of a typical stellar binary, showing the eccentricity and cosine of inclination over multiple trajectories around the MBH. Evolution is shown both with and without the angular momentum kicks to the outer orbit due to two-body relaxation. The primary colours show the elements throughout each trajectory around the MBH, whereas the secondary colours show the initial value for each periapsis passage.

Substituting in the initial periapsis of the systems we are investigating, $r_{p,\text{out}} = 5r_{\text{TS}}$, yields a LK timescale which is ~ 5 times the orbital period around the MBH (cf. Table 3.2). Therefore, the angular momentum kicks that the binary’s orbit around the MBH receives at apoapsis due to 2-body relaxation destroy the coherence required for LK resonance and suppress classical LK oscillations.

This suppression is demonstrated in Figure 3.2, where we compare the evolution of two otherwise identical systems, with and without angular momentum kicks applied far from the MBH. Without these kicks, the evolution is coherent and can be

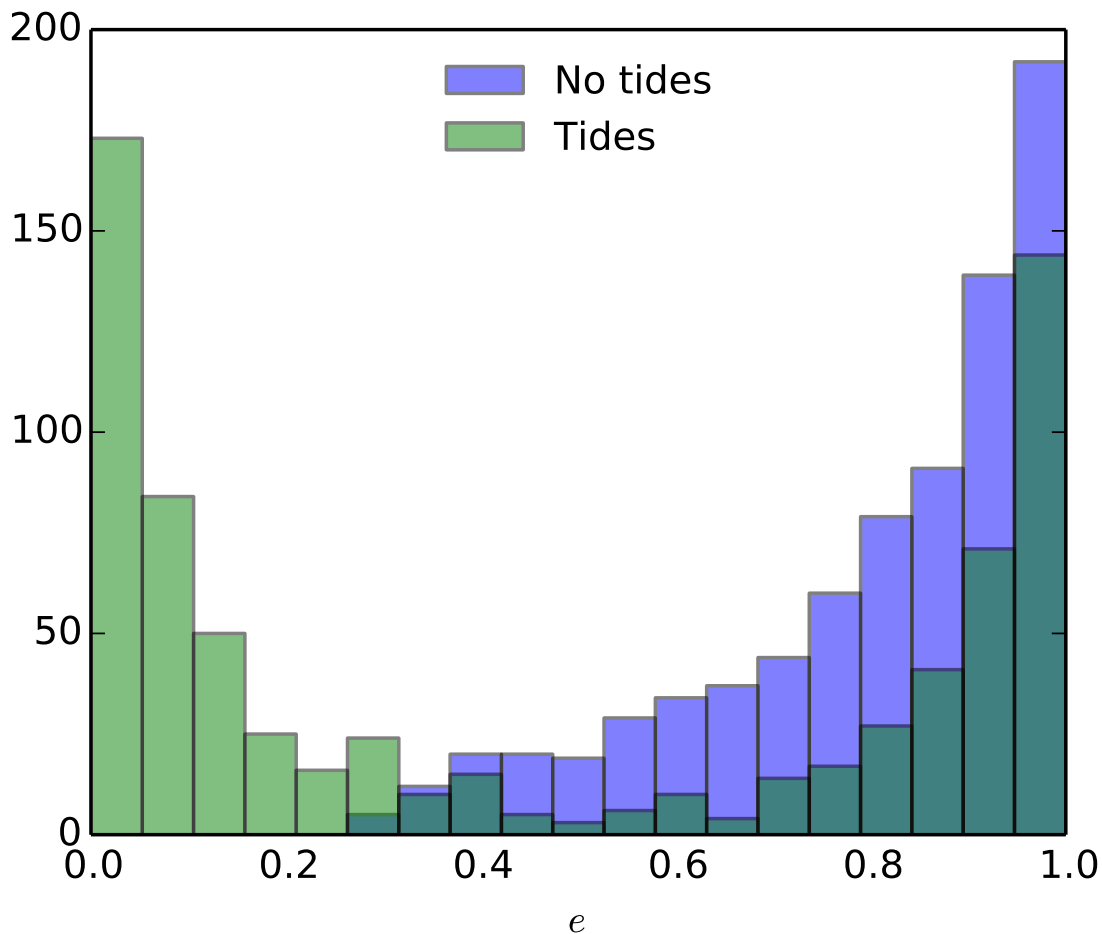


Figure 3.3: Final eccentricity distribution of merging systems, both with and without tides acting between the inner binary components.

seen to follow LK-like behaviour where the projection of the angular momentum of the binary onto the orbital angular momentum axis remains almost constant. When these kicks are included, the evolution of the inner orbital parameters appears chaotic and can reach very high eccentricities in tens of orbits around the MBH.

Such eccentricity excursions lead to a high fraction of tidally stimulated mergers. The vast majority of the simulated binaries, just under 80%, result in mergers. As expected, mergers typically happen at the highest eccentricities, when the inter-star separation at periapsis decreases. Although $\sim 85\%$ of the stellar binaries we simulated are initially circular, the final distribution is “super-thermal” (steeper than $p(e) = 2e$), as shown in Figure 3.3. The merger fraction is highest for initially close

binaries, which require smaller eccentricity excursions for merger (see Figure 3.4). The remaining binaries are tidally separated, with one of the stars ejected as a hypervelocity star.

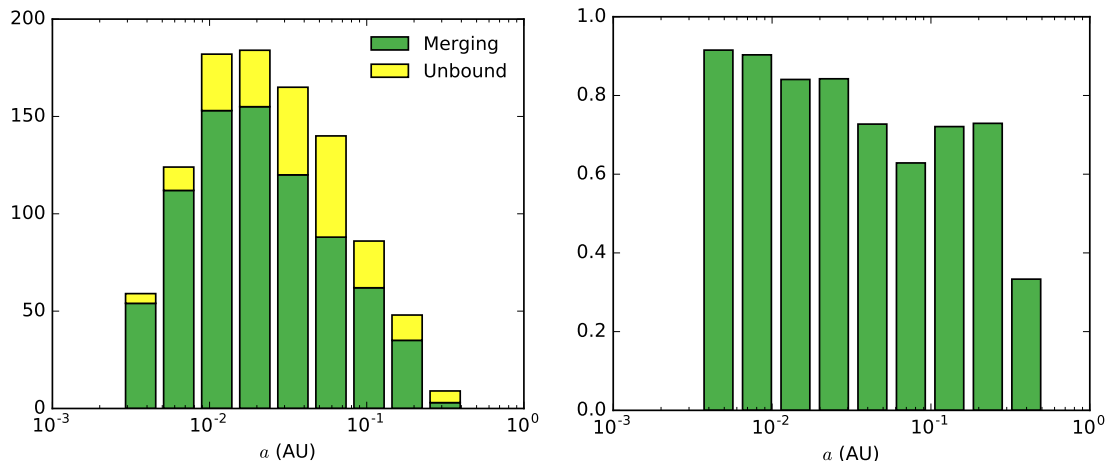


Figure 3.4: Initial binary semimajor axes categorised by the binary’s fate (no stellar tides). The right image shows the merging fraction in each bin.

The inclusion of stellar tides slightly decreases the overall fraction of mergers to $\sim 75\%$, as high-eccentricity excursions are partially suppressed by tides. Figure 3.3 shows a bimodal distribution of inner binary eccentricities once tides are included, with many binaries circularised by tides. While tides circularise these binaries, they also harden them; this ensures that merger rather than tidal separation remains the most likely evolutionary outcome. The dependence of the merger fraction on initial separation with stellar tides remains similar to Figure 3.4 and is not included here.

The circularising impact of stellar tides significantly changes the collision dynamics when the merger happens. The relative velocities between colliding stars are shown in Figure 3.5. Collisions in the absence of stellar tides, which typically happen at a high impact velocity, reaching the escape velocity at the surface of the more massive star, are likely to lead to significant mass loss and an extended merger product. Meanwhile, grazing collisions in the tidally circularised binaries can have significantly lower relative velocities.

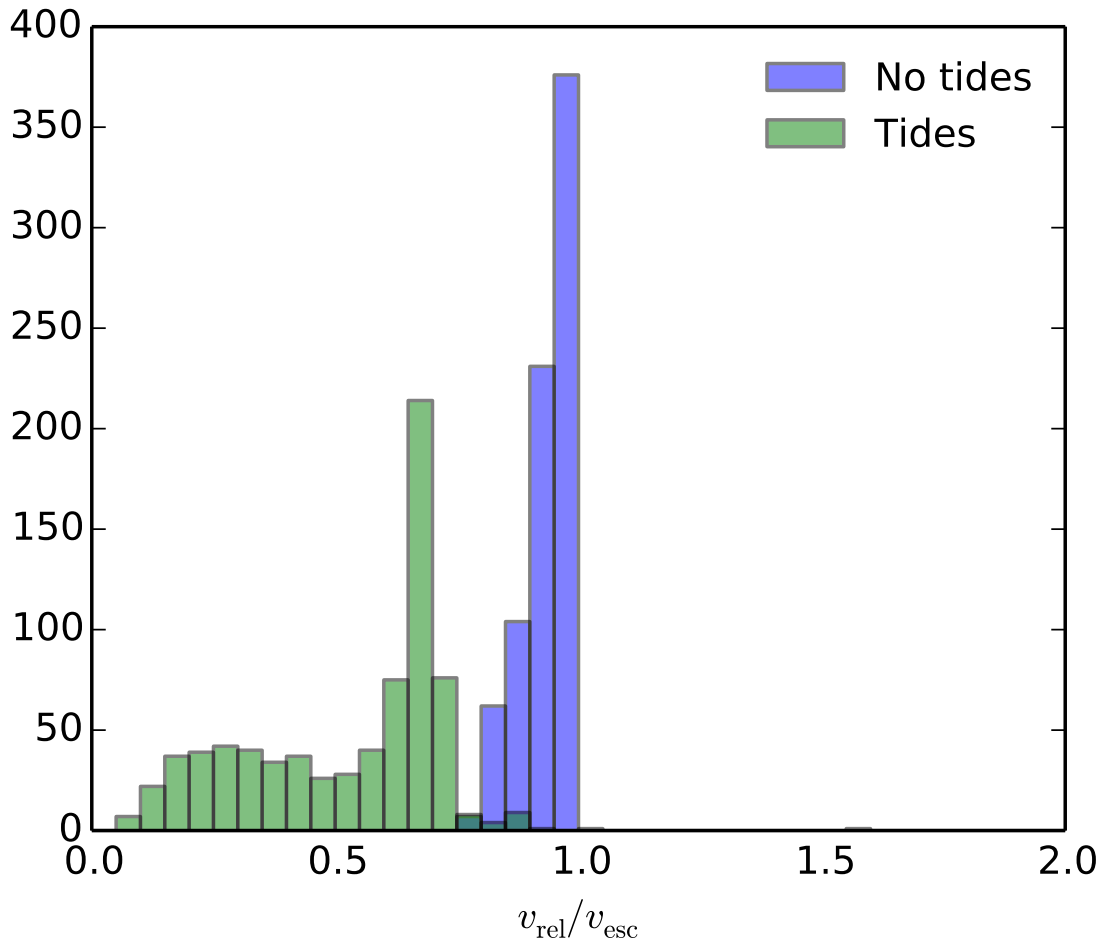


Figure 3.5: Relative velocity at point of impact for merging systems in units of the escape velocity of the primary star, with and without stellar tides.

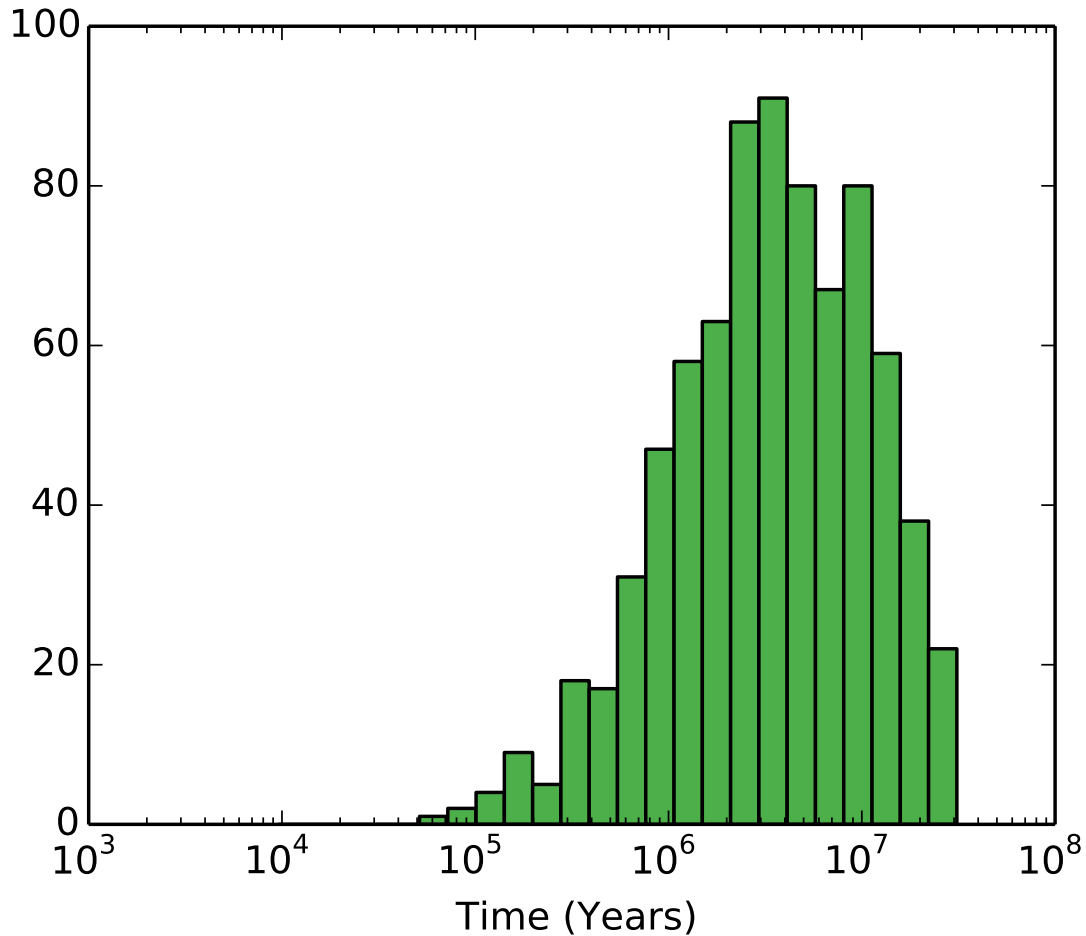


Figure 3.6: Time delay distribution between the tidally stimulated mergers and the tidal disruption of the merger product by the MBH in our simulations, chosen so that the merger product would approach to within its tidal disruption periapsis of the MBH within 1000 outer orbits. A tail of longer time delays is omitted through this choice; see section 3.6.

Among the simulated population of binaries most still require ~ 100 orbits after merger before the merger product is disrupted. Figure 3.6 shows the distribution of the time between the tidally stimulated merger and the tidal disruption of the merger product, under the assumption that the merger itself does not alter the trajectory around the MBH. Merger products can be disrupted in as little as $\sim 10^5$ years. The inclusion of stellar tides does not appreciably change this distribution.

Although mergers are more common than binary tidal separations in our simulations, a considerable number of hypervelocity star (HVS) are still produced. The

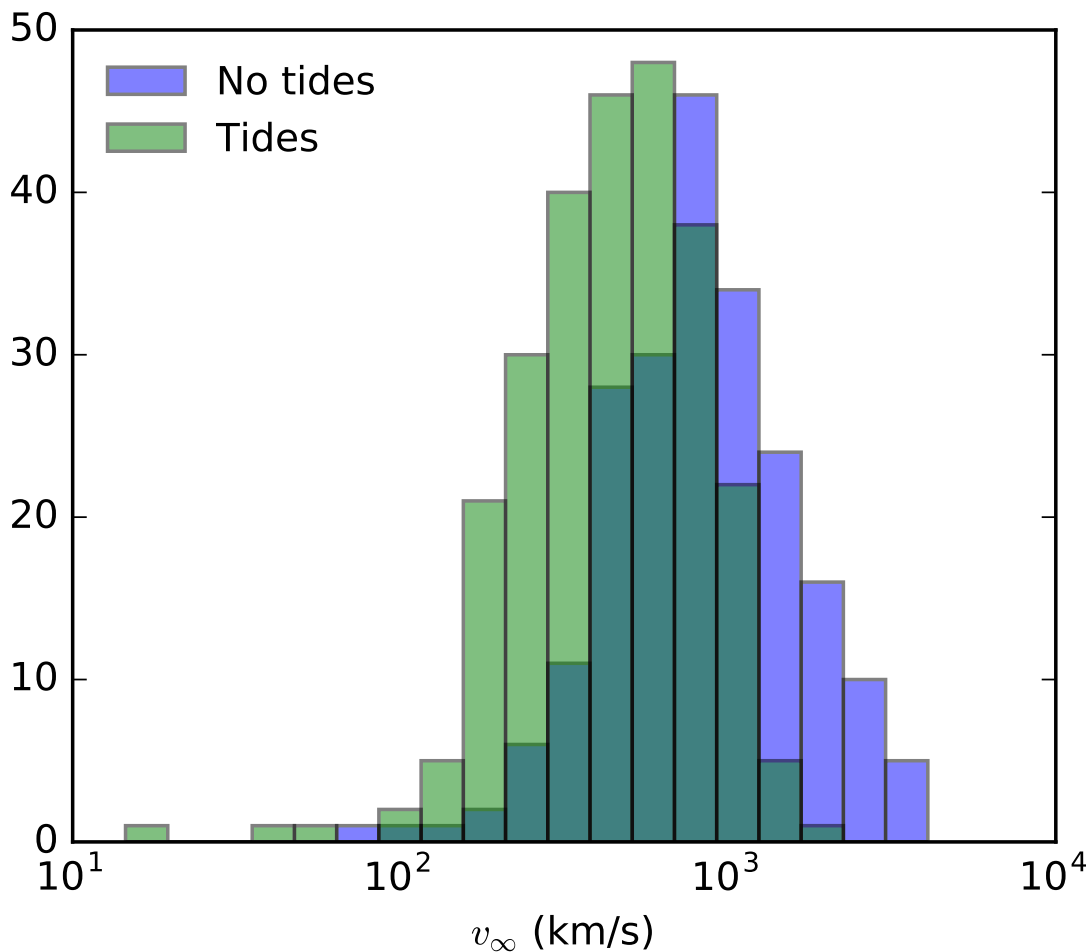


Figure 3.7: The distribution of hyperbolic excess velocities of tidally ejected stars.

distribution of hyperbolic excess velocities of the ejected stars in tidally separated binaries $v_\infty^2 = v_*^2 - 2GM_{\text{MBH}}/r$, where v_* is the star’s current velocity and r is the radial distance from the star to the MBH, is shown in Figure 3.7. A number of stars are ejected with velocities exceeding 1000 km s^{-1} . Stellar tides generally reduce ejection velocities.

3.6 Discussion

We simulated the dynamics of stellar binaries in the empty loss cone around an MBH. These systems preferentially merge over becoming tidally separated as the tide on the

binary from the MBH efficiently drives eccentricity evolution without significantly affecting the binary's energy (see Figure 3.1). We found that stellar binaries on highly eccentric orbits that gradually diffuse in angular momentum produce mergers in $\gtrsim 75\%$ of our simulations. The remaining binaries become tidally separated and produce HVS with hyperbolic excess velocities up to 1000 km s^{-1} . Consequently, more than ten percent of all tidal disruption events should be disruptions of merger products.

Such mergers may generate strong magnetic fields through a dynamo mechanism (Wickramasinghe et al. 2014). When the merger products are subsequently tidally disrupted by the MBH, these strong magnetic fields could play a crucial role in powering the prompt formation of jets such as observed in Swift J164449.3+573451 (Giannios and Metzger 2011).

Stellar tides between the binary components slightly reduce the merging fraction, and significantly reduce the eccentricity of the binary at the time of merger for many systems, thereby reducing the collision velocity. We used an equilibrium tide model that only includes quadrupolar terms in the stellar deformation and loses accuracy at high eccentricity. A more careful treatment of tides would include a dynamical tide model (e.g., Fabian et al. 1975; Zahn 1977; Press and Teukolsky 1977) and additional effects from stellar rotation and tides raised by the MBH. This would increase tidal efficiency for very eccentric systems, possibly further reducing the eccentricity and relative velocity at merger.

The treatment of the collision could be improved with more detailed hydrodynamical simulations to more accurately determine the structure of the merger product (Antonini, Lombardi, et al. 2011), the mass loss from the system, and any change in the trajectory of the merger product following merger, which we have ignored in our simplified analysis. Moreover, Roche lobe overflow as the stars approach prior to merger could lead to a softer collision.

Stephan et al. (2016) found that stellar evolution played an important role in the evolution of 65% of the binaries they simulated in orbit around an MBH. However, stellar evolution is unlikely to significantly affect our results, as these systems evolve on a typical timescale of \sim Myrs.

We assumed a Bahcall-Wolf cusp around the MBH. The stellar density affects the efficiency of 2-body relaxation at a given radius (see Eq. 3.2); therefore, a different stellar density profile would shift the boundary between the empty loss cone and the full loss cone. However, the behaviour of binaries within the empty loss cone for tidal separation will not be significantly affected, and \sim 50% of tidally impacted binaries would still come from the empty loss cone regime.

We populated stellar binaries according to the observed mass, period, and eccentricity distributions (see section 3.4.1). If tighter/wider orbits are favoured, the fraction of tidally induced mergers would increase/decrease, as indicated by the anti-correlation between the orbital separation and merger fraction in Figure 3.4. Meanwhile, the component mass is not significantly correlated with the fate of the binary; therefore, varying the mass distribution should not appreciably impact the merger fraction. The vast majority of the relatively short-period binaries analysed here are expected to be tidally circularised, with negligible initial eccentricities.

The shortest-period binaries with the highest orbital velocity are expected to produce the fastest hypervelocity stars when the binary is tidally separated by an MBH. However, our simulations show that the closest binaries are preferentially merged rather than tidally separated in the empty loss cone. This depletes the high-velocity tail of the hypervelocity star distribution, especially when stellar tides are included. The absence of the high-velocity tail appears consistent with observations of Galactic hypervelocity stars (Rossi, Kobayashi, et al. 2014; Rossi, Marchetti, et al. 2017). However, the tidally stimulated merger fraction is significantly lower for binaries in the full loss cone (Mandel and Levin 2015), so full loss cone binaries could still

provide contributions to the high-velocity tail unless other effects suppress tidal separations of close binaries in that regime.

Our simulations were selected to focus on binaries whose angular momentum random walk around the MBH will bring the merger product to a sufficiently small periapsis for tidal disruption within 1000 orbits. The actual fraction of merger products disrupted within a few million years is $\lesssim 10\%$. A long delay could allow the merger product to return to equilibrium, reducing the stellar radius, but an enhanced magnetic field could be retained in the radiative zones of the merger product (Braithwaite and Spruit 2004). Moreover, many merger products will come sufficiently close to the MBH for partial disruption long before full tidal disruption, and the extended merger products will be particularly susceptible to partial disruptions. Guillochon and McCourt (2017) argue that such disruptions can increase the magnetic field by factors of ~ 20 . The combined effect of a merger followed by repeated partial disruptions can have a truly dramatic effect on the star's magnetic field. Tchekhovskoy et al. (2014b) argued that strong coherent fields are required for prompt jet formation. Parfrey et al. (2015) advocate a less stringent requirement for the large-scale field and the ability of small-scale fields to produce jets when interacting with a spinning black hole. Clearly, strong initial fields prior to disc formation can enhance the magnetic activity of the disc and jet formation. Tidally stimulated stellar mergers could thus be an important ingredient in the production of jets during subsequent TDEs.

Acknowledgements

Simulations in this paper made use of the IAS15 N-body integrator (Rein and Spiegel 2015) found in the REBOUND package (Rein and Liu 2012), which can be downloaded at <http://github.com/hannorein/rebound>. We are grateful to Will Farr,

James Guillochon, Elena Maria Rossi and Alison Farmer for useful discussions. IM acknowledges partial support by the STFC and by the National Science Foundation under Grant No. NSF PHY11-25915. YL acknowledges research support by the Australian Research Council Future Fellowship.

References

- [1] J. M. O. Antognini. “Timescales of Kozai-Lidov oscillations at quadrupole and octupole order in the test particle limit”. In: MNRAS 452 (Oct. 2015), pp. 3610–3619. DOI: 10.1093/mnras/stv1552. arXiv: 1504.05957 [astro-ph.EP].
- [2] F. Antonini, J. Faber, et al. “Tidal Breakup of Binary Stars at the Galactic Center and Its Consequences”. In: ApJ 713 (Apr. 2010), pp. 90–104. DOI: 10.1088/0004-637X/713/1/90. arXiv: 0909.1959.
- [3] F. Antonini, J. C. Lombardi Jr., and D. Merritt. “Tidal Breakup of Binary Stars at the Galactic Center. II. Hydrodynamic Simulations”. In: ApJ 731, 128 (Apr. 2011), p. 128. DOI: 10.1088/0004-637X/731/2/128. arXiv: 1008.5369.
- [4] I. Arcavi et al. “A Continuum of H- to He-rich Tidal Disruption Candidates With a Preference for E+A Galaxies”. In: ApJ 793, 38 (Sept. 2014), p. 38. DOI: 10.1088/0004-637X/793/1/38. arXiv: 1405.1415 [astro-ph.HE].
- [5] J. S. Bloom et al. “A Possible Relativistic Jetted Outburst from a Massive Black Hole Fed by a Tidally Disrupted Star”. In: *Science* 333 (July 2011), p. 203. DOI: 10.1126/science.1207150. arXiv: 1104.3257 [astro-ph.HE].
- [6] C. Bonnerot, D. J. Price, et al. “Magnetic field evolution in tidal disruption events”. In: *ArXiv e-prints* (Nov. 2016). arXiv: 1611.09853 [astro-ph.HE].
- [7] C. Bonnerot, E. M. Rossi, et al. “Disc formation from tidal disruptions of stars on eccentric orbits by Schwarzschild black holes”. In: MNRAS 455 (Jan.

- 2016), pp. 2253–2266. DOI: 10.1093/mnras/stv2411. arXiv: 1501.04635 [astro-ph.HE].
- [8] B. Bradnick, I. Mandel, and Y. Levin. “Stellar binaries in galactic nuclei: tidally stimulated mergers followed by tidal disruptions”. In: *Monthly Notices of the Royal Astronomical Society* 469.2 (2017), p. 2042. DOI: 10.1093/mnras/stx1007. eprint: /oup/backfile/content_public/journal/mnras/469/2/10.1093_mnras_stx1007/1/stx1007.pdf. URL: <http://dx.doi.org/10.1093/mnras/stx1007>.
- [9] J. Braithwaite and H. C. Spruit. “A fossil origin for the magnetic field in A stars and white dwarfs”. In: *Nature* 431 (Oct. 2004), pp. 819–821. DOI: 10.1038/nature02934. eprint: astro-ph/0502043.
- [10] W. R. Brown. “Hypervelocity Stars”. In: *ARA&A* 53 (Aug. 2015), pp. 15–49. DOI: 10.1146/annurev-astro-082214-122230.
- [11] W. R. Brown et al. “Discovery of an Unbound Hypervelocity Star in the Milky Way Halo”. In: *ApJ* 622 (Mar. 2005), pp. L33–L36. DOI: 10.1086/429378. eprint: astro-ph/0501177.
- [12] D. N. Burrows et al. “Relativistic jet activity from the tidal disruption of a star by a massive black hole”. In: *Nature* 476 (Aug. 2011), pp. 421–424. DOI: 10.1038/nature10374. arXiv: 1104.4787 [astro-ph.HE].
- [13] R. Chornock et al. “The Ultraviolet-bright, Slowly Declining Transient PS1-11af as a Partial Tidal Disruption Event”. In: *ApJ* 780, 44 (Jan. 2014), p. 44. DOI: 10.1088/0004-637X/780/1/44. arXiv: 1309.3009.
- [14] A. Duquennoy and M. Mayor. “Multiplicity among solar-type stars in the solar neighbourhood. II - Distribution of the orbital elements in an unbiased sample”. In: *A&A* 248 (Aug. 1991), pp. 485–524.
- [15] Neb Duric. *Advanced Astrophysics*. Cambridge University Press, 2012.

-
- [16] P. P. Eggleton. “Approximations to the radii of Roche lobes”. In: *ApJ* 268 (May 1983), p. 368. DOI: 10.1086/160960.
- [17] P. P. Eggleton, L. G. Kiseleva, and P. Hut. “The Equilibrium Tide Model for Tidal Friction”. In: *ApJ* 499 (May 1998), pp. 853–870. eprint: astro-ph/9801246.
- [18] P. P. Eggleton and L. Kiseleva-Eggleton. “Orbital Evolution in Binary and Triple Stars, with an Application to SS Lacertae”. In: *ApJ* 562 (Dec. 2001), pp. 1012–1030. DOI: 10.1086/323843. eprint: astro-ph/0104126.
- [19] A. C. Fabian, J. E. Pringle, and M. J. Rees. “Tidal capture formation of binary systems and X-ray sources in globular clusters”. In: *MNRAS* 172 (Aug. 1975), 15p–18p. DOI: 10.1093/mnras/172.1.15P.
- [20] S. Gezari, R. Chornock, et al. “An ultraviolet-optical flare from the tidal disruption of a helium-rich stellar core”. In: *Nature* 485 (May 2012), pp. 217–220. DOI: 10.1038/nature10990. arXiv: 1205.0252 [astro-ph.CO].
- [21] S. Gezari, T. Heckman, et al. “Luminous Thermal Flares from Quiescent Supermassive Black Holes”. In: *ApJ* 698 (June 2009), pp. 1367–1379. DOI: 10.1088/0004-637X/698/2/1367. arXiv: 0904.1596 [astro-ph.CO].
- [22] D. Giannios and B. D. Metzger. “Radio transients from stellar tidal disruption by massive black holes”. In: *MNRAS* 416 (Sept. 2011), pp. 2102–2107. DOI: 10.1111/j.1365-2966.2011.19188.x. arXiv: 1102.1429 [astro-ph.HE].
- [23] A. Gould and A. C. Quillen. “Sagittarius A* Companion S0-2: A Probe of Very High Mass Star Formation”. In: *ApJ* 592 (Aug. 2003), pp. 935–940. DOI: 10.1086/375840. eprint: astro-ph/0302437.
- [24] A. Gualandris, S. Portegies Zwart, and M. S. Sipior. “Three-body encounters in the Galactic Centre: the origin of the hypervelocity star SDSS J090745.0+024507”.

- In: MNRAS 363 (Oct. 2005), pp. 223–228. DOI: 10.1111/j.1365-2966.2005.09433.x. eprint: astro-ph/0507365.
- [25] J. Guillochon and M. McCourt. “Simulations of Magnetic Fields in Tidally Disrupted Stars”. In: ApJ 834, L19 (Jan. 2017), p. L19. DOI: 10.3847/2041-8213/834/2/L19. arXiv: 1609.08160 [astro-ph.HE].
- [26] J. Guillochon and E. Ramirez-Ruiz. “Hydrodynamical Simulations to Determine the Feeding Rate of Black Holes by the Tidal Disruption of Stars: The Importance of the Impact Parameter and Stellar Structure”. In: ApJ 767, 25 (Apr. 2013), p. 25. DOI: 10.1088/0004-637X/767/1/25. arXiv: 1206.2350 [astro-ph.HE].
- [27] J. G. Hills. “Hyper-velocity and tidal stars from binaries disrupted by a massive Galactic black hole”. In: Nature 331 (Feb. 1988), pp. 687–689. DOI: 10.1038/331687a0.
- [28] T. W.-S. Holoien et al. “ASASSN-14ae: a tidal disruption event at 200 Mpc”. In: MNRAS 445 (Dec. 2014), pp. 3263–3277. DOI: 10.1093/mnras/stu1922. arXiv: 1405.1417.
- [29] P. Hut. “Tidal evolution in close binary systems”. In: A&A 99 (June 1981), pp. 126–140.
- [30] R. Kippenhahn and A. Weigert. *Stellar structure and evolution*. Springer-Verlag, 1994.
- [31] S. Komossa and J. Greiner. “Discovery of a giant and luminous X-ray outburst from the optically inactive galaxy pair RX J1242.6-1119”. In: A&A 349 (Sept. 1999), pp. L45–L48. eprint: astro-ph/9908216.
- [32] S. Komossa, J. Halpern, et al. “A Huge Drop in the X-Ray Luminosity of the Nonactive Galaxy RX J1242.6-1119A, and the First Postflare Spectrum:

-
- Testing the Tidal Disruption Scenario”. In: ApJ 603 (Mar. 2004), pp. L17–L20. DOI: 10.1086/382046. eprint: astro-ph/0402468.
- [33] Y. Kozai. “Secular perturbations of asteroids with high inclination and eccentricity”. In: AJ 67 (Nov. 1962), p. 591. DOI: 10.1086/108790.
- [34] P. Kroupa. “On the variation of the initial mass function”. In: MNRAS 322 (Apr. 2001), pp. 231–246. DOI: 10.1046/j.1365-8711.2001.04022.x. eprint: astro-ph/0009005.
- [35] A. J. Levan et al. “An Extremely Luminous Panchromatic Outburst from the Nucleus of a Distant Galaxy”. In: *Science* 333 (July 2011), p. 199. DOI: 10.1126/science.1207143. arXiv: 1104.3356 [astro-ph.HE].
- [36] M. L. Lidov. “The evolution of orbits of artificial satellites of planets under the action of gravitational perturbations of external bodies”. In: Planet. Space Sci. 9 (Oct. 1962), pp. 719–759. DOI: 10.1016/0032-0633(62)90129-0.
- [37] A. P. Lightman and S. L. Shapiro. “The distribution and consumption rate of stars around a massive, collapsed object”. In: ApJ 211 (Jan. 1977), pp. 244–262. DOI: 10.1086/154925.
- [38] G. Lodato, A. R. King, and J. E. Pringle. “Stellar disruption by a supermassive black hole: is the light curve really proportional to $t^{-5/3}$?” In: MNRAS 392 (Jan. 2009), pp. 332–340. DOI: 10.1111/j.1365-2966.2008.14049.x. arXiv: 0810.1288.
- [39] M. MacLeod, J. Guillochon, and E. Ramirez-Ruiz. “The Tidal Disruption of Giant Stars and their Contribution to the Flaring Supermassive Black Hole Population”. In: ApJ 757, 134 (Oct. 2012), p. 134. DOI: 10.1088/0004-637X/757/2/134. arXiv: 1206.2922 [astro-ph.HE].

- [40] J. Magorrian and S. Tremaine. “Rates of tidal disruption of stars by massive central black holes”. In: *MNRAS* 309 (Oct. 1999), pp. 447–460. DOI: 10.1046/j.1365-8711.1999.02853.x. eprint: astro-ph/9902032.
- [41] I. Mandel and Y. Levin. “Double Tidal Disruptions in Galactic Nuclei”. In: *ApJ* 805, L4 (May 2015), p. L4. DOI: 10.1088/2041-8205/805/1/L4. arXiv: 1504.02787 [astro-ph.SR].
- [42] D. Merritt. “Single and Binary Black Holes and their Influence on Nuclear Structure”. In: *Coevolution of Black Holes and Galaxies* (2004), p. 263. eprint: astro-ph/0301257.
- [43] M. C. Miller et al. “Binary Encounters with Supermassive Black Holes: Zero-Eccentricity LISA Events”. In: *ApJ* 631 (Oct. 2005), pp. L117–L120. DOI: 10.1086/497335. eprint: astro-ph/0507133.
- [44] E. Öpik. “Statistical Studies of Double Stars: On the Distribution of Relative Luminosities and Distances of Double Stars in the Harvard Revised Photometry North of Declination -31deg”. In: *Publications of the Tartu Astrofizika Observatory* 25 (1924).
- [45] K. Parfrey, D. Giannios, and A. M. Beloborodov. “Black hole jets without large-scale net magnetic flux”. In: *MNRAS* 446 (Jan. 2015), pp. L61–L65. DOI: 10.1093/mnrasl/slu162. arXiv: 1410.0374 [astro-ph.HE].
- [46] E. S. Phinney. “Manifestations of a Massive Black Hole in the Galactic Center”. In: *The Center of the Galaxy*. Ed. by M. Morris. Vol. 136. IAU Symposium. 1989, p. 543.
- [47] W. H. Press and S. A. Teukolsky. “On formation of close binaries by two-body tidal capture”. In: *ApJ* 213 (Apr. 1977), pp. 183–192. DOI: 10.1086/155143.
- [48] S. Prodan, F. Antonini, and H. B. Perets. “Secular Evolution of Binaries near Massive Black Holes: Formation of Compact Binaries, Merger/Collision

- Products and G2-like Objects”. In: ApJ 799, 118 (Feb. 2015), p. 118. DOI: 10.1088/0004-637X/799/2/118. arXiv: 1405.6029.
- [49] M. J. Rees. “Tidal disruption of stars by black holes of 10 to the 6th-10 to the 8th solar masses in nearby galaxies”. In: Nature 333 (June 1988), pp. 523–528. DOI: 10.1038/333523a0.
- [50] M. M. Reggiani and M. R. Meyer. “Binary Formation Mechanisms: Constraints from the Companion Mass Ratio Distribution”. In: ApJ 738, 60 (Sept. 2011), p. 60. DOI: 10.1088/0004-637X/738/1/60. arXiv: 1106.3064.
- [51] H. Rein and S.-F. Liu. “REBOUND: an open-source multi-purpose N-body code for collisional dynamics”. In: A&A 537, A128 (Jan. 2012), A128. DOI: 10.1051/0004-6361/201118085. arXiv: 1110.4876 [astro-ph.EP].
- [52] H. Rein and D. S. Spiegel. “IAS15: a fast, adaptive, high-order integrator for gravitational dynamics, accurate to machine precision over a billion orbits”. In: MNRAS 446 (Jan. 2015), pp. 1424–1437. DOI: 10.1093/mnras/stu2164. arXiv: 1409.4779 [astro-ph.EP].
- [53] E. M. Rossi, S. Kobayashi, and R. Sari. “The Velocity Distribution of Hypervelocity Stars”. In: ApJ 795, 125 (Nov. 2014), p. 125. DOI: 10.1088/0004-637X/795/2/125. arXiv: 1307.1134.
- [54] E. M. Rossi, T. Marchetti, et al. “Joint constraints on the Galactic dark matter halo and GC from hypervelocity stars”. In: MNRAS (Jan. 2017). DOI: 10.1093/mnras/stx098. arXiv: 1608.02000.
- [55] Maurizio Salaris and Santi Cassisi. *Evolution of stars and stellar populations*. John Wiley & Sons, 2005.
- [56] H. Sana et al. “The VLT-FLAMES Tarantula Survey. VIII. Multiplicity properties of the O-type star population”. In: A&A 550, A107 (Feb. 2013), A107. DOI: 10.1051/0004-6361/201219621. arXiv: 1209.4638 [astro-ph.SR].

- [57] R. Sari, S. Kobayashi, and E. M. Rossi. “Hypervelocity Stars and the Restricted Parabolic Three-Body Problem”. In: *ApJ* 708 (Jan. 2010), pp. 605–614. DOI: 10.1088/0004-637X/708/1/605. arXiv: 0911.1136 [astro-ph.HE].
- [58] R.-F. Shen and C. D. Matzner. “Evolution of Accretion Disks in Tidal Disruption Events”. In: *ApJ* 784, 87 (Apr. 2014), p. 87. DOI: 10.1088/0004-637X/784/2/87. arXiv: 1305.5570 [astro-ph.HE].
- [59] H. Shiokawa et al. “General Relativistic Hydrodynamic Simulation of Accretion Flow from a Stellar Tidal Disruption”. In: *ApJ* 804, 85 (May 2015), p. 85. DOI: 10.1088/0004-637X/804/2/85. arXiv: 1501.04365 [astro-ph.HE].
- [60] L. Spitzer Jr. and M. H. Hart. “Random Gravitational Encounters and the Evolution of Spherical Systems. I. Method”. In: *ApJ* 164 (Mar. 1971), p. 399. DOI: 10.1086/150855.
- [61] A. P. Stephan et al. “Merging Binaries in the Galactic Center: The eccentric Kozai-Lidov mechanism with stellar evolution”. In: *ArXiv e-prints* (Mar. 2016). arXiv: 1603.02709 [astro-ph.SR].
- [62] L. E. Strubbe and E. Quataert. “Optical flares from the tidal disruption of stars by massive black holes”. In: *MNRAS* 400 (Dec. 2009), pp. 2070–2084. DOI: 10.1111/j.1365-2966.2009.15599.x. arXiv: 0905.3735.
- [63] A. Tchekhovskoy et al. “Swift J1644+57 gone MAD: the case for dynamically important magnetic flux threading the black hole in a jetted tidal disruption event”. In: *MNRAS* 437 (Jan. 2014), pp. 2744–2760. DOI: 10.1093/mnras/stt2085. arXiv: 1301.1982 [astro-ph.HE].
- [64] A. Tchekhovskoy et al. “Swift J1644+57 gone MAD: the case for dynamically important magnetic flux threading the black hole in a jetted tidal disruption event”. In: *MNRAS* 437 (Jan. 2014), pp. 2744–2760. DOI: 10.1093/mnras/stt2085. arXiv: 1301.1982 [astro-ph.HE].

-
- [65] S. van Velzen et al. “Optical Discovery of Probable Stellar Tidal Disruption Flares”. In: *ApJ* 741, 73 (Nov. 2011), p. 73. DOI: 10.1088/0004-637X/741/2/73. arXiv: 1009.1627 [astro-ph.CO].
- [66] D. T. Wickramasinghe, C. A. Tout, and L. Ferrario. “The most magnetic stars”. In: *MNRAS* 437 (Jan. 2014), pp. 675–681. DOI: 10.1093/mnras/stt1910. arXiv: 1310.2696 [astro-ph.SR].
- [67] Q. Yu and S. Tremaine. “Ejection of Hypervelocity Stars by the (Binary) Black Hole in the Galactic Center”. In: *ApJ* 599 (Dec. 2003), pp. 1129–1138. DOI: 10.1086/379546. eprint: astro-ph/0309084.
- [68] J.-P. Zahn. “Tidal friction in close binary stars”. In: *A&A* 57 (May 1977), pp. 383–394.
- [69] B. A. Zauderer et al. “Birth of a relativistic outflow in the unusual γ -ray transient Swift J164449.3+573451”. In: *Nature* 476 (Aug. 2011), pp. 425–428. DOI: 10.1038/nature10366. arXiv: 1106.3568 [astro-ph.HE].
- [70] C. Zhu et al. “Magnetized Moving Mesh Merger of a Carbon-Oxygen White Dwarf Binary”. In: *ApJ* 806, L1 (June 2015), p. L1. DOI: 10.1088/2041-8205/806/1/L1. arXiv: 1504.01732 [astro-ph.SR].

Chapter 4

Stellar population synthesis and interpolating stellar tracks

4.1 Introduction

The work presented in this chapter moves away from n-body simulations and instead follows the ongoing work to produce a method for rapidly calculating the stellar evolution of single stars. Given an initial metallicity and mass of a star, a stellar evolutionary track can be obtained which contains the stellar properties from the star of the main sequence through to the end of hydrogen burning, the white dwarf cooling sequence (WDCS) or the end of carbon burning depending on the star's initial mass. Stellar evolutionary tracks have already been computed using Modules for Experiments in Stellar Astrophysics (MESA) (Paxton, Bildsten, et al. 2011; Paxton, Cantiello, et al. 2013; Paxton, Marchant, et al. 2015) over many intervals in initial stellar mass and metallicity as part of MESA Isochrones and Stellar Tracks (MIST) (Dotter 2016; Choi et al. 2016). These stellar tracks can be used for grid-based interpolation, where new stellar tracks are obtained by interpolating between surrounding points on the grid.

The main goal of this project is to be able to obtain stellar evolution tracks of stars over a wide range of mass and metallicities rapidly. The output will then be integrated into the Compact Object Mergers: Population Astrophysics and Statistics (COMPAS) project (Stevenson et al. 2017) to provide an additional channel of single stellar evolution alongside single-star evolution (SSE). This will help alleviate some limitations of evolving more massive stars without requiring extrapolation of for more massive stars between 50 and 300 solar masses (as used currently using SSE formulae, see Hurley et al. (2000)), and can also be incorporated into the binary evolution code which also considers additional effects such as mass transfer.

The chapter is laid out as follows. Section 4.2 details the methods used to create a database containing the interpolation grid and performing the interpolation, calculating the remnant mass of more massive stars and generating mass distributions. Section 4.3 contains some results from using the code, demonstrating stellar evo-

lution for a range of properties and generating a cluster of single stars. These are also compared to the current single star evolution provided in COMPAS using SSE. Last of all, section 4.4 discusses the current results and status of the project, and its future.

4.2 Methods

The equivalent evolutionary point (EEP) stellar evolution track files are obtained for each simulated star in MIST¹. Currently tracks are provided for non-rotating stars as well as stars rotating at $v/v_{\text{crit}} = 0.4$, 40% of the break-up speed. These stellar track files cover a range of initial masses in the range 0.1 - 300.0 M_{\odot} and metallicities, $-4.0 \leq [Z/H] < 0.5$ until the end of hydrogen burning, the WDCS or carbon burning depending on whether the star is low-mass or high-mass (although it is noted that the stellar evolution ends at core helium burning for metallicities $[Z/H] < -2.0$). These files are processed and stored as datasets in a single database, from which new stellar tracks can be interpolated from.

4.2.1 Storing EEP tracks

The HDF5 database format is used for storing the datasets contained in the grid. As each stellar track file is processed, the stellar properties are recalculated at uniform time steps through each stellar phase so that there is an equivalent point for all stars which evolve through the same phases which can be used to interpolate between, i.e. the n th point in phase p in one track will be at the same elapsed time in units of the length of phase p as the n th point for another track. This is performed using the phases as defined by Flexible Stellar Population Synthesis (FSPS) which is stored as a column in each track file (see table 4.2), and by default linear interpolation is

¹Publicly available from http://waps.cfa.harvard.edu/MIST/model_grids.html

used to calculate the stellar properties at these points (which can have issues, as discussed in section 4.4).

Linear interpolation between two known points is simple. Given two points x_0, y_0 and x_1, y_1 , the value y at a point x between x_0 and x_1 is obtained by drawing a straight line between the two points – and essentially gives each known point a weight based on the inverse of their distance to the new point. Then, the value y can be found from:

$$y = m(x - x_0) + y_0, \quad (4.1)$$

where $m = (y_1 - y_0)/(x_1 - x_0)$. Linear interpolation was chosen because of its speed and the data in the stellar tracks are fairly closely spaced (although this would be trivial to change to use another method, such as cubic splines for smoother interpolants).

To reduce storage and computational requirements, unneeded stellar properties in the track files can be excluded from the database. A `Python` script can be run with different parameters to recreate a database with different property columns, and also produce `C++` class files containing the declaration and definition of the base star class and derived class for a star with a stellar track obtained using MIST, as well as methods for obtaining its properties, and evolving and obtaining the remnant mass of the star. A benefit of using the `HDF5` format is compression which can reduce the size of the file stored on the disk.

4.2.2 Interpolating between EEP tracks

Given a desired initial mass, m , and metallicity, $[Z/H] \equiv \log_{10} [(Z/X)/(Z_{\odot}/X_{\odot})]$, of a star, the code finds up to four neighbouring stellar tracks from the MIST grid which surround the desired point in mass-metallicity space. The metallicity of the stellar tracks in these files are scaled relative to the protosolar solar metallicity,

EEP	Phase
1	Pre-main sequence (PMS)
2	Zero-age main sequence (ZAMS)
3	Intermediate-age main sequence (IAMS)
4	Terminal-age main sequence (TAMS)
5	Red giant branch tip (RGBTip)
6	Zero-age core helium burning (ZACHeB)
7	Terminal-age core helium burning (TACHeB)
Low mass	
8	Thermally-pulsating asymptotic giant branch (TPAGB)
9	Post-aymptotic giant branch (PostAGB)
10	White dwarf cooling sequence (WDCS)
High mass	
8	Carbon burning (CB)

Table 4.1: Stellar phases included in the EEP track files for both low and high mass stars (Choi et al. 2016). The boundary between low and mass stars depends upon the stellar metallicity.

$Z_{\odot, \text{proto}} = 0.0142$ (Asplund et al. 2009), instead of the usually adopted value of $Z_{\odot} = 0.0134$. The absolute values of hydrogen and helium mass fraction from a given value of Z are calculated using (Choi et al. 2016):

$$Y = Y_p + \left(\frac{Y_{\odot, \text{proto}} - Y_p}{Z_{\odot, \text{proto}}} \right) Z, \quad (4.2)$$

$$X = 1 - Y - Z, \quad (4.3)$$

where $Y_p = 0.249$ is the primordial helium abundance (Planck Collaboration et al. 2016),

If either the desired mass or metallicity matches those of a set of grid points, then only the two surrounding points in the other dimension are found (e.g. if the grid contains points at the same metallicity as the desired star, then two neighbouring mass points of the grid will be selected). If the desired properties match a grid point exactly, then the stellar track of that grid point is used without any interpolation being required.

Number	FSPS phase	Data points
-1	Pre-main sequence (PMS)	201
0	Main sequence (MS)	252
2	Red giant branch (RGB)	151
3	Core helium burning (CHeB)	102
4	Extended asymptotic giant branch (EAGB)	101
5	Thermally-pulsating asymptotic giant branch (TPAGB)	601
6	Post-asymptotic giant branch (PAGB)	302
9	Wolf-Rayet star (WR)	450

Table 4.2: FSPS phases (Conroy, Gunn, and White 2009; Conroy and Gunn 2010) included in the EEP track files for each star which are used for interpolation, and the default number of points of data interpolated for each phase. Not all phases are explored by each star, e.g. low mass stars don't evolve to become WR stars.

Following selection of grid points, and assuming that the star doesn't match a grid point, the points are then compared to see if interpolation is possible. This requires each of the stellar tracks to contain the same stellar phases, so all points need to either be evolved as low mass or high mass stars (table 4.1) and also explore the same FSPS phases (table 4.2). If these requirements are met, then interpolation is performed between each of the grid points using a linear regime (i.e. bilinear for four grid points, interpolating in mass and metallicity). Bilinear interpolation is performed in two dimensions by linearly interpolating in each dimension once. Given the value of a function at four points $f(x_0, y_0)$, $f(x_1, y_0)$, $f(x_0, y_1)$ and $f(x_1, y_1)$, the value of the function at $f(x, y)$ bounded by these four points can be calculated. Linear interpolation (as before) can be performed along the x-axis first to yield:

$$f(x, y_0) = \frac{x_1 - x}{x_1 - x_0} f(x_0, y_0) + \frac{x - x_0}{x_1 - x_0} f(x_1, y_0), \quad (4.4)$$

$$f(x, y_1) = \frac{x_1 - x}{x_1 - x_0} f(x_0, y_1) + \frac{x - x_0}{x_1 - x_0} f(x_1, y_1). \quad (4.5)$$

Then linear interpolation is applied between these two points to obtain the estimate of $f(x, y)$:

$$f(x, y) = \frac{y_1 - y}{y_1 - y_0} f(x, y_0) + \frac{y - y_0}{y_1 - y_0} f(x, y_1). \quad (4.6)$$

If interpolation is unable to be performed between the stellar tracks due to containing different phases, a fallback routine is used. In this case, each surrounding point on the grid is given a weight based on the inverse of the distance to the desired point, and a stellar track is picked at random using these weights. The nearest point is therefore has the highest probability at being picked but other points aren't entirely excluded, as the boundary between exploring the different stellar phases isn't precisely known. In practice $\lesssim 2\%$ of stellar tracks were obtained using this method when generating initial masses using a Kroupa initial mass function (IMF) (but can vary depending on choice of metallicity and mass range). The weights were simply calculated as:

$$w_{\text{mass},i} = \frac{1}{|m - m_i|}, \quad (4.7)$$

$$w_{\text{metal},i} = \frac{1}{|M - M_i|}, \quad (4.8)$$

where m and $M = [Z/H]$ are the initial mass and relative abundance (compared to the sun) of metal of the desired star and m_i and M_i the mass and relative abundance of grid point i . In the case of four surrounding grid points, the mass and metallicity were randomly calculated independently from each other to avoid the requirement of normalisation in each dimension to compare them.

Currently there are two versions of the interpolator. The first version reads in the grid data into RAM to speed up the interpolation, whilst the second version reads in the datasets of only the surrounding grid points just prior to interpolation of each star. There are benefits and disadvantages to each version, and the computational time required by each depends on the number of grid points in the grid and the number of columns of stellar properties stored in each. In the default setup containing all stars from the packaged model grids and 16 of the 77 stellar property columns, the MIST database requires ~ 350 MB of RAM and takes $\sim 10 - 15s$ to read from a mechanical hard drive. However, once this database is stored in RAM this results

in a $\sim 2\times$ speed-up in interpolation on the same device (table 4.3), providing that there is sufficient memory available on the system. For a small number of stars the uncached interpolator is recommended, otherwise for generating the stellar tracks of many stars the cached version will be faster – providing that the amount of memory required by the grid is free.

Interpolation	Uncached	Cached
Linear	22s	10s
Bilinear	45s	23s

Table 4.3: Running benchmarks to compare the time taken to interpolate 10,000 stellar tracks using the cached and uncached version of the interpolator for the default MIST grid settings (all stars in the packaged model grid 0.1 - 300.0 M_{\odot} from $-4.0 \leq [Z/H] \leq 0.5$, and 16 stellar property columns). Note that reading in the MIST grid into RAM requires additional time. The fallback routine of randomly picking a neighbouring point was used in $\sim 1.5\%$ of cases.

4.2.3 Evolving a star

A stellar evolutionary track has now been produced for the desired stellar properties; either by interpolation or using an exact grid point from matching the desired properties or through the secondary routine. Linear interpolation is again used to be able to find the stellar properties at any desired age of the star until the end of the track, either through setting the age directly or evolving the star along the track.

Whilst not contained in the stellar tracks, remnant masses can be calculated using various prescriptions from the final stellar properties of the high mass stars that have finished carbon burning (CB). The default supernova engine for calculating the remnant masses of high mass stars ($\gtrsim 8.0 M_{\odot}$, Doherty et al. (2015)) is through using the delayed supernova mechanism presented in Fryer et al. (2012) (although the code is modular, and additional models can be added). This model only requires knowledge of the mass of the star, M , and the carbon-oxygen (CO) core mass,

M_{CO} , just prior to the supernova explosion, and involves calculating the proto-compact object mass and the amount of fallback material which is accreted back onto the proto-compact object during the explosion. The proto-compact object mass is calculated as (Fryer et al. 2012):

$$M_{\text{proto}} = \begin{cases} 1.2 M_{\odot}, & \text{for } M_{\text{CO}} < 3.5 M_{\odot} \\ 1.3 M_{\odot}, & \text{for } 3.5 M_{\odot} \leq M_{\text{CO}} < 6.0 M_{\odot} \\ 1.4 M_{\odot}, & \text{for } 6.0 M_{\odot} \leq M_{\text{CO}} < 11.0 M_{\odot} \\ 1.6 M_{\odot}, & \text{for } M_{\text{CO}} \geq 11.0 M_{\odot}. \end{cases} \quad (4.9)$$

The fallback mass is calculating assuming that the more massive cores experience a larger delay before the supernova, meaning that a larger fraction of mass is accreted back onto the proto-compact object. The fallback mass or fraction is calculated as (ibid.):

$$\begin{cases} M_{\text{fb}} = 0.2 M_{\odot}, & \text{for } M_{\text{CO}} < 2.5 M_{\odot} \\ M_{\text{fb}} = 0.5 M_{\text{CO}} - 1.05 M_{\odot}, & \text{for } 2.5 M_{\odot} \leq M_{\text{CO}} < 3.5 M_{\odot} \\ f_{\text{fb}} = a M_{\text{CO}} + b, & \text{for } 3.5 M_{\odot} \leq M_{\text{CO}} < 11.0 M_{\odot} \\ f_{\text{fb}} = 1.0, & \text{for } M_{\text{CO}} \geq 11.0 M_{\odot}, \end{cases} \quad (4.10)$$

where $a = 0.133 - (0.093/M - M_{\text{proto}})$, $b = -11a + 1$ and $M_{\text{fb}} = f_{\text{fb}}(M - M_{\text{proto}})$.

The baryonic remnant mass is then just the sum of the proto-compact object mass and the fallback mass, $M_{\text{rem,bar}} = M_{\text{proto}} + M_{\text{fb}}$ (ibid.). The baryonic remnant mass is then converted to the gravitational remnant mass using:

$$\begin{cases} M_{\text{rem}} = 0.9 M_{\text{rem,bar}}, & \text{for BHs (ibid.)} \\ M_{\text{rem}}^2 + M_{\text{rem}} - M_{\text{rem,bar}} = 0, & \text{for NS's (ibid.),} \end{cases} \quad (4.11)$$

with the baryonic remnant mass boundary between neutron stars and black holes set as an adjustable parameter. The latter equation for calculating the neutron star remnant mass is solved using the quadratic formula.

4.2.4 Obtaining the mass distribution of a cluster

Given a metallicity, a cluster of stars can be produced using an IMF to generate their zero-age main sequence (ZAMS) masses. Assuming that each star then evolves as an isolated object (which is physically unrealistic in a real cluster, with the majority of stars in a binary and with most stars living for $>$ Gyrs, dynamical interactions with other stars in the cluster are likely), the interpolator can be used to obtain their stellar properties over time. Using a supernova engine such as the delayed supernova (SN) engine mentioned above in section 4.2.3, the mass distribution of BHs and NS's can be obtained. For this project, the Kroupa IMF is chosen to generate the initial cluster of stars (Kroupa 2001), where $p(m) \propto m^{-\alpha}$, with α as:

$$\alpha = \begin{cases} 0.3, & \text{for } m < 0.08 M_{\odot} \\ 1.3, & \text{for } 0.08 \leq m \leq 0.5 M_{\odot} \\ 2.3, & \text{for } m > 0.5 M_{\odot}. \end{cases} \quad (4.12)$$

Clusters of 5×10^5 stars are generated in a Monte Carlo (MC) simulation with stellar masses ranging from 8.0 - 100.0 M_{\odot} at different metallicities for each cluster using the MIST interpolator and then evolved into remnants using the delayed SN engine from Fryer et al. (2012). The massive stars $\gtrsim 8 M_{\odot}$ also have much shorter lives with main sequence lifetime on the order of tens of Myr or less, so dynamical interactions become less important. These clusters are then compared to equivalent clusters produced using the COMPAS population synthesis code (Stevenson et al.

2017), where stars are evolved using SSE (Hurley et al. 2000)² and the same SN engine is used to calculate the remnant masses. Comparisons will be drawn on the distribution of masses at the end of the lives of the stars, and their remnants, at two metallicities of $Z = 0.02$ and $Z = 0.005$ (slightly higher than solar and below solar metallicities). The upper mass limit is the current limit of evolving single stars in COMPAS using SSE, which already extrapolates for stellar masses $> 50 M_{\odot}$. One key discrepancy between the two stellar evolution methods is the difference in stellar rotation. Evolving stars in COMPAS consider all stars to be non-rotating. Currently MIST provides two sets of stellar EEP tracks, for both non-rotating and for stellar rotations of $v/v_{\text{crit}} = 0.4$, 40% of the critical break-up speed. However, there appears to be large issues in the non-rotating models of MIST where certain tracks contain only the pre-main sequence (MS) evolution of the star, so interpolation and calculation of remnant masses is not currently possible. This means that the tracks containing the evolution of rotating stars are used to generate the cluster of stars in MIST, which will likely have some effects on the stellar properties such as the stellar radius that aren't present in the COMPAS cluster. A more reliable comparison will likely be able to be performed in the future once this issue is rectified.

4.3 Results

Contained in this section are some plots of the stellar properties obtained using the MIST interpolator. Also present are plots comparing the fate of high-mass ($\gtrsim 8.0 M_{\odot}$) stars in terms of NS and BH masses and the properties at the time of the SN.

²with extrapolations of the fitting formulae used for stars $m > 50 M_{\odot}$

4.3.1 Stellar radius through each phase

figure 4.1 shows the stellar radius at the start of each FSPS phase for two different metallicities; solar and at a low metallicity of 0.01% of solar. The boundary between low and high mass at solar metallicity can be seen by looking at the final radius where a sharp cutoff occurs at $\sim 8M_{\odot}$. The stellar tracks for the low metallicity stars finish at the end of core helium burning (CHeB), meaning that there is no WDCS shown. Knowing the stellar radius during the life of a star is important for binary evolution when considering mass transfer through Roche-lobe overflow (RLOF) and common envelope phases, and potential mass loss and collisions with other objects such as in dense nuclear clusters.

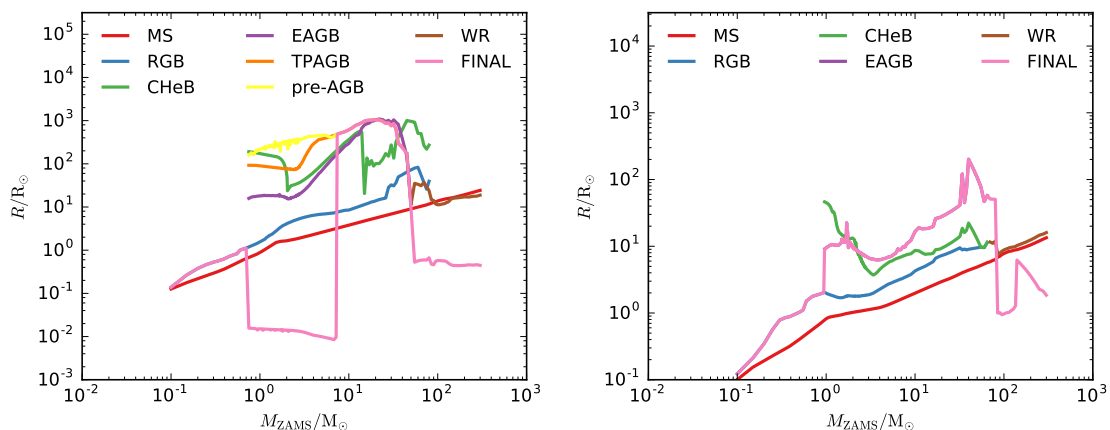


Figure 4.1: The radius of stars at the beginning of each FSPS phase (see table 4.2) calculated at solar metallicity (left) and 0.01% solar metallicity (right). The lower metallicity stellar tracks can be seen to end at CHeB.

4.3.2 Stellar evolution on the MIST grid

Plots of the final masses of the stars and their remnants were produced along for the entire range of masses and metallicities available for MIST and SSE, the latter using COMPAS and extrapolated fits up to $100M_{\odot}$. It should be noted that the full evolution tracks are not provided for $[Z/H] < 2.0$ in MIST, so the results of stars in this region should be taken with a (large) grain of salt and so are not shown in

these results.

The final mass of stars for MIST and SSE at the end of the stellar tracks are shown in figure 4.2, along with the equivalent plot for SSE shown for the same range and normalised to the same colours. There is a similar trend in final masses between MIST and SSE where the final masses of stars generally increases for lower metallicity and higher masses, but there is also an additional peak in both cases in different locations. The highest final masses occur at $\sim 70 - 80 M_{\odot}$ and $[Z/H] \sim -0.9 - -1.0$ for MIST stars, and is higher than the peak for SSE stars. There is a minor peak in the final masses of SSE stars at $\sim 30 M_{\odot}$ at $[Z/H] \lesssim -1.0$. The contours are much less smooth for the MIST stars, this is due to the interpolation failing for stars at these points and instead a random neighbouring stellar track is used.

The CO core masses for both MIST and SSE are found in figure 4.3. SSE displays the same trend as for the final masses, albeit this time without the secondary minor peak. Interestingly, the some of the MIST stars within the peak of the final masses display no CO in the core, which may be due to errors during evolution of the star when evolved using MESA (as the original EEP files display the same result without interpolation). MIST again produces stars with the largest CO core masses, but there are regions at the lower metallicity range and the highest stellar masses where SSE star CO core masses are larger.

Finally, the remnant masses produced using the delayed SN mechanism (Fryer et al. 2012) are displayed in figure 4.4. The lack of CO core masses in some MIST stars severely restricts the fallback fraction, meaning that they result in the minimum $\sim 1.27 M_{\odot}$ NS being produced from the delayed SN remnant model (which is likely due to an issue in MESA evolution rather than for physical reasons). The higher final masses coupled with the slightly higher CO core masses near the peak for the MIST stars results in the potential for more massive BH, and the secondary peak

at $\sim 30 M_{\odot}$ appears again at low metallicity for SSE stars. For some metallicities, this will result in fewer BH being produced from an IMF in place of a NS using the delayed SN mechanism, but won't have an effect at the two metallicities tested in this work.

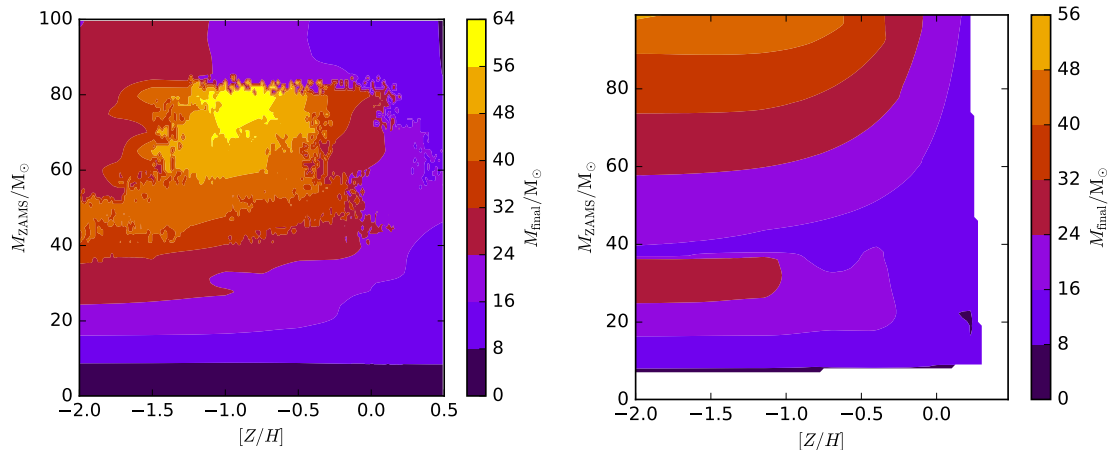


Figure 4.2: Final stellar masses for stars evolved using MIST interpolation (left) and using SSE via COMPAS (right). MIST evolves stars until the end of the HB, the WDCS or CB phases depending on the initial stellar properties in the shown range of metallicity.

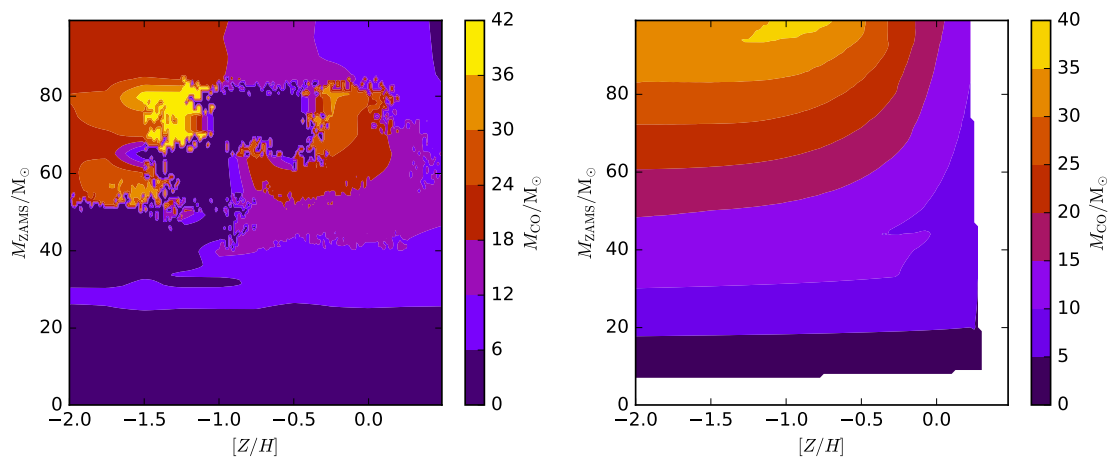


Figure 4.3: The final mass of the CO core for MIST stars (left) and SSE stars via COMPAS (right). MIST evolves stars until the end of the HB, the WDCS or CB phases depending on the initial stellar properties in the shown range of metallicity.

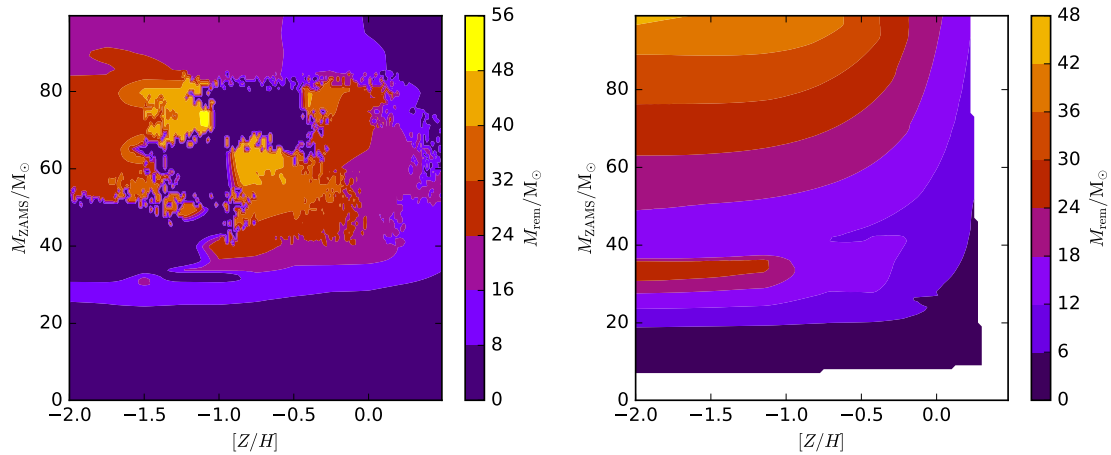


Figure 4.4: Remnant masses of MIST stars (left) and SSE stars via COMPAS (right) using the same delayed SN mechanism from Fryer et al. (2012) (except for SSE stars $\lesssim 8 M_{\odot}$, which evolve via **ECSN!**).

4.3.3 Mass distributions using MIST versus SSE

Shown here are plots of the initial and various final mass distributions of the stellar clusters generated using both the MIST interpolator and SSE vis COMPAS. When the final mass of a star is mentioned, this is referring to the pre-SN mass used to calculate the fallback mass as part of the overall remnant mass in the delayed SN engine.

Cluster at $Z=0.02$

Two clusters consisting of 500,000 high mass stars at $Z = 0.02$, slightly above solar metallicity, are produced using both MIST and SSE to calculate their stellar evolution. The initial and final mass distributions of stars are shown in figure 4.5. Starting from the same initial distribution, there is a noticeable difference in the remnant mass distribution between the two stellar evolution models. The remnant mass depends on the final stellar mass and the CO core mass just prior to the supernova. A clearer comparison of the final stellar mass distribution between the two models is plotted in the left panel of figure 4.5. Here, whilst the peak of both distributions are similar with final masses $\sim 8 - 13 M_{\odot}$, there are a significant

number of stars from the COMPAS cluster which have final masses $\lesssim 5 M_{\odot}$, and in contrast an even greater number of MIST stars at higher final masses $\gtrsim 16 M_{\odot}$. The distribution of CO core masses in the right panel of the same figure are similar, but there are fewer MIST stars with CO core masses at $\sim 6 - 9 M_{\odot}$ whilst containing an excess at $\gtrsim 10 M_{\odot}$ which extends past the upper limit of COMPAS. A comparison of the remnant masses is shown in figure 4.7. A low remnant masses $\lesssim 10 M_{\odot}$ the difference in distributions mostly reflect that of the difference in the CO core masses, but above $\gtrsim 14 M_{\odot}$ the difference is much greater. This is because the fallback mass fraction is relatively small at low CO core masses, but becomes large for more massive final CO masses (which also corresponds to more massive stars, increasing the fallback mass further) and therefore has an increasing influence on the remnant mass. This means that the distribution of NS's obtained are similar in MIST and COMPAS, but MIST stars tend to produce more massive BHs.

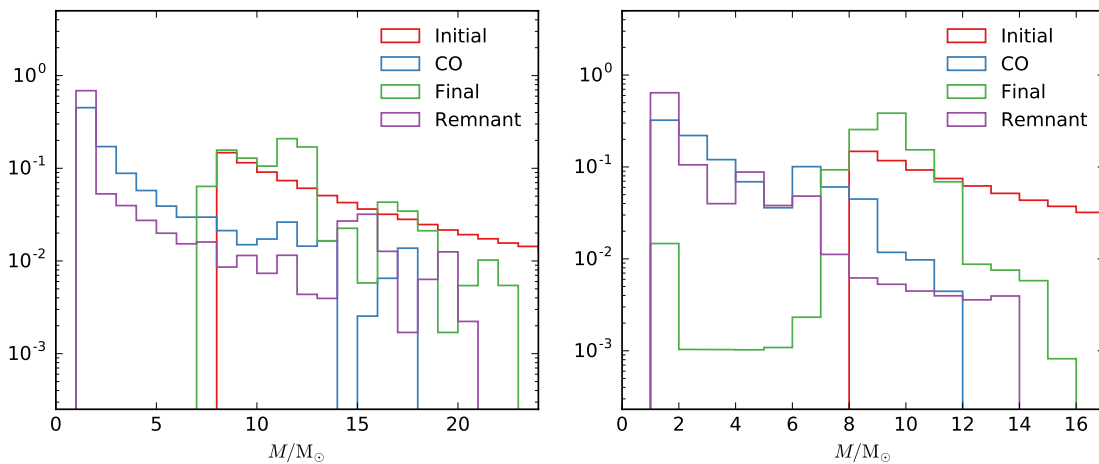


Figure 4.5: The initial and various final normalised mass distributions of a cluster of $8.0 - 100.0 M_{\odot}$ stars at $Z = 0.02$ produced by interpolating MIST models (left) and using SSE (right).

Cluster at $Z=0.005$

The mass distributions generated from the MIST grid contain gaps in them, partially due to the the fallback routine used during interpolation, where one of the nearest

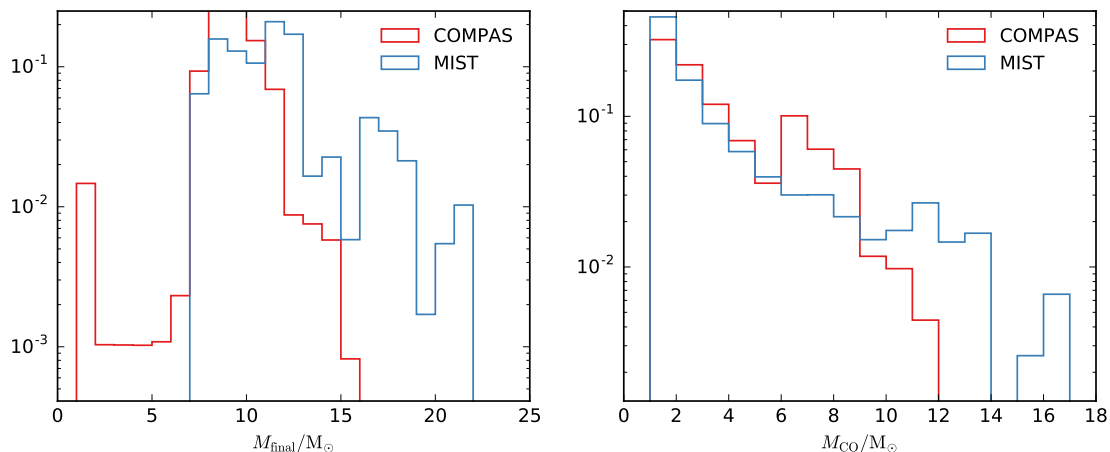


Figure 4.6: Comparison of the final (left) and CO core (right) mass distributions between interpolating from MIST and SSE for a cluster of stars at $Z = 0.02$.

four neighbouring grid points are chosen at random without any interpolation being formed. Figure 4.8 shows the same initial and final mass distributions as shown for $Z = 0.02$, with the gaps appearing at the higher end of masses. From figure 4.3, these can be seen to result from the stars at around $\sim 50 - 75 M_{\odot}$, which actually produce the largest remnant masses at this metallicity. It is likely that the distribution of final, CO core and remnant masses should be more continuous as shown in the right panel of figure 4.8 for the COMPAS stars. Although again it is observed that a number of COMPAS stars end with small final masses. When comparing the final and CO core masses more closely in figure 4.8, the distributions are reasonably similar – especially if the likely unphysical gaps in the MIST distribution are made continuous. Then, the only additional difference is the small number of MIST stars which reach a final mass close to $\sim 50 M_{\odot}$. As expected from these two distributions, the remnant mass distributions (figure 4.9) are alike (if again the gaps in the MIST distribution are “smoothed” into a continuous shape). The MIST stars produce slightly higher mass BHs at the expense of moderate masses, with essentially the same NS distribution.

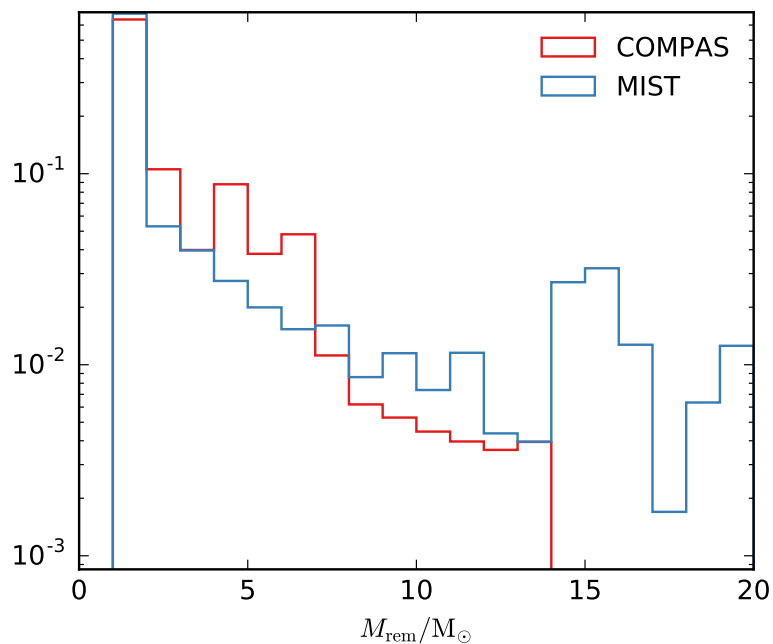


Figure 4.7: A comparison of the remnant mass distributions between interpolating from MIST and SSE for high mass stars with $Z = 0.02$.

4.4 Discussion

The interpolator can interpolate using the MIST grid to rapidly obtain stellar evolutionary tracks for stars over a large range in mass and metallicities. NS and BH remnant masses can be calculated for $-2.0 \leq [Z/H] \leq 0.5$, with stellar tracks of stars at lower metallicities not evolved sufficiently by MIST. Additionally, high mass stars $\gtrsim 100 M_{\odot}$ need to be more carefully considered, particularly at low metallicities. Stellar pulsations can result in mass loss in stars $\sim 100 - 140 M_{\odot}$ at $Z \lesssim 10^{-3} - 10^{-4}$ (Heger et al. 2003), and pair-instability SN can disrupt massive stars in the range $\sim 140 - 260 M_{\odot}$ to leave behind no remnant at all. It may even be possible for high mass stars to experience a pair-instability SN at higher metallicities where sufficient surface magnetic fields prevent mass loss and increase the mass of the CO core (Georgy et al. 2017).

The interpolation of each stellar track at equivalent points over each stellar phase could be improved. Currently, linear interpolation is performed over each stellar

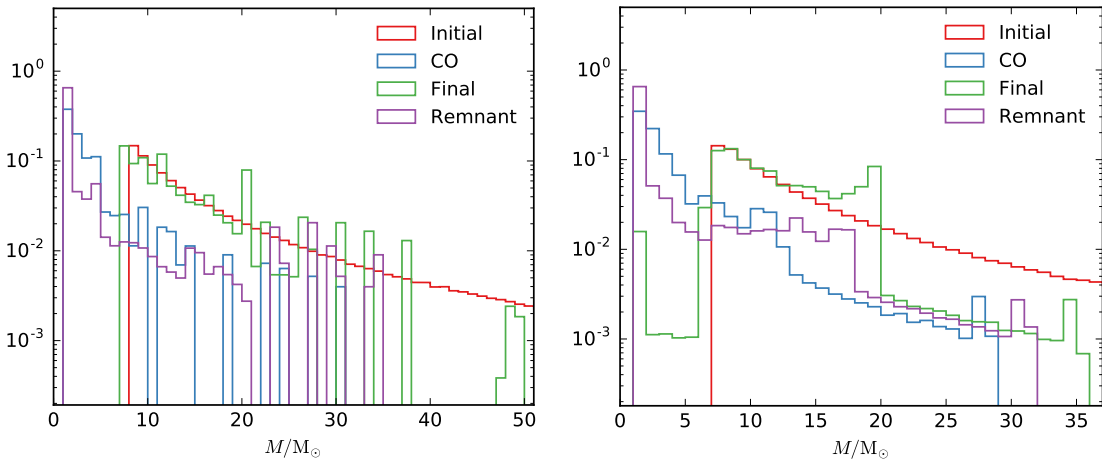


Figure 4.8: The initial and various final normalised mass distributions of a cluster of $8.0 - 100.0 M_{\odot}$ stars at $Z = 0.005$ produced by interpolating MIST models (left) and using SSE (right).

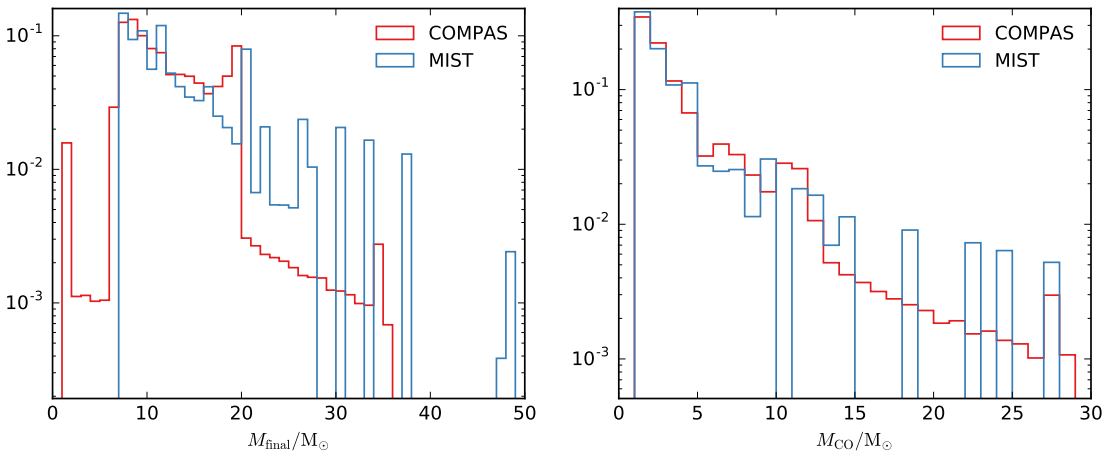


Figure 4.9: Comparison of the final (left) and CO core (right) mass distributions between interpolating from MIST and SSE for a cluster of stars at $Z = 0.005$.

property with the same number of points as the original unevenly-sampled points in the provided stellar tracks, potentially resulting in large errors in places where changes in properties are non-linear. This error can be reduced by increasing the overall number of points provided in the grid in each phase, or use another interpolation method such as a set of cubic splines (or even the Akima spline which is more stable by suppressing oscillations from “outliers”). Using a piecewise interpolation method should reduce the need to increase the number of points to control the errors, keeping the size of the grid small enough and avoiding an increase in

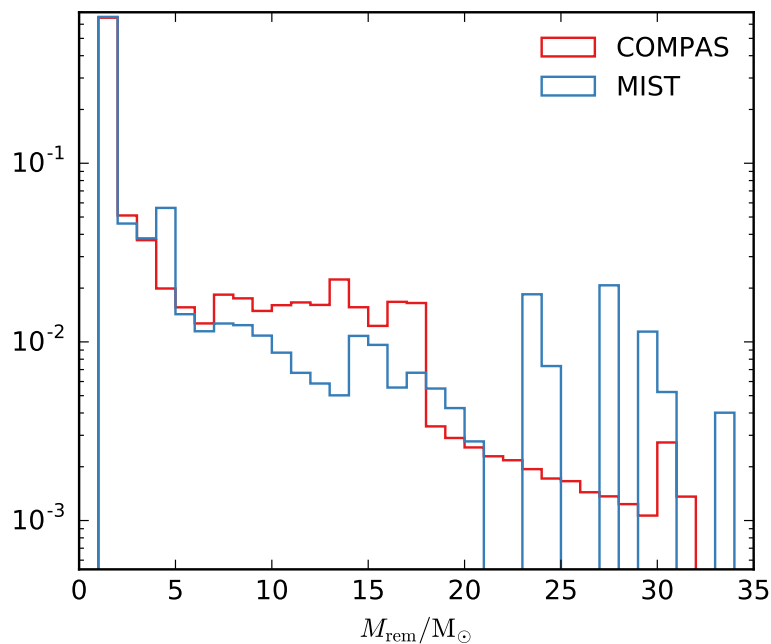


Figure 4.10: A comparison of the remnant mass distributions between interpolating from MIST and SSE for high mass stars with $Z = 0.005$.

interpolation time. The same method can also be applied to the interpolation performed between stellar tracks without dramatically affecting computational time, but more investigation is required so that unphysical artifacts from the interpolation are prevented.

The secondary routine of choosing a random grid point when interpolation fails could also be improved. Currently, there is potential for a star which undergoes evolution as a high-mass star which has a lower mass than a star which is evolved as a low-mass star. A potential partial solution to this is to investigate the boundary between the two in MESA and provide stellar tracks at masses just above and below this boundary mass. Then when evolving stars of a given metallicity, a clear boundary is defined and the mass distribution should appear more continuous. However, this would not solve the case for picking stars at metallicities where the boundary of high and low mass stars are in significantly different locations, although it may reduce the fraction of stars being evolved this way.

Whilst the current method for determining the final remnant mass of massive stars

is the delayed mechanism in Fryer et al. (2012), there are still uncertainties surrounding the formation of compact remnants and their properties. The next stage, as previously mentioned, is incorporation of this code into COMPAS. This adds the option of evolving stars using MIST alongside using SSE for both single and binary evolution, and the COMPAS code already includes various prescriptions for modelling the post-SN remnants produced from high-mass stars. In addition, stars evolved using interpolation through MIST can then be tested against observations, and can be used to increase our understanding of binary evolution (Stevenson et al. 2017).

References

- [1] M. Asplund et al. “The Chemical Composition of the Sun”. In: *ARA&A* 47 (Sept. 2009), pp. 481–522. DOI: 10.1146/annurev.astro.46.060407.145222. arXiv: 0909.0948 [astro-ph.SR].
- [2] J. Choi et al. “Mesa Isochrones and Stellar Tracks (MIST). I. Solar-scaled Models”. In: *ApJ* 823, 102 (June 2016), p. 102. DOI: 10.3847/0004-637X/823/2/102. arXiv: 1604.08592 [astro-ph.SR].
- [3] C. Conroy and J. E. Gunn. “The Propagation of Uncertainties in Stellar Population Synthesis Modeling. III. Model Calibration, Comparison, and Evaluation”. In: *ApJ* 712 (Apr. 2010), pp. 833–857. DOI: 10.1088/0004-637X/712/2/833. arXiv: 0911.3151.
- [4] C. Conroy, J. E. Gunn, and M. White. “The Propagation of Uncertainties in Stellar Population Synthesis Modeling. I. The Relevance of Uncertain Aspects of Stellar Evolution and the Initial Mass Function to the Derived Physical Properties of Galaxies”. In: *ApJ* 699 (July 2009), pp. 486–506. DOI: 10.1088/0004-637X/699/1/486. arXiv: 0809.4261.
- [5] C. L. Doherty et al. “Super- and massive AGB stars - IV. Final fates - initial-to-final mass relation”. In: *MNRAS* 446 (Jan. 2015), pp. 2599–2612. DOI: 10.1093/mnras/stu2180. arXiv: 1410.5431 [astro-ph.SR].

- [6] A. Dotter. “MESA Isochrones and Stellar Tracks (MIST) 0: Methods for the Construction of Stellar Isochrones”. In: *ApJS* 222, 8 (Jan. 2016), p. 8. DOI: 10.3847/0067-0049/222/1/8. arXiv: 1601.05144 [astro-ph.SR].
- [7] C. L. Fryer et al. “Compact Remnant Mass Function: Dependence on the Explosion Mechanism and Metallicity”. In: *ApJ* 749, 91 (Apr. 2012), p. 91. DOI: 10.1088/0004-637X/749/1/91. arXiv: 1110.1726 [astro-ph.SR].
- [8] C. Georgy et al. “Possible pair-instability supernovae at solar metallicity from magnetic stellar progenitors”. In: *A&A* 599, L5 (Mar. 2017), p. L5. DOI: 10.1051/0004-6361/201730401. arXiv: 1702.02340 [astro-ph.SR].
- [9] A. Heger et al. “How Massive Single Stars End Their Life”. In: *ApJ* 591 (July 2003), pp. 288–300. DOI: 10.1086/375341. eprint: astro-ph/0212469.
- [10] J. R. Hurley, O. R. Pols, and C. A. Tout. “Comprehensive analytic formulae for stellar evolution as a function of mass and metallicity”. In: *MNRAS* 315 (July 2000), pp. 543–569. DOI: 10.1046/j.1365-8711.2000.03426.x. eprint: astro-ph/0001295.
- [11] P. Kroupa. “On the variation of the initial mass function”. In: *MNRAS* 322 (Apr. 2001), pp. 231–246. DOI: 10.1046/j.1365-8711.2001.04022.x. eprint: astro-ph/0009005.
- [12] B. Paxton, L. Bildsten, et al. “Modules for Experiments in Stellar Astrophysics (MESA)”. In: *ApJS* 192, 3 (Jan. 2011), p. 3. DOI: 10.1088/0067-0049/192/1/3. arXiv: 1009.1622 [astro-ph.SR].
- [13] B. Paxton, M. Cantiello, et al. “Modules for Experiments in Stellar Astrophysics (MESA): Planets, Oscillations, Rotation, and Massive Stars”. In: *ApJS* 208, 4 (Sept. 2013), p. 4. DOI: 10.1088/0067-0049/208/1/4. arXiv: 1301.0319 [astro-ph.SR].

-
- [14] B. Paxton, P. Marchant, et al. “Modules for Experiments in Stellar Astrophysics (MESA): Binaries, Pulsations, and Explosions”. In: *ApJS* 220, 15 (Sept. 2015), p. 15. DOI: 10.1088/0067-0049/220/1/15. arXiv: 1506.03146 [astro-ph.SR].
- [15] Planck Collaboration et al. “Planck 2015 results. XIII. Cosmological parameters”. In: *A&A* 594, A13 (Sept. 2016), A13. DOI: 10.1051/0004-6361/201525830. arXiv: 1502.01589.
- [16] S. Stevenson et al. “Formation of the first three gravitational-wave observations through isolated binary evolution”. In: *Nature Communications* 8, 14906 (Apr. 2017), p. 14906. DOI: 10.1038/ncomms14906. arXiv: 1704.01352 [astro-ph.HE].
- [17] F. X. Timmes, S. E. Woosley, and T. A. Weaver. “The Neutron Star and Black Hole Initial Mass Function”. In: *ApJ* 457 (Feb. 1996), p. 834. DOI: 10.1086/176778. eprint: astro-ph/9510136.

Appendix A

Appendix

A.1 Converting between orbital elements and state vectors

These equations are used to convert between state vectors and orbital elements assuming a dominant central Keplerian potential.

A.1.1 State vectors to orbital elements

Orbital elements of a body in a Keplerian orbit in the xy plane can be obtained from its state vectors, position \vec{r} and velocity \vec{v} . The sum of the kinetic and potential energy of two bodies orbiting divided by the reduced mass $\mu = m_1 m_2 / (m_1 + m_2)$ is known as the specific energy, where m_1 and m_2 are the masses of the two bodies. The specific energy is therefore written as:

$$\varepsilon = \frac{v^2}{2} - \frac{GM}{r}, \quad (\text{A.1})$$

where $v = |\vec{v}|$ is the relative orbital speed between the two bodies, G is the gravitational constant, $M = m_1 + m_2$ is the total mass and $r = |\vec{r}|$ is the distance between the two bodies. The semimajor axis, a , can be obtained by rearranging the vis-viva equation:

$$\frac{v^2}{2} - \frac{GM}{r} = \frac{GM}{2a}. \quad (\text{A.2})$$

The eccentricity is the magnitude of the eccentricity, a vector pointing from the apoapsis to the periapsis:

$$e = |\vec{e}| = \left| \frac{\vec{v} \times \vec{h}}{GM} - \frac{\vec{r}}{r} \right|, \quad (\text{A.3})$$

where $\vec{h} = \vec{r} \times m\vec{v}$ is the angular momentum vector.

The argument of periapsis can be found from the ascending node $\vec{n} = \vec{k} \times \vec{h}$, where $\vec{k} = [0, 0, 1]$ is the unit vector normal to the plane of the orbit, and eccentricity

vectors:

$$\omega = \begin{cases} \cos^{-1} \frac{\langle \vec{n}, \vec{e} \rangle}{|\vec{n}| |\vec{e}|} & \text{for } e_z \geq 0 \\ 2\pi - \cos^{-1} \frac{\langle \vec{n}, \vec{e} \rangle}{|\vec{n}| |\vec{e}|} & \text{for } e_z < 0. \end{cases} \quad (\text{A.4})$$

The longitude of the ascending node is found solely from the ascending node vector:

$$\Omega = \begin{cases} \cos^{-1} \frac{n_x}{|\vec{n}|} & \text{for } n_y \geq 0 \\ 2\pi - \cos^{-1} \frac{n_x}{|\vec{n}|} & \text{for } n_y < 0. \end{cases} \quad (\text{A.5})$$

The true anomaly is from the eccentricity and position vectors:

$$\nu = \begin{cases} \cos^{-1} \frac{\langle \vec{e}, \vec{r} \rangle}{|\vec{e}| |\vec{r}|} & \text{for } \langle \vec{r}, \vec{v} \rangle \geq 0 \\ 2\pi - \cos^{-1} \frac{\langle \vec{e}, \vec{r} \rangle}{|\vec{e}| |\vec{r}|} & \text{otherwise.} \end{cases} \quad (\text{A.6})$$

The eccentric anomaly requires the true anomaly and the eccentricity:

$$E = 2 \tan^{-1} \frac{\tan \frac{\nu}{2}}{\sqrt{\frac{1+e}{1-e}}}. \quad (\text{A.7})$$

The inclination of obtained from the orbital momentum vector:

$$i = \cos^{-1} \frac{h_z}{|\vec{h}|}. \quad (\text{A.8})$$

Finally, the mean anomaly is found from the eccentric anomaly and eccentricity:

$$M = E - e \sin E. \quad (\text{A.9})$$

A.1.2 Orbital elements to state vectors

The radial position is calculated from the general equation of a conic (Murray and Dermott 1999):

$$r = \frac{p}{1 + e \cos \nu}, \quad (\text{A.10})$$

where $p = h^2/GM$ is the semilatus rectum, with $p = a(1 - e^2)$ for an elliptical orbit and $p = 2r_{\text{per}}$ in the case of a parabolic orbit. The true anomaly can be calculated from (ibid.):

$$\tan \frac{\nu}{2} = \sqrt{\frac{1+e}{1-e}} \tan \frac{E}{2}, \quad (\text{A.11})$$

and the eccentric anomaly can be found from the equation $M = E - e \sin E$ (ibid.) using a Newton-Raphson method to find the root where $f(E) = E - e \sin E - M = 0$, where $E_{i+1} = E_i - f(E_i)/f'(E_i)$ where $f'(E) = df(E)/dE$. The initial guess for the first value of the eccentric anomaly is obtained from Danby (1988):

$$E_0 = M + \text{sign}(\sin M)ke, \quad (\text{A.12})$$

with $k = 0.85$ as recommended and $\text{sign}(x) = |x|/x$ is the signum function for x . The x and y components of the radial position in Cartesian coordinates are then just:

$$x = r \cos \nu, \quad (\text{A.13})$$

$$y = r \sin \nu. \quad (\text{A.14})$$

The orbital velocity can be obtained from differentiating Equation A.10 with time,

yielding:

$$v = \frac{dr}{dt} = \frac{dr}{d\nu} \frac{d\nu}{dt}, \quad (\text{A.15})$$

$$= -\frac{p}{(1 + e \cos \nu)^2} \times -e \sin \nu \times \dot{\nu}, \quad (\text{A.16})$$

$$= \frac{pe\dot{\nu} \sin \nu}{(1 + e \cos \nu)^2}, \quad (\text{A.17})$$

$$= \frac{re\dot{\nu} \sin \nu}{1 + e \cos \nu}. \quad (\text{A.18})$$

The x and y components of the velocity can be obtained from differentiation of Equations A.13 and A.14:

$$v_x = \dot{r} \cos \nu - r\dot{\nu} \sin \nu, \quad (\text{A.19})$$

$$v_y = \dot{r} \sin \nu + r\dot{\nu} \cos \nu. \quad (\text{A.20})$$

Equation A.18 can be used to find an expression for \dot{r} and $\dot{\nu}$. The angular momentum $h = \sqrt{GMp} = \sqrt{GMa(1 - e^2)} = na^2\sqrt{1 - e^2}$, where n is the mean motion $2\pi/P_{\text{orb}}$, can also be written as $h = |\vec{r} \times \dot{\vec{r}}| = r^2\dot{\nu}$ with $\dot{\vec{r}} = \dot{r}\hat{r} + r\dot{\theta}\hat{\theta}$ in polar coordinates (as the change in the angle over time $\dot{\theta} = \dot{\nu}$). Rearranging for \dot{r} , this yields:

$$\dot{r} = \frac{na^2\sqrt{1 - e^2}}{r^2}. \quad (\text{A.21})$$

Substituting this into Equation A.18 obtains the expression for $\dot{\nu}$:

$$\dot{r} = \frac{na^2\sqrt{1 - e^2}}{r(1 + e \cos \nu)} e \sin \nu, \quad (\text{A.22})$$

$$= \frac{na}{\sqrt{1 - e^2}} e \sin \nu. \quad (\text{A.23})$$

An expression for $r\dot{\nu}$ can be obtained from rearranging Equation A.18 and substi-

tuting in Equation A.23:

$$\dot{\nu} = \frac{\dot{r}(1 + e \cos \nu)}{r e \sin \nu}, \quad (\text{A.24})$$

$$r\dot{\nu} = \frac{na}{\sqrt{1 - e^2}}(1 + e \cos \nu). \quad (\text{A.25})$$

Finally, these are substituted into Equations A.19 and A.19, simplifying them to:

$$v_x = \frac{na}{\sqrt{1 - e^2}} (e \sin \nu \cos \nu - (\sin \nu + e \sin \nu \cos \nu)), \quad (\text{A.26})$$

$$= -\frac{na}{\sqrt{1 - e^2}} \sin \nu. \quad (\text{A.27})$$

$$v_y = \frac{na}{\sqrt{1 - e^2}} (e \sin \nu^2 + \cos \nu + e \cos \nu^2), \quad (\text{A.28})$$

$$= \frac{na}{\sqrt{1 - e^2}} (\cos \nu + e). \quad (\text{A.29})$$

A.2 Inverse transform sampling

Generating random numbers based on different distributions was performed using the inverse transform method. Samples from a probability function $p(x)$ can be generated through the use of its cumulative distribution function (CDF), $F(x)$, which is an non-decreasing monotonic function. The inverse of the CDF, $F^{-1}(y)$, is defined as:

$$F^{-1}(y) = \inf\{x|F(x) \geq y\}, \quad y \in [0, 1], \quad (\text{A.30})$$

where \inf is the infimum of the CDF. Then a random variable u can be generated from $u = F^{-1}(U)$, where $U = \text{uniform}(0, 1)$, to be distributed as F with $p(u \leq x) = F(x)$. In practice, this means solving $F(F^{-1}(U)) = U$ for $u = F^{-1}(U)$.

A.2.1 Mutual inclination of the MBH-binary

The mutual inclination between the inner and outer binary in chapter 3 are randomly orientated, such that $p(i) = A \sin i$, with A normalising the sum of probabilities such that $\int_0^\pi p(i) di = 1$, where $A = 1/2$. The CDF can be therefore written as:

$$F(i) = \int_0^i \frac{1}{2} \sin(i) di, \quad (\text{A.31})$$

$$= -\frac{1}{2} [\cos i - 1]. \quad (\text{A.32})$$

Now, solving for $F(i) = F(F^{-1}(U))$ we obtain:

$$U = F(F^{-1}(U)), \quad (\text{A.33})$$

$$= -\frac{1}{2} [\cos F^{-1}(U) - 1], \quad (\text{A.34})$$

$$-2U = \cos F^{-1}(U) - 1, \quad (\text{A.35})$$

$$F^{-1}(U) = \arccos 1 - 2U, \quad (\text{A.36})$$

so $\cos i = \cos(F^{-1}(U))$ is distributed uniformly in the range $[-1, 1]$.

A.2.2 Power law

Some distributions, such as generating the masses of stars from the Kroupa IMF, used a power law in the form $p(x) = Ax^n$. Normalising between x_{\min} and x_{\max} we get $A = (n + 1)/(x_{\max}^{n+1} - x_{\min}^{n+1})$. The CDF is:

$$F(x) = \int_{x_{\min}}^x p(x) dx, \quad (\text{A.37})$$

$$= \frac{A}{n + 1} [x^{n+1} - x_{\min}^{n+1}], \quad (\text{A.38})$$

$$= \frac{x^{n+1} - x_{\min}^{n+1}}{x_{\max}^{n+1} - x_{\min}^{n+1}}. \quad (\text{A.39})$$

Solving for $F(x) = F(F^{-1}(U))$ as before:

$$F(F^{-1}(U)) = \frac{(F^{-1}(U))^{n+1} - x_{\min}^{n+1}}{x_{\max}^{n+1} - x_{\min}^{n+1}}, \quad (\text{A.40})$$

$$(F^{-1}(U))^{n+1} = (x_{\max}^{n+1} - x_{\min}^{n+1})U + x_{\min}^{n+1}, \quad (\text{A.41})$$

$$x = [(x_{\max}^{n+1} - x_{\min}^{n+1})U + x_{\min}^{n+1}]^{1/(n+1)}. \quad (\text{A.42})$$

For the case of $p(a) = Ax^{-1}$ for Öpik's law, $A = 1/(\ln a_{\max}/a_{\min})$ and the CDF is:

$$F(a) = \frac{\ln a - \ln a_{\min}}{\ln a_{\max} - \ln a_{\min}}. \quad (\text{A.43})$$

Solving for $F(a) = F(F^{-1}(U))$ yields:

$$a = e^{U(\ln a_{\max} - \ln a_{\min}) - \ln a_{\min}}, \quad (\text{A.44})$$

$$= a_{\min} e^{U(\ln a_{\max} - \ln a_{\min})}, \quad (\text{A.45})$$

$$= a_{\min} (a_{\max}^U - a_{\min}^U), \quad (\text{A.46})$$

$$= a_{\max}^U a_{\min}^{1-U}. \quad (\text{A.47})$$

A.2.3 Gaussian

The eccentricities of some of the wider stellar binaries from chapter 3 were drawn from a Gaussian distribution. The probability distribution for the eccentricity drawn from a Gaussian with mean μ and standard deviation μ is:

$$p(e) = \frac{1}{\sqrt{2\pi\sigma^2}} e^{-\frac{(e-\mu)^2}{2\sigma^2}}, \quad (\text{A.48})$$

The CDF is written as:

$$F(e) = \frac{1}{\sqrt{2\pi\sigma^2}} \int_0^e e^{-\frac{(e-\mu)^2}{2\sigma^2}} de, \quad (\text{A.49})$$

$$= \frac{1}{2} \operatorname{erf} \left(\frac{e - \mu}{\sqrt{2}\sigma} \right) + 1, \quad (\text{A.50})$$

where $\operatorname{erf}(x) = 2/\pi \int_0^x e^{-x^2} dx$ is the error function. Therefore the eccentricity can be drawn from $F(F^{-1}(U)) = U$:

$$U = \frac{1}{2} \operatorname{erf} \left(\frac{F^{-1}(U) - \mu}{\sqrt{2}\sigma} \right) + 1, \quad (\text{A.51})$$

$$e = \sqrt{2}\sigma \operatorname{erf}^{-1}(2U - 1) + \mu, \quad (\text{A.52})$$

where erf^{-1} is the inverse of the error function.

A.3 Parabolic orbits

In chapter 3, the outer orbit of the stellar binary was approximated to be a parabolic orbit ($e = 1$) around the massive black hole (MBH). The specific energy of a parabolic orbit is $\varepsilon = 0$, meaning that the velocity at any point in the orbit is equal to the escape velocity (from Equation A.1):

$$v = \sqrt{\frac{2GM}{r}}, \quad (\text{A.53})$$

which is also related to the orbital velocity of a circular orbit with semimajor axis equal to the radial distance r as $v/v_{\text{orb,circ}} = \sqrt{2}$. The radial position can be found from the true anomaly, and using $p = h^2/GM$:

$$r = \frac{h^2}{GM(1 + \cos \nu)}, \quad (\text{A.54})$$

We can use Barker's equation to relate the time difference at two points on an orbit with the difference in their true anomalies. This is derived from the expression for specific angular momentum $h = r^2\dot{\nu} = \sqrt{GMp}$. Rearranging this equation forms an integral:

$$r^2 d\nu = \sqrt{GMp} dt. \quad (\text{A.55})$$

We can substitute in Equation A.54 and use the identity $1 + \cos \nu = \sec \nu/2^2$:

$$\frac{p^2}{4} \sec^4 \left(\frac{\nu}{2} \right) d\nu = \sqrt{GMp} dt, \quad (\text{A.56})$$

$$\sec^4 \left(\frac{\nu}{2} \right) d\nu = 4 \sqrt{\frac{GM}{p^3}} dt. \quad (\text{A.57})$$

The integral can now be calculated:

$$\int_{t_0}^{t_1} 4 \sqrt{\frac{GM}{p^3}} dt = \int_{\nu_0}^{\nu_1} \sec^4 \left(\frac{\nu}{2} \right) d\nu, \quad (\text{A.58})$$

$$4 \sqrt{\frac{GM}{p^3}} (t_1 - t_0) = \int_{\nu_0}^{\nu_1} \left[1 + \tan^2 \left(\frac{\nu}{2} \right) \right] \sec^2 \left(\frac{\nu}{2} \right) d\nu, \quad (\text{A.59})$$

$$= \left[2 \tan \left(\frac{\nu}{2} \right) \right]_{\nu_0}^{\nu_1} + \int_{\nu_0}^{\nu_1} \tan^2 \left(\frac{\nu}{2} \right) \sec^2 \left(\frac{\nu}{2} \right) d\nu. \quad (\text{A.60})$$

The integral on the right can be solved using through substitution of $u = \tan(\nu/2)$ and $du/d\nu = \sec^2(\nu/2)/2$. Then the integral becomes:

$$\int_{\nu_0}^{\nu_1} \tan^2 \left(\frac{\nu}{2} \right) \sec^2 \left(\frac{\nu}{2} \right) d\nu = \int_{\nu=\nu_0}^{\nu=\nu_1} 2u^2 du, \quad (\text{A.61})$$

$$= \left[\frac{2u^3}{3} \right]_{\nu=\nu_0}^{\nu=\nu_1}, \quad (\text{A.62})$$

$$= \left[\frac{2 \tan^3 \left(\frac{\nu}{2} \right)}{3} \right]_{\nu_0}^{\nu_1}. \quad (\text{A.63})$$

So we end with the equation:

$$6 \sqrt{\frac{GM}{p^3}} (t_1 - t_0) = 3 \tan \left(\frac{\nu_1}{2} \right) + \tan^3 \left(\frac{\nu_1}{2} \right) - \left[3 \tan \left(\frac{\nu_0}{2} \right) + \tan^3 \left(\frac{\nu_0}{2} \right) \right]. \quad (\text{A.64})$$

Setting t_0 to the time of the periapsis passage also results in the bracketed terms on the right side disappearing ($\tan^3 0 = \tan 0 = 0$). A solution in $\tan \nu/2$ using the relative time from periapsis can be found through the substitution $\tan \nu/2 = (z - 1/z)$, meaning that Equation A.64 can be written as:

$$\left(z - \frac{1}{z}\right)^3 + 3\left(z - \frac{1}{z}\right) = 2B, \quad (\text{A.65})$$

$$2B = z^3 - \frac{1}{z^3} - 3z + \frac{3}{z} + 3z - \frac{3}{z}, \quad (\text{A.66})$$

$$= z^3 - \frac{1}{z^3}, \quad (\text{A.67})$$

where $B = 3\sqrt{GM/p^3}(\Delta t)$ with Δt as the time to periapsis. This means we have a quadratic to solve in $x = z^3$:

$$z^6 - 2Bz^3 - 1 = 0, \quad (\text{A.68})$$

$$x^2 - 2Bx - 1 = 0, \quad (\text{A.69})$$

$$x = B \pm \sqrt{B^2 - 1}, \quad (\text{A.70})$$

$$z = \left(B \pm \sqrt{B^2 - 1}\right)^{1/3}, \quad (\text{A.71})$$

$$\tan\left(\frac{\nu}{2}\right) = (B + \sqrt{B^2 - 1})^{1/3} - (B + \sqrt{B^2 - 1})^{-1/3}, \quad (\text{A.72})$$

where the negative root is ignored as the solution is the same.

A.4 Stellar tides using a Runge-Kutta Cash-Karp method

A Runge-Kutta Cash-Karp method was used to solve for the eccentricity evolution of the inner binary in chapter 3 due to stellar tides. A fourth-order was used to solve for the next step, and the fifth-order for obtaining an estimate of the error. The method is described below for a general function $dy/dx = f(x, y)$ which describes

a_i	b_{ij}					
0						
$\frac{1}{5}$	$\frac{1}{5}$					
$\frac{3}{10}$	$\frac{3}{40}$	$\frac{9}{40}$				
$\frac{3}{5}$	$\frac{3}{10}$	$-\frac{9}{10}$	$\frac{6}{5}$			
1	$-\frac{11}{54}$	$\frac{5}{2}$	$-\frac{70}{27}$	$\frac{35}{27}$		
$\frac{7}{8}$	$\frac{1631}{55296}$	$\frac{175}{512}$	$\frac{575}{13824}$	$\frac{44275}{110592}$	$\frac{253}{4096}$	
c_i	$\frac{2825}{27648}$	0	$\frac{18575}{48384}$	$\frac{13525}{55296}$	$\frac{277}{14336}$	$\frac{1}{4}$
c_i^*	$\frac{37}{378}$	0	$\frac{250}{621}$	$\frac{125}{594}$	0	$\frac{512}{1771}$

Table A.1: Parameters for the fourth and fifth order equations using the Runge-Kutta Cash-Karp method.

how y evolves due to x , and given an initial value $y(x_0) = y_0$. The general forms of the fourth and fifth order Runge-Kutta equations to solve for the next step, y_{n+1} and y_{n+1}^* , given a current step y_n are (Press et al. 2002):

$$y_{n+1} = y_n + O(h^5) + \sum_{i=1}^6 c_i k_i, \quad (\text{A.73})$$

$$= y_n + O(h^6) + \sum_{i=1}^6 c_i^* k_i, \quad (\text{A.74})$$

where h is the step size, c_i and c_i^* are coefficients which give a weight to each of the parameters k_i , which consist of evaluations of the function $f(x, y)$ at several points from $x_n = x$ to $x_{n+1} = x + h$. The parameters k_i are written as (ibid.):

$$k_i = hf \left(x_n + a_i h, y_n + \sum_{j=1}^{i-1} b_{ij} k_j \right). \quad (\text{A.75})$$

The values of the parameters and coefficients for the Cash-Karp variant can be found in Butcher tableau in Table A.1.

The estimate of the error is then obtained by comparing the results from the fifth and fourth order Runge-Kutta methods, $\Delta = |y_{n+1} - y_{n+1}^*|$. The step size h can be adapted to balance between precision and speed, with the error scaling as $\Delta \propto h^5$. Therefore, if a step h_0 produces an error larger than desired $\Delta_0 > \Delta_{\max}$, the step

size can be reduced to the maximum desired error as $h_{\max} = h_0 |\Delta_{\max}/\Delta_0|^{0.2}$. The actual implementation of the method makes use of the recommended adaptive step size routine, accounting for some uncertainty in the error (Press et al. 2002, pp.722-723):

$$h = \begin{cases} Sh_0 \left| \frac{\Delta_{\max}}{\Delta_0} \right|^{0.2} & \Delta_0 \leq \Delta_{\max} \\ Sh_0 \left| \frac{\Delta_{\max}}{\Delta_0} \right|^{0.25} & \Delta_0 > \Delta_{\max} \end{cases}, \quad (\text{A.76})$$

where $S = 0.95$ is a "safety factor" because the error is only an estimate of the true error.

A.5 Tidal disruption of a star and binary by a MBH

A single star of mass m_* and radius R_* on an orbit at semimajor axis a around an MBH of mass M_{MBH} will feel a gravitational attraction $F_g = GMm/a^2$. The strength of the attraction at the surface of the star to the MBH will, in general, be different from the strength at the centre. This is known as the tidal force, and is strongest at the points on the surface closest and farthest from the MBH (assuming a spherical shape) – which are connected by a line passing through the centre of the star and the centre of the black hole. The tidal force at these points can therefore be calculated by considering the differences in the force felt by a test particle on the surface of the star versus at the centre, resulting in an acceleration:

$$a_t = \left| \frac{GM_{\text{MBH}}}{a^2} - \frac{GM_{\text{MBH}}}{(a \pm R_*)^2} \right|, \quad (\text{A.77})$$

$$= GM_{\text{MBH}} \left| \frac{1}{a^2} - \frac{1}{(a \pm R_*)^2} \right|. \quad (\text{A.78})$$

The surface term can be expanded:

$$\frac{1}{(a + R_*)^2} = \frac{1}{a^2 + R_*^2 \pm 2aR_*}, \quad (\text{A.79})$$

$$= \frac{1}{a^2(1 \pm \frac{2R_*}{a} + \frac{R_*^2}{a^2})}. \quad (\text{A.80})$$

In the limit where $a \gg R_*$, the higher order term R_*^2/a^2 is small and can be ignored.

This means the acceleration due to the tidal force can now be written as:

$$a_t \approx \frac{GM_{\text{MBH}}}{a^2} \left| 1 - \frac{1}{1 \pm \frac{2R_*}{a}} \right|. \quad (\text{A.81})$$

The right-hand term, $1/(1 + 2R/a)$ can be expressed as a Taylor series, and because $2R \ll a$ it will converge quickly. Expanding the series to first order, the acceleration is now:

$$a_t \approx \frac{GM_{\text{MBH}}}{a^2} \left| 1 - \left(1 \pm \frac{2R_*}{a} \right) \right|, \quad (\text{A.82})$$

$$\approx \frac{2GM_{\text{MBH}}R_*}{a^3}. \quad (\text{A.83})$$

The star can be tidally disrupted if the tidal force exceeds the star's self-gravity.

Using the same terms as before, this is where:

$$\frac{2GM_{\text{MBH}}R_*}{a^3} \gtrsim \frac{Gm}{R_*^2}. \quad (\text{A.84})$$

The boundary where the two forces are equal occurs at a semimajor axis:

$$a_{\text{TD}} \approx \left(\frac{m}{2M_{\text{MBH}}} \right)^{1/3} R_*. \quad (\text{A.85})$$

The tidal force on a stellar binary due to an MBH can be found using the same method, this time considering the difference in the gravitational force between the two stars of mass m . Assuming the plane of the inner orbit of the binary is aligned

with the outer orbit around the MBH, the tidal force during a conjunction of all three bodies is:

$$F_{t,\text{bin}} \approx \frac{GM_{\text{MBH}}M_{\text{bin}}a}{r^3}, \quad (\text{A.86})$$

where M_{MBH} is the mass of the MBH, $M_{\text{bin}} \approx 2m$ is the mass of the binary, a is the semimajor axis of the binary and r is the distance between the centre of mass of the binary and the MBH. Inclined orbits reduce the tidal force, and inclinations of $i = 90^\circ$ will cause it to vanish for an equal mass binary. Similarly to the star, the binary will be tidally disrupted (separated) by the MBH if this tidal force exceeds the gravitational force between the two stars. This occurs when $R_{\text{TS}} \approx (M_{\text{MBH}}/M_{\text{bin}})^{1/3}a$.

A.6 Fluctuations of the binary orbital energy by a MBH

An order of magnitude calculation of the orbital energy fluctuations in the binary due to the tidal force by the MBH over one orbit of the binary can be obtained by considering the work done on one of the stars in the binary, treated as a test particle, by the MBH. The work can be calculated from the equation $W = P\tau$, where $P = F_t v \cos \theta$ is the power, $F_t = 2GM_{\text{BH}}a/r_{\text{p,out}}^3$ is the magnitude of the tidal force applied to the binary by the MBH, $v \approx \sqrt{GM_{\text{bin}}/a}$ is the velocity of one of the stars and $\cos \theta$ is the angle between the tidal force and stellar velocity vectors. Then, the power can be written as:

$$P \approx \frac{2G^{3/2}M_{\text{bin}}^{1/2}M_{\text{MBH}}a^{1/2}}{r_{\text{p,out}}^3} \cos \theta, \quad (\text{A.87})$$

which is the approximate power as the outer orbit of the binary reaches the periapsis distance around the MBH, where the tidal force will be greatest (assuming the stars

are in conjunction with the MBH). The time that this power is applied for is related to the orbital period, $\tau \approx P_{\text{bin}} = 2\pi(a^3/GM_{\text{bin}})^{1/2}$. Thus, the work done is approximately:

$$W \approx 4\pi G\gamma \frac{M_{\text{MBH}}a^2}{r_{\text{p,out}}^3}, \quad (\text{A.88})$$

where $\gamma < 1$ is a factor that accounts for the magnitude of the tidal force fluctuating over a the course of the binary orbit, whilst at the same time the alignment of the velocity and tidal force vectors varies between $0 - 90^\circ$. This work is the change in orbital energy $\Delta\varepsilon$ of the test star, and can be written as a fractional change by considering the specific orbital energy $\varepsilon = -\mu/2a$, where $\mu = GM_{\text{bin}}$:

$$\left| \frac{\Delta\varepsilon}{\varepsilon} \right| \sim 2\pi\gamma \frac{M_{\text{MBH}}}{M_{\text{bin}}} \left(\frac{a}{r_{\text{p,out}}} \right)^3, \quad (\text{A.89})$$

$$\sim 2\pi\gamma \left(\frac{R_{\text{TS}}}{r_{\text{p,out}}} \right)^3. \quad (\text{A.90})$$

So the expected maximum fluctuations in orbital energy of the binary increase strongly with larger tidal separation radii and with smaller periapsis distances of the outer orbit. The initial periapsis distance is set to 5 times the tidal separation radius in simulations performed in this work, so it is expected that fluctuations at the beginning will be fairly small, of the order of $\sim 1\%$.

A.7 Long-term Kepler system integrations

This section looks at the dynamical evolution of the planetary systems in the long-term integrations individually. This includes looking at the changes in orbital elements over time, finding out how and why systems are becoming unstable. In the original simulations the integrations lasted for one million orbital periods, which is $\lesssim 10^6$ years for the majority of systems – meaning that these simulations last 2 – 3 orders of magnitude longer. Sixteen systems consisting of just Kepler planets were

selected at random, and integrated for a significantly longer length of time. Table A.2 displays the results of the long integrations. It can be seen that the systems contain either three or four planets. This is because these systems were generated in the first set of integrations which contained a bug relating to the generation of number of planets in each system, which was fixed and all other integrations were rerun. These integrations were not performed again due to time constraints, but they are still valid planetary systems otherwise. The systems are run for a fixed amount of CPU time, which is why the length of integration time varies across systems, especially with three versus four planets present in the system as the systems with fewer bodies require fewer force calculations. Only two of the systems become unstable in these longer runs, both containing four planets. However, it has to be considered that systems containing a larger number of planets (~ 10) that remained stable after one million inner orbits would be more likely to become unstable during these longer integrations. Some of systems reach times of ~ 1 Gyr (e.g. systems 4006 and 4003) and are still stable, which is starting to approach the age of our Solar System. This isn't unexpected, as these planets all begin at low eccentricities and it was shown that the majority of these systems still remain at low eccentricities after one million inner orbital periods. This means that a much longer time is required to grow eccentricities without any massive planets present.

System 4000

This system contains four planets and has the smallest spacing between any pair of planets across all systems, measured by both d_{CPP} and Δ_{min} . This system remains stable for ~ 22.7 million years, with evolution relatively uneventful for the first 20 million years. This system remained stable for an order of magnitude longer than predicted by the line of best fit, inline with the typical spread observed in stability timescales. Over the next few million years the eccentricity begins to grow in the planets, particularly the inner two planets (Figure A.1). The relatively small spac-

System	N	Stable	Time (yrs)	d_{CPP}	Δ_{min}	τ_{exp} (years)	C
4000	4	No	2.27×10^7	7.218	7.279	$1.04^{+1.11}_{-0.537} \times 10^6$	U
4001	4	Yes	2.82×10^8	21.182	21.147	$2.90^{+20.61}_{-2.54} \times 10^{16}$	S
4002	3	Yes	3.07×10^8	11.493	9.694	$1.04^{+3.92}_{-0.82} \times 10^9$	S
4003	3	Yes	8.95×10^8	9.335	8.316	$6.19^{+17.54}_{-4.58} \times 10^7$	MS
4004	4	Yes	1.98×10^8	24.211	28.683	$1.37^{+22.06}_{-1.29} \times 10^{22}$	S
4005	4	No	2.70×10^7	10.736	10.703	$3.96^{+7.47}_{-2.59} \times 10^8$	U
4006	3	Yes	9.41×10^8	9.189	7.656	$1.61^{+3.93}_{-1.14} \times 10^7$	MS
4007	3	Yes	5.03×10^8	29.843	29.197	$2.16^{+23.67}_{-2.14} \times 10^{26}$	S
4008	3	Yes	1.28×10^8	36.220	30.103	$1.38^{+174.9}_{-1.37} \times 10^{27}$	S
4009	3	Yes	2.58×10^8	20.202	21.934	$7.66^{+255.57}_{-7.44} \times 10^{19}$	BS
4010	3	Yes	6.19×10^8	29.514	35.806	$1.594^{+510.68}_{-1.589} \times 10^{32}$	S
4011	4	Yes	1.96×10^7	24.361	20.938	$2.02^{+14.01}_{-1.76} \times 10^{16}$	S
4012	4	Yes	1.17×10^8	11.980	10.761	$4.38^{+8.33}_{-2.87} \times 10^8$	S
4013	4	Yes	1.26×10^8	10.103	8.485	$7.75^{+10.14}_{-4.39} \times 10^6$	S
4014	3	Yes	9.33×10^8	13.981	12.914	$7.49^{+52.71}_{-6.56} \times 10^{11}$	S
4015	4	Yes	2.14×10^8	8.795	7.338	$1.16^{+1.24}_{-0.60} \times 10^6$	MS

Table A.2: Stability of long-term integrations of Kepler planet-only systems by semi-major axis order. The time given is the length of time the stable remained stable for, or when integration was ended in the case of a system still remaining stable. The initial planet minimum planet spacing is also given expressed as both d_{CPP} and Δ_{min} . τ_{exp} is the expected stability timescale based on the parameters of the line of best fit calculated in section 2.5.3. The category of each system is determined as U for unstable, S for stable, MS for marginally stable and BS for becomes stable. MS systems contain planets whose orbital parameters appear to be fluctuating chaotically whilst growing over time, and BS is the lone system which appears to migrate from MS to S during integration. S systems experience no significant change in orbital parameters or their evolution over the entire integration.

ing between the planets results in their orbits crossing when eccentricities of these planets reach $e \sim 0.25$, and eventually close encounters disrupt their orbits as can be seen in Figure A.2. Body 1 migrates outwards to sit just outside of body 2, and it's moderate eccentricity results in another encounter which kicks it out further to ~ 8 AU with a high eccentricity $e \sim 0.75$. Even at this high eccentricity, it remains in orbit around the star until the integration finishes. Body 0's semimajor axis and eccentricity fluctuate for ~ 60 million years after the initial close encounter, but it never reaches a stable configuration and is finally ejected from the system. After

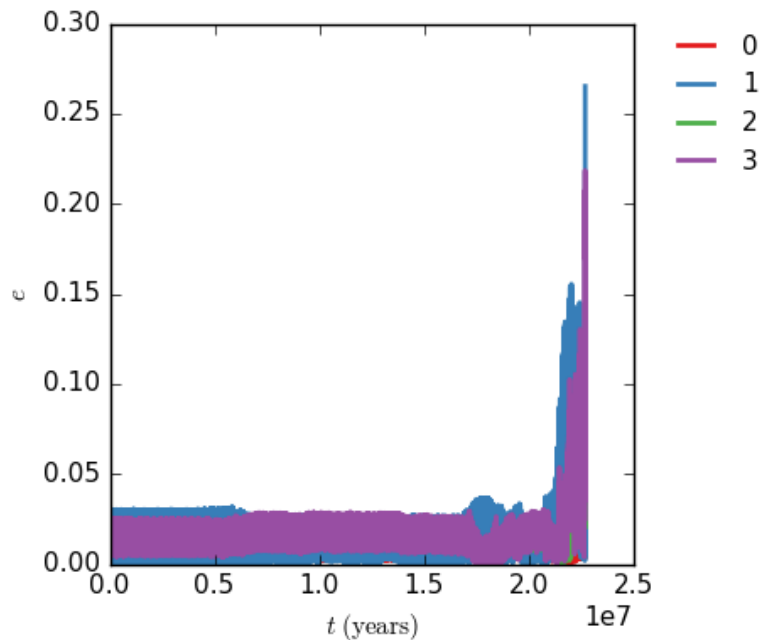


Figure A.1: The eccentricity of each body over time for system 4000, cutoff at the point where the system initially reorders by semimajor axis.

the ejection of this body, the remaining three bodies maintain a stable configuration with relatively fixed semimajor axes and oscillating eccentricities. The final spacing between the planets is larger than the initial configuration, but the larger eccentricities means future stability can no longer just be predicted from differences in semimajor axis. The inclination of each body is shown in Figure A.3. After the first encounter, body 3 performs some orbit flips between prograde and retrograde until it is eventually ejected. Body 1 remains in a prograde orbit, peaking at $\sim 80^\circ$ whilst it crosses the orbits of bodies 0 and 2, before settling at $i \lesssim 40^\circ$ (hidden behind body 3).

System 4005

This system becomes unstable over a similar timescale to system 4000, even though the minimum spacing between planets are comparable to some of the systems which remained stable with both d_{CPP} and $\Delta_{\text{min}} > 10$. The relatively quick instability is also apparent when comparing to the expected timescale from the line of best fit,

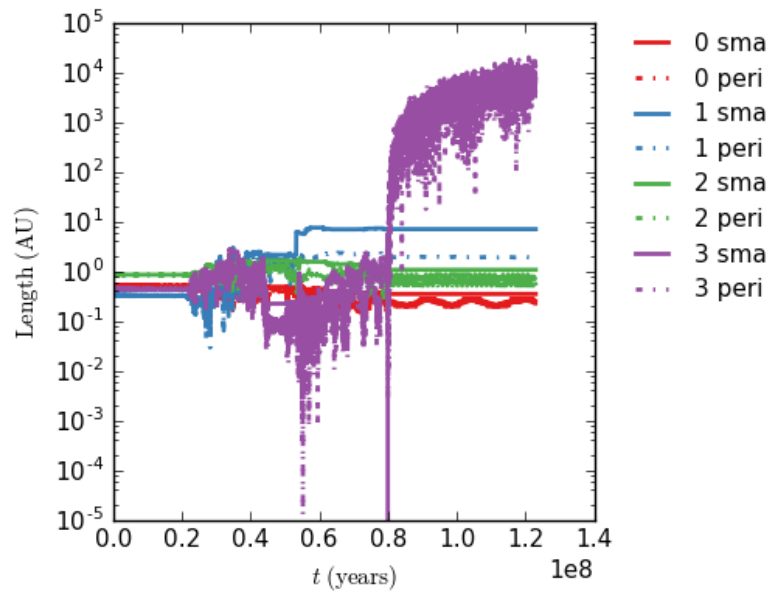


Figure A.2: The semimajor axis (solid line) and periastron distance (dashed line) over time for each of the bodies in system 4000. The solid line disappears for body 3 when it is ejected at $t \sim 8 \times 10^7$ years.

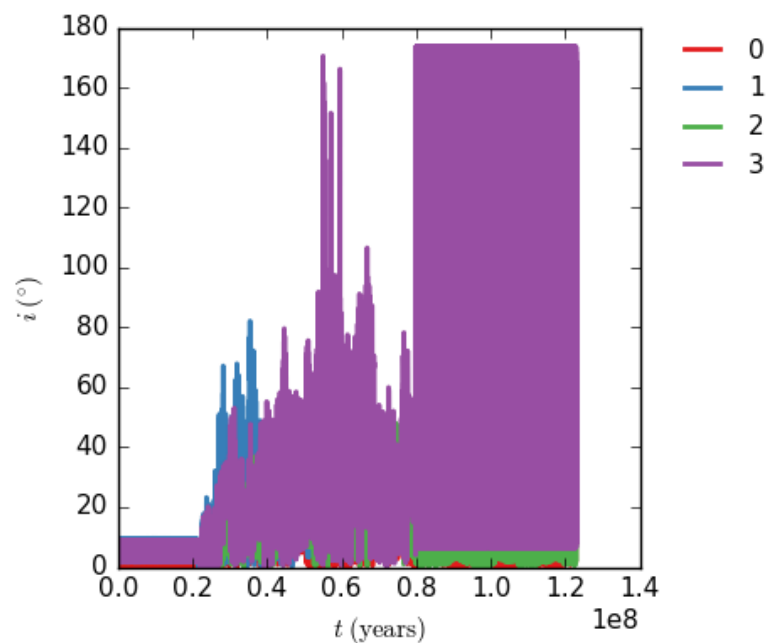


Figure A.3: The inclination of planets in unstable system 4000. Body 3 flips between prograde and retrograde orbits several times between the first close encounter and ejection.

this time an order of magnitude larger than the actual time the system remained stable – although again within the range of observed spread of timescales. The evolution of bodies is also similar to system 4000, with slow initial evolution until growing fluctuations in eccentricity cause close encounters. At around 27 million years into the integration, bodies 0 and 3 experience a close encounter due to the slow eccentricity growth in body 0 causing the orbits to cross (Figure A.4). Body 0 is kicked to a wider orbit, and ends up as the outer body after ~ 8 million years due to interactions with bodies 1 and 2, as shown in Figure A.5). From this initial instability, body 3 evolves erratically with semimajor axis fluctuations and very large fluctuations in its eccentricity (left panel in A.4), and also undergoes chaotic flipping between prograde and retrograde orbits. Bodies 1 and 2 swap semimajor axis order ~ 58 million years into the integration, and undergo the process again at ~ 88 million years. This system’s evolution still appears very active, unlike system 4000 where only small changes can be observed after one planet is ejected. Evolution in the eccentricity and inclination of each body doesn’t appear coherent, and no first-order resonances were found in these parameters comparing peak frequencies from their fast fourier transforms (FFTs). Body 3 is only marginally bound to the host star with its eccentricity frequently approaching 1, and ejection from the system is probable. Only body 0 appears to be relatively safe from the inner planets due to its large final semimajor axis, but future close encounters in the inner part of the system are very likely, and could result in another planet being thrown out to a similar semimajor axis and disturb the orbit – particularly because of the moderately high ($e \gtrsim 0.6$) eccentricity of body 0 meaning that it sweeps through a large band in space over many orbits.

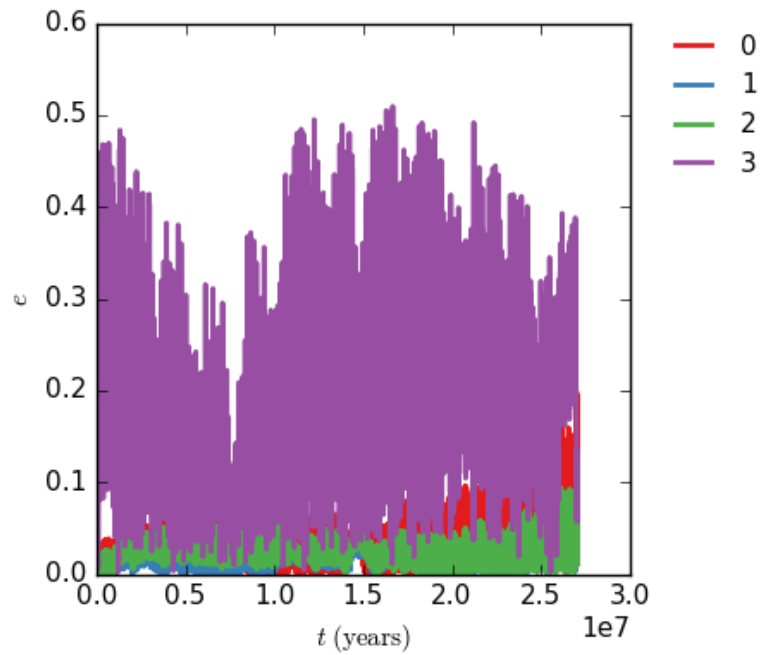


Figure A.4: The eccentricity of each body over time for system 4005, cutoff at the point where the system initially reorders by semimajor axis.

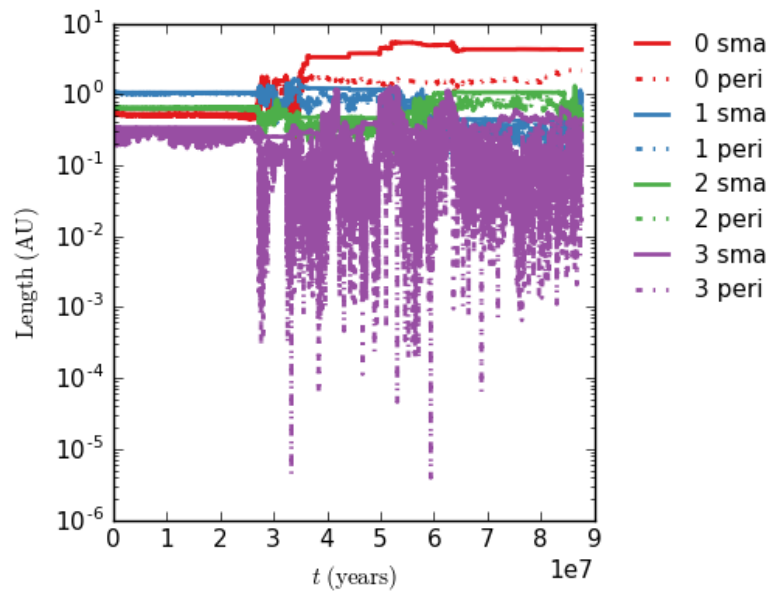


Figure A.5: The semimajor axis (solid line) and periastris distance (dashed line) over time for each of the bodies in system 4005.

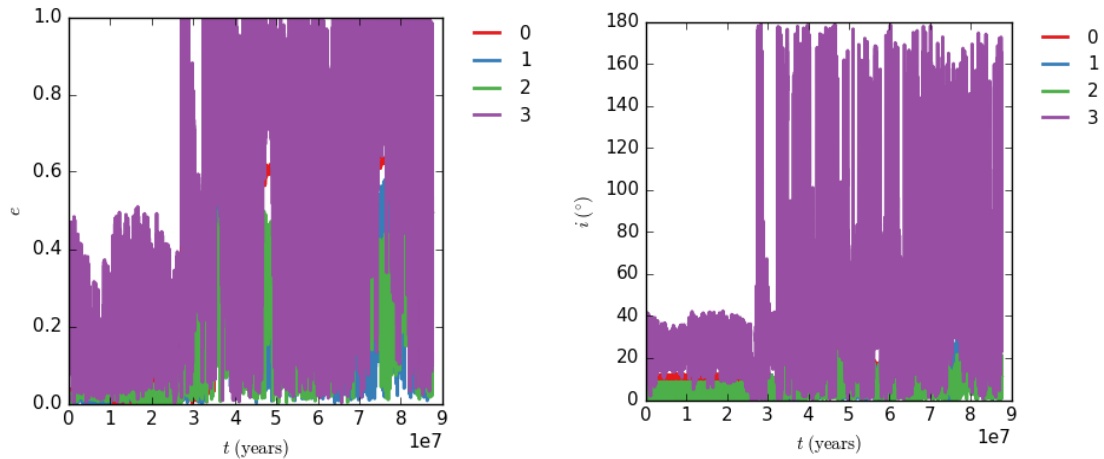


Figure A.6: Eccentricity (left) and inclination (right) of each planet in system 4005, shown over the entire integration.

Stable systems

The remaining fourteen systems preserved the ordering of their planets by semi-major axes during these long-term integrations. Some of these systems may be in resonances which protect the planets from close encounters, or the planets may be simple spaced far-enough apart that there is insufficient time for perturbations to grow eccentricities and change the semimajor axes enough in the time of the simulation. Broadly speaking, when looking at the evolution of the orbital elements of each planet in these systems, they appear to fit into one of two categories. In both cases the semimajor axes of the planets remain very close to initial values, such as in Figure A.7.

The largest category is where the evolution of each planet’s eccentricity and inclination appears to remain the same over the course of the integration, so the system’s parameters are almost the same at the end as the initial conditions. Figure A.8 shows an example system displaying this behaviour. The fluctuations in these orbital elements remain at roughly the same magnitude, and oscillations appear coupled between bodies. Evolution in these systems appear coherent, meaning that the these systems can potentially remain stable for much longer periods of time. When

looking at the smallest spacings between planets in these systems, a lot of them are very well spaced with $\Delta_{\min} > 20$ – so it isn't surprising that these remain stable in these integrations as even inclined massive Jupiters did not destabilise any systems at these spacings. A few systems in this category do have smaller minimum planet spacings, with $\Delta_{\min} = 8.485$ for system 4013. This system is predicted to have become unstable within $\sim 10^6 - 10^7$ years as predicted by the line of best fit, even when considering uncertainties. The other systems typically had very long expected timescales compared to the age of the Solar System, although this is assuming the fit is valid when extrapolated and doesn't plateau past a certain timescale similarly to the systems with inclined perturbers.

The other category contains three systems, and contain planets which show non-coherent evolution in their orbital elements (which can be seen in Figure A.9). Fluctuations in eccentricity are observed to grow during the integration and, assuming this continues for times longer than integrated for, these can create orbit-crossing conditions and eventually the system will be destabilised. Thus these systems can be expected to become unstable at some point in the future, especially as these fluctuations are able to grow to moderate values in just a few million years (which occurred in system 4000 and was shown in Figure A.1). Whilst two of the three systems in this category are already stable for \sim Gyr timescales, these only contain 3 planets and evolution will typically be more rapid for systems of higher multiplicities. What's interesting to note is that each of these systems are stable for longer periods of time than predicted by the line of best fit, particularly system 4015 which is still stable after lasting 2 orders of magnitude longer than expected.

The final stable system appeared to jump from the non-coherent category to the other part-way through. Starting from almost circular orbits, eccentricities of the planets quickly grew to values fluctuating up to $e \sim 0.2 - 0.25$. However, these fluctuations ceased growing and the planet spacing was sufficient enough that a close

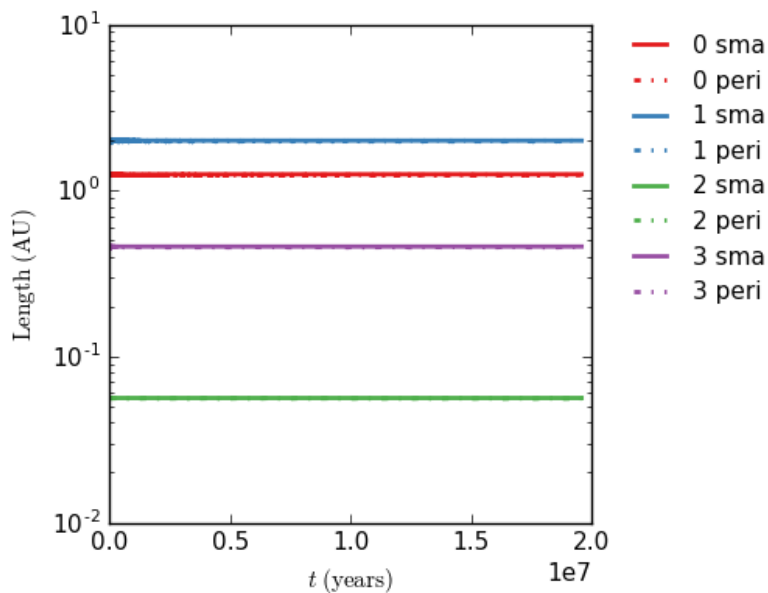


Figure A.7: The semimajor axis (solid line) and periastron distance (dashed line) over time for each of the bodies in the stable system 4011, showing no real changes.

encounter didn't occur (Figure A.10). After about ~ 170 million years fluctuations in eccentricities abruptly shrank to small values with consistent fluctuations of order $\sim \pm 0.1$ for each planet, with fluctuations also becoming consistently-sized for inclinations at the same time. This can be seen in Figure A.10, where the remaining evolution appears coherent until the integration ended. It is unclear what caused this change in behaviour, and how common it can occur, but this may mean that instability is not inevitable for the 3 “psuedostable” systems with growing fluctuations (although there a large difference in the minimum planet spacings). The fluctuations in eccentricity appear to be much larger than expected when considering the minimum planet spacing is $\Delta_{\min} > 20$, especially as they initially grew from small values over a short period of time.

So, overall it appears that eleven (including the lone system that migrated into this category) of the sixteen stable systems still appear to be stable post-integration, three systems are stable on $\sim 10^8$ timescales but might become unstable in the near-future, and two systems which don't remain stable with the ejection of a planet in one and a marginally-stable planet in the other. Looking back at the multiplicity

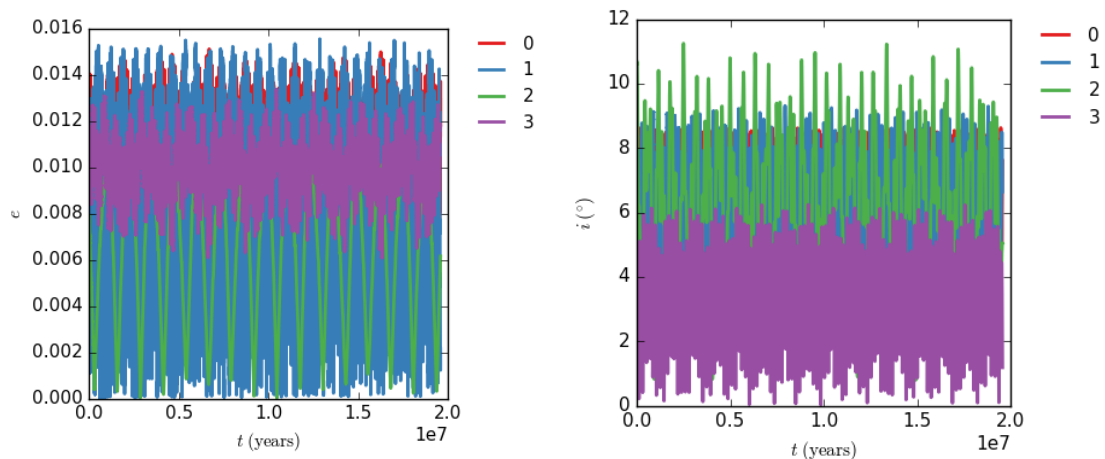


Figure A.8: Eccentricity (left) and inclination (right) of each planet in the stable system 4011, shown over the entire integration. Evolution appears coherent and predictable based on coupled oscillations.

distribution of Kepler-only planets in Figure 2.6, there are ~ 185 systems with one planet, most systems contain two-five planets. A prediction of the number of stable systems can be made on the timescales of these integrations (~ 0.1 Gyr) by considering the following. If eleven out of every sixteen planetary system with more than one planet is stable on this timescale (based on there being two-planet systems which are more likely to remain stable, which should act somewhat to counter the number of planetary systems with greater than four planets), then we can multiply this number by the 1,152 systems with more than one planet that remain stable for one million inner orbital periods. Then we add the single planet systems that will always remain stable, and we get the predicted number of systems remaining (marginally) stable for ~ 0.1 Gyr being 48.6%. If we use the less optimistic value of eight in sixteen, we obtain $\sim 38\%$ remaining stable (rather than marginally stable) for ~ 0.1 Gyr. Whilst these seem low, this is just an estimate on how many systems remain stable by semimajor axis order – even systems undergoing these changes doesn't mean the period-radius distribution will be dramatically change, as planets can reorder by semimajor axis and fulfill the unstable criterion without any ejections.

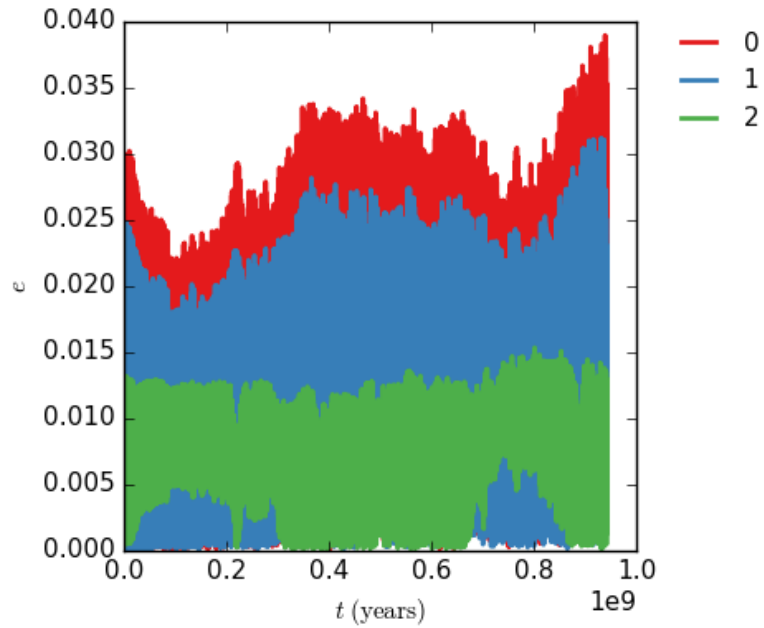


Figure A.9: The eccentricity evolution of planets in stable system 4006. Here the evolution doesn't remain coherent and the fluctuations grow in magnitude as time increases.

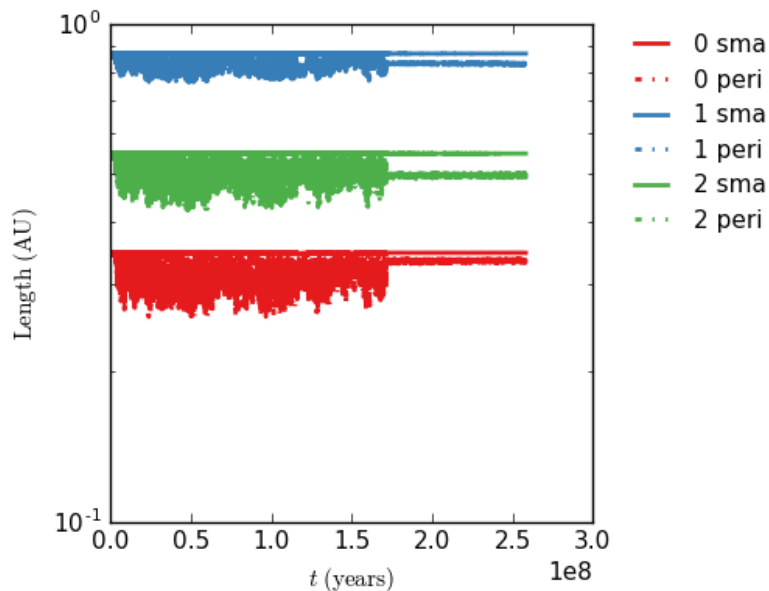


Figure A.10: The semimajor axis (solid line) and periapsis distance (dashed line) over time for each of the bodies in the stable system 4009, showing an abrupt change in evolution of planets after ~ 170 million years.

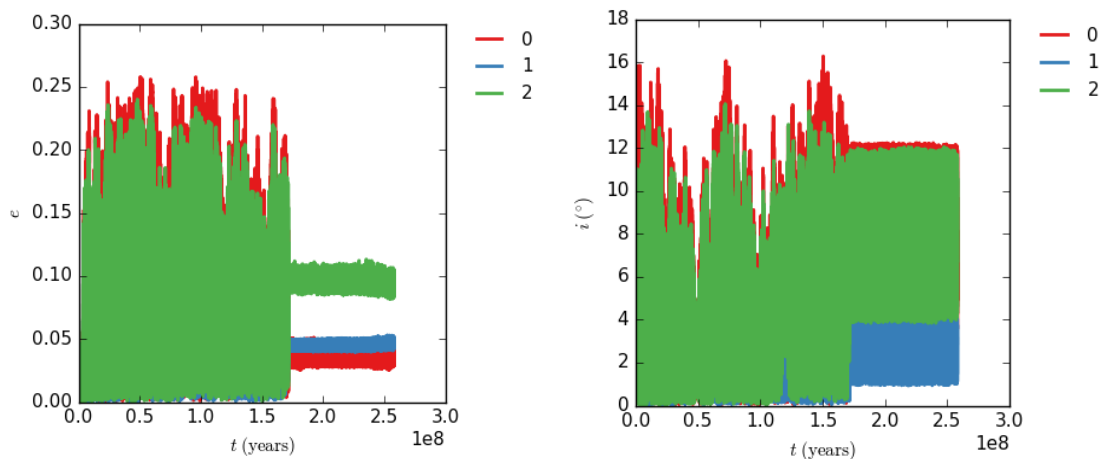


Figure A.11: Eccentricity (left) and inclination (right) of each planet in the stable system 4009, shown over the entire integration. Evolution appears coherent and predictable based on coupled oscillations.

A.8 Evolution of individual Kepler planetary systems

This section looks at comparing the evolution of individual systems in each configuration, including the Jupiter in aligned and inclined configurations. Whilst on the whole the stability of systems just containing Kepler planets and those with an additional aligned Jupiter-like perturber are similar, the stronger planet-planet interactions will affect the evolution of individual systems (as long as the Jupiter isn't too well-spaced in semimajor axis from the inner planets, weakening the interaction). Inclined perturbing bodies may result in some Kepler planets performing Kozai oscillations. A small number of systems are selected in each configuration (as their periodic output is not saved in the main set of integrations), and are integrated for 10^6 years. The short timescale compared to the long-term integrations means that only small number of planet ejections were observed, even after multiple changes in semimajor axis.

Immediately apparent in the planetary systems with inclined Jupiters is the precession of the orbital angular momentum vectors around the total angular momentum

vector of the system, which is dominated by the contribution from Jupiter. The orbits of the inner planets are therefore seen to precess around the angular momentum vector of the perturbing body, which can be seen in the left panel of Figure A.12. This system remains stable after integration whilst maintaining this configuration, with the semimajor axes of the planets remaining stable (right panel of Figure A.12). Eccentricity fluctuations slowly growing but still $e \lesssim 0.08$ after 10^6 years, and the minimum distance between any pair of planets in units of the Hill Radius of the more massive planet as ~ 6.4 . The planetary disk of inner planets is also preserved, with the thickness of the disk remaining unchanged. Only planet 0 and 1 are in the vicinity of a first-order mean motion resonance (MMR) resonance, with the distance from the 3:2 resonance (Ramos et al. 2017) as $\delta_{3/2} = (P_1/P_0) - (3/2) = 0.0379$. No other first-order MMRs are found. In some systems there were multiple planetary disks, which one such example shown in Figure A.13. Bodies 0 and 2 are seen to be in a disk which precesses coherently around the total angular momentum vector of the system, and these two bodies actually swap semimajor axis order several times during integration. The other two Kepler planets closest to the star also show coupled evolution with each other in a second disk, but don't precess cleanly around the angular momentum of the outer perturber. The eccentricities of the innermost planets can be seen to be excited at the two points where the two disks become aligned.

Almost all of the systems with inclined perturbers showed disk-like structures of planets precessing around the total orbital angular momentum vector, with most in a single disk configuration – even in the small number of unstable systems observed. None of these systems were found to display clear Lidov-Kozai (LK) oscillations, potentially due to suppression from interactions between other members of the disk. Figure A.14 shows the difference in periapsis angles for two planets from the same single-disk system shown in Figure A.12 that have been multiplied by two different integers whose difference is 1. Solid colours are circulating angles and oscillations

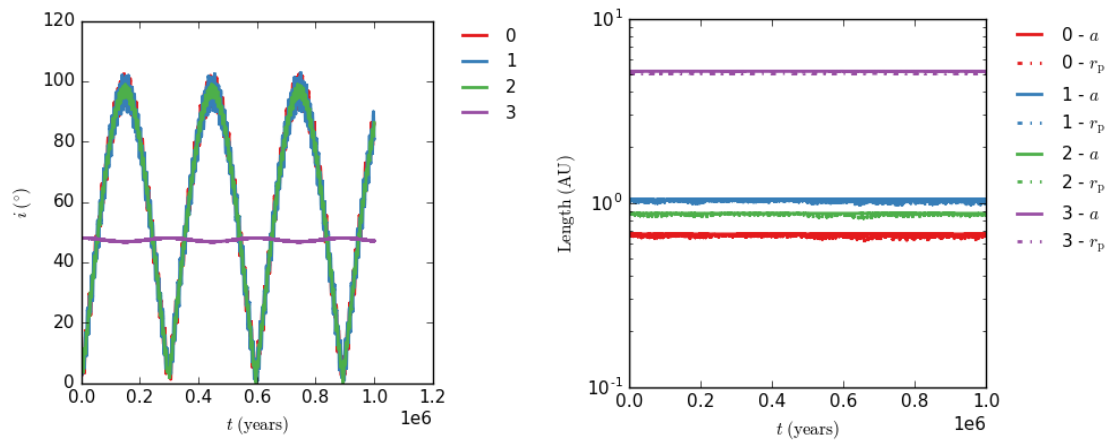


Figure A.12: The evolution of a system where the planetary disk precesses around the total angular momentum of the system, dominated by the outer perturbing body. The left panel shows the inclination of each planet, and the right panel their semimajor axis and periapsis.

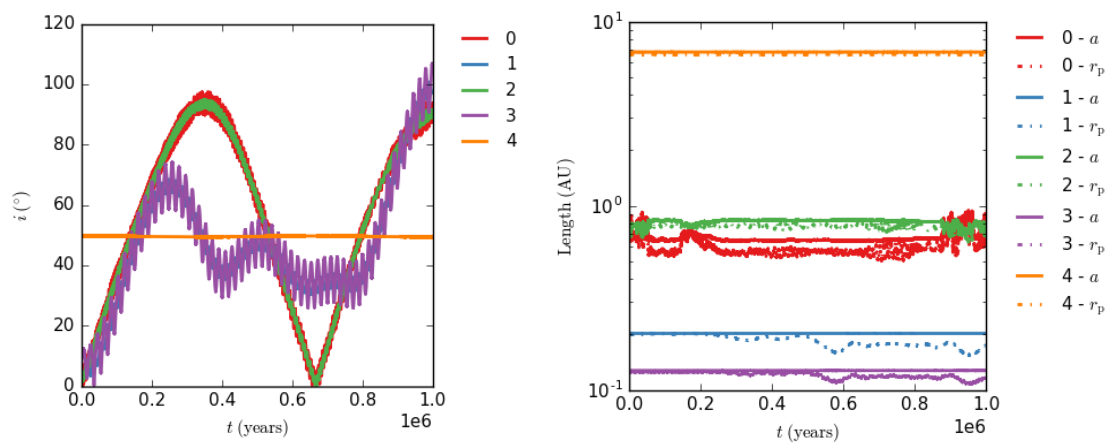


Figure A.13: Evolution of a planetary system with two planetary disks, showing the inclination of each planet (left) and their semimajor axis and periapsis (right).

show potential librations, which could indicate a resonance. The right panel of Figure A.15 shows the FFT of the eccentricity for a planet from the same single-disk system, which shows a significant peak corresponding to oscillations $\sim 10^5$ years. This peak is observed for all planets in the disk, and originates from oscillations seen at the start of the simulation which occur again half way through. These eccentricity excitations don't appear commensurable with the semimajor axis or inclination evolution of the system.

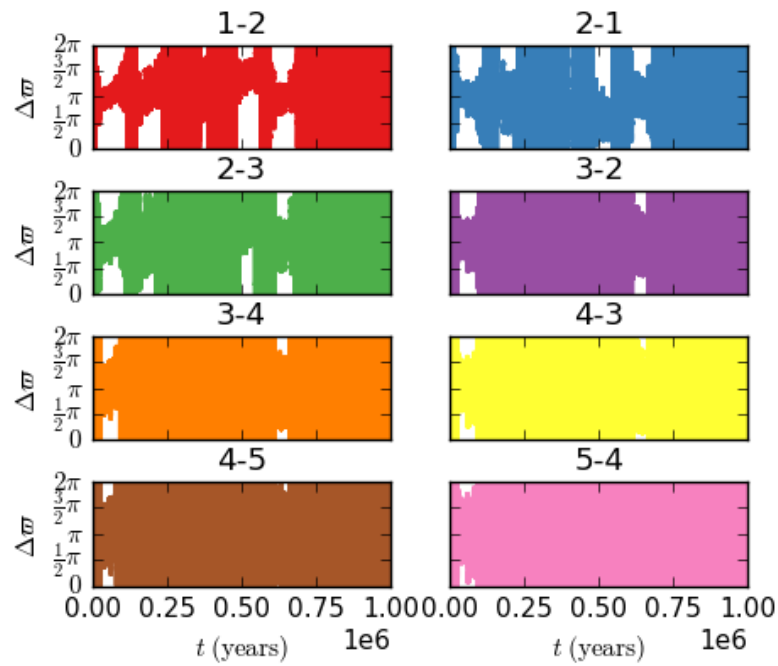


Figure A.14: Differences in the periapsis angles modulo- 2π for two planets in the single-disk system at first-order, where the angles are multiplied by two integers that differ in value by 1.

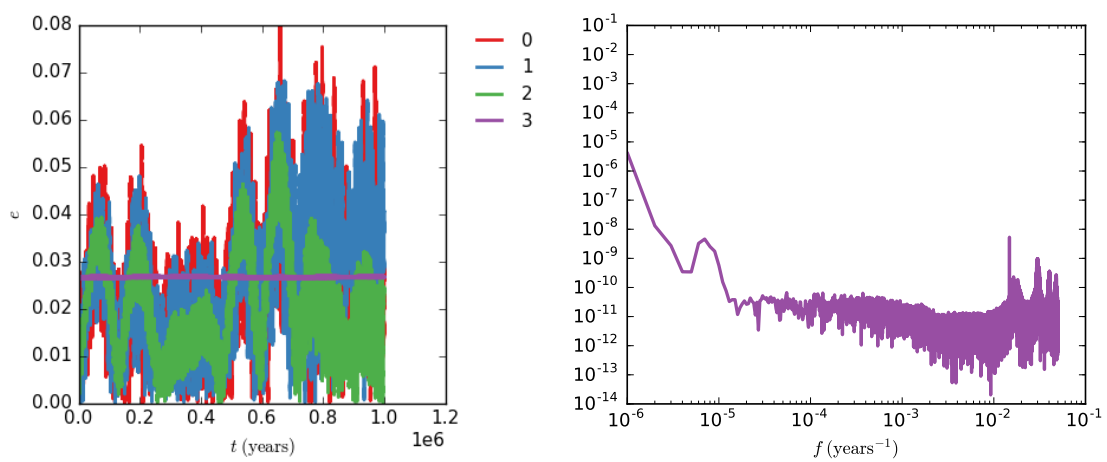


Figure A.15: Eccentricity evolution of the single-disk system and an FFT shown for one of the planets in the disk.

References

- [1] J. M. A. Danby. *Fundamentals of celestial mechanics*. 1988.
- [2] C. D. Murray and S. F. Dermott. *Solar system dynamics*. 1999.
- [3] W. H. Press et al. *Numerical recipes in C++ : the art of scientific computing*. 2002.
- [4] X. S. Ramos et al. “Planetary migration and the origin of the 2:1 and 3:2 (near)-resonant population of close-in exoplanets”. In: *ArXiv e-prints* (Apr. 2017). arXiv: 1704.06459 [astro-ph.EP].